Design of a Power-Efficient Radiative Wireless System for Autonomous Biomedical Implants

Shuoliang Ding

université PARIS-SACLAY

Design of a Power-Efficient Radiative Wireless System for Autonomous Biomedical Implants

Thèse de doctorat de l'université Paris-Saclay

École doctorale : Electrical, Optical, Bio : Physics And Engineering (EOBE)
Spécialité de doctorat : Imagerie et physique médicale
Unité de recherche : Université Paris-Saclay, CentraleSupélec, CNRS, Laboratoire de Génie Electrique et Electronique de Paris, 91192, Gif-sur-Yvette, France
Référent : CentraleSupélec

Thèse présentée et soutenue à Gif-sur-Yvette, le 05/02/2021, par

Shuoliang DING

Composition du Jury

Hamid KOKABI Professeur, Sorbonne Université, CNRS, GeePs, 75252, Paris, France	Président du jury
Dimitrios ANAGNOSTOU Maître de Conférences, Institute of Signals, Sensors and Systems, Heriot Watt University, Edinburgh, EH14 4AS, UK	Rapporteur & Examinateur
Philippe LE THUC Maître de Conférences, University Côte d'Azur / LEAT / CNRS UMR 7248, Sophia Antipolis, France	Rapporteur & Examinateur
Mauro FELIZIANI Professeur, Università degli Studi dell'Aquila | Università dell'Aquila · Department of Industrial and Information Engineering and Economics	Examinateur
Yann LE BIHAN Professeur, University of Paris-Saclay, CentraleSupélec, CNRS, GeePs, 91192, Gif-sur-Yvette, France	Examinateur
Lionel PICHON Directeur de Recherche, University of Paris-Saclay, CentraleSupélec, CNRS, GeePs, 91192, Gif-sur-Yvette, France	Directeur de thèse
Stavros KOULOURIDIS Maître de Conférences, Electrical and Computer Engineering Department, University of Patras, Patras, Greece	Co-encadrant & Examinateur

Thèse de doctorat

NNT : 2021UPAST006

ECOLE DOCTORALE N°575
• Electrical, Optical, Bio : Physics And Engineering (EOBE)

Titre : Conception d'un système de transmission d'énergie sans fils pour les implants autonomes biomédicaux

Mots clés : Antenne implantée ; Industrial, Scientific and Medical Band ; Transmission d'énergie sans fil ; Biotélémétrie ;Rectenna

Ce travail est destiné à concevoir un système de transmission d'énergie sans fil complet, qui est constitué par les éléments suivants : une antenne externe pour fournir la puissance ; une antenne bi-bande circulaire miniaturisée implantée pour la réception d'énergie et un circuit de redressement—doubleur de tension. Quelques capteurs issus de la littérature sont aussi mentionnés et discutés. Le scénario complet garantit l'intégrité du système et donc valide sa faisabilité. En comparant avec des publications récentes, le système proposé dans cette thèse possède la taille électrique la plus petite. Même si l'efficacité de transmission peut être considérée comme basse, le travail montre que le système est capable d'alimenter plusieurs types de capteur sans difficulté.

La partie d'antenne, afin de maximiser la puissance transmise, fonctionne à 915 MHz selon la contrainte internationale de puissance de transmission. L'antenne est circulaire et a un diamètre de 11 mm. Plusieurs améliorations ont été réalisées pendant la procédure de conception, par exemple, réduire la taille du patch pour qu'il soit isolé du tissu autour. En plus, dans l'intention d'envisager toutes les améliorations possibles de l'antenne, le rôle et l'influence de chaque paramètre sont détaillés. Plusieurs résultats numériques importants sont présentés et le scénario de la transmission est évalué. Quelques éléments annexes du système, comme l'antenne externe et le réflecteur sont aussi étudiés et la composition l optimisée est déterminée. Les contraintes de sécurité sont également satisfaites. Le rendement de l'antenne dans le corps humain peut atteindre -35 dB pour une distance de 400mm. Enfin, une méthode mathématique récente est présentée. Elle est capable d'analyser la sensibilité et d'estimer des résultats de simulation à moindre coût.

Pour la partie de circuit, plusieurs idées sont proposées et comparées afin d'atteindre la meilleure performance. Les caractéristiques électromagnétiques de tous les éléments du circuit sont prises en compte afin d'obtenir des valeurs optimales. Une simulation totale (antenne et circuit ensemble) est également réalisée. Avec l'analyse antenne-circuit, le système complet est capable de recevoir 56.9 µW pour une distance de transmission de 400 mm et 233.6 µW pour 200 mm avec la configuration optimisée. Le scénario a été finalisé tout en présentant des capteurs de basse consommation.

Finalement, plusieurs mesures ont été réalisées pour valider le comportement du système. Pendant la première mesure, un certain nombre de problème ont été diagnostiqués et certaines hypothèses ont été étudiées. Ensuite, elles ont été prouvées correctes et la deuxième mesure s'est avérée une réussite. Différents environnements de simulation ont été comparés et les résultats ont été discutés. Le circuit a également été mesuré.

Université Paris-Saclay
Espace Technologique / Immeuble Discovery
Route de l'Orme aux Merisiers RD 128 / 91190 Saint-Aubin, France

Title : Design of a Power-Efficient Radiative Wireless System for Autonomous Biomedical Implants

Keywords : Implantable antenna; Industrial, Scientific and Medical Band; Wireless power transmission; Biomedical engineering; Rectenna

The work in this thesis is dedicated to designing a complete wireless power transmission system including an external power delivery patch antenna, a miniaturized dual-band circular embedded power reception dipole antenna, and a voltage doubler rectifying circuit. Some sensors in the previous literature are mentioned and discussed as well. This entire scenario guarantees the completeness of this system and thus validates its feasibility. Comparing to the previous literature, the system in this thesis has the smallest electrical size. Although the total efficiency seems as low as in other designs, our work proves that it could support several kinds of sensors without any difficulty.

For the antenna part, in order to have the maximum power transmitted, the power transmission operates at 915 MHz because of the power limit standards. The circular antenna has a diameter of 11 mm. Several improvements have been made during the design process, including reducing the patch size and isolate it from the surrounding tissue, in order to be more suitable for use. Also, in order to simplify any improvement in the future, the influence of each antenna's parameters is detailed. Several important simulation results are presented and the transmission scenario is evaluated. Different accessories such as: the external antenna and the reflector are also evaluated. The most optimized parameter for the reflector is found and safety issues are considered. The in-body transmission efficiency could reach -35 dB (around 0.03%) for 400mm distance. At last, a new mathematical method with the capability of analyzing the parameters' sensitivity and predicting results is introduced.

For the circuit part, several designs are proposed and compared in order to achieve the best performance. The electromagnetic properties of all parts in the circuit are considered and taken into account. Each component is altered for the purpose of finding the optimized value and an antenna-circuit simulation is done. Through antenna-circuit combination analysis, with the most optimized configuration, the entire system is able to receive 56.9 μW for 400 mm power transmission distance and 233.6 μW for 200 mm power transmission distance. By introducing the sensors, the entire scenario has been completed. Link budget has been analyzed as well.

Finally, several measurements are done in order to validate the performance of the system. During the first measurement, several issues were found (tissue contact, fat dissipation, etc) and some assumptions were made. Then the assumptions were proved to be right and the second measurement was a success. Different operation environments were compared and differences were discussed. The circuit was measured as well.

The entire system could be used in some scenario where miniaturized self-powering medical implants could be useful.

Université Paris-Saclay
Espace Technologique / Immeuble Discovery
Route de l'Orme aux Merisiers RD 128 / 91190 Saint-Aubin, France

Résumé

Le chapitre 1 présente tout d'abord l'idée générale des dispositifs médicaux implantables (IMD) et des dispositifs médicaux portables (WMD), et discute de leur importance dans la société moderne. Les méthodes actuelles de charge électrique sans fil sont présentées, y compris les méthodes électriques et non électriques. De nombreuses méthodes ont été utilisées par les chercheurs et trois d'entre elles sont basées sur les théories électromagnétiques standards : La charge inductive, la résonance magnétique fortement couplée et le transfert d'énergie par micro-ondes. Après des années de développement, le rayonnement a suffisamment mûri pour devenir un choix pour la transmission d'énergie sans fil. Contrairement aux autres méthodes de transfert d'énergie, la méthode de rayonnement présente plus d'avantages et convient mieux à certaines utilisations.

Tout d'abord, les implants peuvent être extrêmement petits par rapport à ceux utilisés par d'autres méthodes. L'antenne intégrée utilisée par la méthode de rayonnement pourrait avoir un rayon de quelques millimètres seulement, voire moins. En effet, dans les plages de fréquences plus élevées, la longueur d'onde est plus petite et les implants pourraient donc être physiquement plus petits avec la même proportion de longueur d'onde (longueur électrique). Avec des dispositifs plus petits, ces implants pourraient être plus "implantables" sans gêner le mouvement du patient et en minimisant les éventuels effets secondaires négatifs causés par l'implantation, mesurer certains paramètres biologiques qui ne pourraient pas être mesurés à la surface de la peau.

Deuxièmement, la méthode des radiations n'a pas de limites très strictes pour les critères de positionnement pendant le processus de transmission de l'énergie. Si l'implant est installé 24 heures sur 24 chez un patient, il n'est pas pratique pour lui de se rendre à l'hôpital ou dans un lieu spécifique uniquement pour le rechargement. Cependant, lorsqu'il se recharge à domicile, il est pratiquement impossible pour les patients de respecter très strictement les règles de positionnement pendant le processus de recharge. Par conséquent, un système de recharge robuste ou presque immunisé contre une légère désorientation est nécessaire. Néanmoins, ni la charge par induction en champ proche ni la SCMR ne sont en mesure d'accomplir cette mission. Ces deux méthodes perdent une grande partie de leur efficacité en cas de désorientation ou de mauvais positionnement.

Néanmoins, toute pièce de monnaie a deux côtés. La méthode par rayonnement a ses propres limites. Malgré sa taille minuscule et pratique, son efficacité est généralement faible par rapport aux méthodes de champ proche. Cela rend la charge par rayonnement presque impossible pour les stimulateurs cardiaques ou tout autre

gros appareil. Toutefois, le stimulateur cardiaque n'est pas la seule cible. Nous verrons en détail qu'avec des capteurs à faible consommation d'énergie, comme dans les littétatures, il est possible de construire de petits systèmes auto-alimentés de mesure et de transmission de données. Il s'agit d'un scénario complètement différent de celui du stimulateur cardiaque, mais il est toujours réalisable et promis à un bel avenir.

Un système de transmission d'énergie médicale par radiofréquence (RF) se compose normalement de deux parties : Une antenne pour capter l'énergie et un circuit pour convertir le courant alternatif (CA) en courant continu (CC). Ces dernières années, de nombreuses équipes de recherche ont étudié les antennes de transfert d'énergie sans fil dans les implants biomédicaux.

Depuis que l'équipe de L.C. Chirwa a publié en 2003 une première étude sur les performances d'une source implantée dans l'intestin humain sous différentes fréquences, de nombreuses équipes de recherche ont successivement réalisé leurs propres conceptions ou analyses. L'équipe de Meng de Hongkong a mené des recherches sur la façon dont l'intensité des ondes électromagnétiques varie en fonction de l'emplacement et de la position de la source rayonnante ; Rahmat-Samii et al. [29] de l'Université de Californie à Los Angeles ont proposé une antenne PIFA (Planar Inverted-F Antenna), puis ont exploré la différence entre le modèle à une couche et celui à trois couches en le faisant communiquer avec un dipôle externe. La même année, Furse et al [30] de l'Université de l'Utah ont étudié l'impact du matériau du substrat de l'antenne et ont comparé deux types de PIFA, découvrant que la PIFA en spirale avait de meilleures performances que la PIFA en serpentin. Soontornpipit [31], de la même université, a également réussi à utiliser des méthodes d'algorithme génétique pour concevoir de nouvelles antennes. M. Zada et al. ont également conçu deux antennes à double bande (une dipôle et une PIFA) qui fonctionnent à 403 MHz et 915 MHz [32]. Ces antennes sont destinées à être implantées dans la bouche, où le tissu musculaire n'est pas très épais et où la profondeur d'implantation n'est que de 3 mm environ. L'équipe de recherche de Topsakal [33], de l'université du Mississippi, a publié ses études sur les propriétés électriques de la peau de rat et les compositions du gel imitant la peau, qui pourrait servir d'instruction pour les mesures.

Il existe de nombreux types d'environnements de simulation qui peuvent représenter un tissu biologique : Modèle de tissu monocouche ; modèle de muscle 2/3 ; modèle humain multicouche et modèle humain numérique précis.

Le modèle le plus couramment utilisé est le cube à simple peau. D'après la comparaison des publications précédentes, de nombreuses équipes de recherche ont choisi ce modèle pour l'environnement de simulation en raison de sa simplicité, afin d'économiser le temps de calcul. Néanmoins, ce modèle est trop simple pour représenter le tissu humain, comme le montrent les statistiques du tableau dans l’article.

De plus, la couche de peau est trop fine pour tout type d'implantation et n'est donc pas réaliste pour les simulations.

Le modèle multicouche est un modèle plus précis qui simule l'environnement des tissus humains. Les tissus les plus couramment utilisés dans les couches sont les os, les muscles, la graisse et la peau. Le modèle multicouche est capable de simuler la réflexion entre les différentes couches qui existent dans l'application réelle. De nombreuses équipes de recherche ont déjà appliqué ce modèle et il est considéré comme un bon compromis entre la précision du modèle et le temps de calcul.

Le modèle de muscle 2/3 est également présent dans la littérature. Il s'agit également d'un modèle monocouche mais avec un "tissu" qui a des propriétés électriques spéciales équivalentes à celles du modèle multicouche. C'est un modèle plus avancé que le modèle de peau monocouche mais pas aussi précis que le modèle multicouche. Par exemple, un modèle de muscle 2/3 à 402 MHz a une permittivité relative de 42,91 et une conductivité de 0,65. Ces valeurs sont les propriétés électriques "équivalentes" du corps humain si l'on considère le corps humain réel comme un tissu homogène. Cependant, il n'est pas aussi précis que le modèle multicouche car il ne peut simuler le tissu humain qu'autour d'une certaine fréquence et certaines réflexions entre les couches sont négligées.

Le modèle le plus précis et le plus exact est un modèle humain en 3D. Ce modèle est normalement digne de confiance pour les simulations de conception d'antennes puisque plusieurs modèles existants ont été créés à partir de scans d'imagerie par résonance magnétique (IRM).

Enfin, le circuit redresseur doit s'adapter à l'antenne afin d'obtenir les meilleures performances.

L'objectif de la thèse est donc déterminé et certaines contraintes de conception sont présentées :

Tout d'abord, pour la plupart des conceptions, les antennes sont encore de grande taille, ce qui représente un grand défi pour les patients et les chirurgiens. Une antenne implantée de grande taille peut gêner les mouvements du patient et causer des dommages inutiles. Il existe des antennes suffisamment petites pour être implantées, mais elles fonctionnent à des fréquences élevées. Les hautes fréquences entraînent des pertes plus importantes, ce qui peut saturer le DAS (voir chapitre 2) avec seulement une faible puissance délivrée. Deuxièmement, de nombreux modèles d'antennes ne disposent pas d'un circuit redresseur approprié [34-49]. La puissance RF ne peut être utilisée directement par aucun capteur et un circuit redresseur non adapté peut fortement atténuer l'efficacité de la transmission de puissance. Même pour les conceptions qui ont leurs propres circuits redresseurs, les circuits ne sont pas simulés

et testés avec un niveau de puissance d'entrée réel, ce qui peut conduire à un résultat complètement différent. Troisièmement, l'environnement de simulation de nombreux travail est une boîte de peau qui n'est pas assez réaliste (voir tableau 1.2). Cette différence d'environnement peut entraîner un décalage important de la fréquence de résonance et l'efficacité de la transmission serait sérieusement réduite à une fréquence non résonante. Certaines recherches ont abordé la question des implants dans la couche de peau, ce qui n'est pas non plus réalisable en raison de l'épaisseur de la peau. Enfin, pour leurs mesures, la plupart d'entre elles utilisent un fantôme de tissu humain. Le fantôme est pratique mais ne peut simuler le tissu humain qu'à une fréquence fixe. Pendant les mesures, il est très probable que les antennes fabriquées ne résonnent pas aux fréquences prédéfinies, avec un léger décalage. Avec ce phénomène, le fantôme n'est pas un choix approprié pour les mesures.

Sur la base des discussions précédentes, l'objectif de la thèse devient clair. Tout d'abord, l'antenne ainsi que le circuit redresseur doit occuper peu d'espace sans perdre beaucoup d'efficacité. Un choix judicieux des fréquences de fonctionnement et de la forme de l'antenne est nécessaire. Ensuite, un circuit redresseur adapté doit être conçu, simulé et testé avec l'antenne. Un système entièrement conçu peut minimiser la perte de désadaptation et optimiser la puissance reçue par la charge. Ensuite, un environnement de simulation réaliste doit être construit pour éviter les imprécisions dans les conceptions. En outre, un modèle de simulation adéquat doit être défini en utilisant la quantité optimale de calcul et sans perdre sa précision. Enfin, la mesure doit être effectuée dans un environnement biologique plus réaliste que le fantôme.

En conclusion, pour construire un système de transmission d'énergie sans fil aussi efficace, les critères suivants doivent être remplis :

- Petite taille mais grande efficacité de transmission
- L'antenne et le circuit redresseur doivent être conçus et adaptés en respectant toutes les contraintes de sécurité (et autres) nécessaires.
- Système testé dans un environnement réaliste

Le chapitre 2 est consacré à la conception de l'antenne implantée. Dans ce chapitre, tout d'abord, la raison pour laquelle ces deux fréquences de fonctionnement sont choisies est expliquée. Ensuite, une antenne circulaire miniaturisée est conçue pour une application biomédicale sans fil dans le corps profond. L'antenne est circulaire et miniaturisée, car elle n'a qu'un rayon de 5,5 mm. Elle possède deux fréquences de résonance différentes : 403 MHz (bande MedRadio) et 915 MHz (bande ISM). L'impact des différents paramètres de l'antenne (ex. le rayon de la fente) est discuté. Le modèle de tissu humain cylindrique à trois couches (os 25 mm, muscle 25 mm-47,5 mm, et peau 47,5 mm-50 mm) est utilisé dans la simulation. Pour chaque fréquence de

résonance de l'antenne, le gain de l'antenne (dans le corps) est de -33,65 dB pour la bande de 403 MHz et de -29,45 dB pour la bande de 915 MHz.

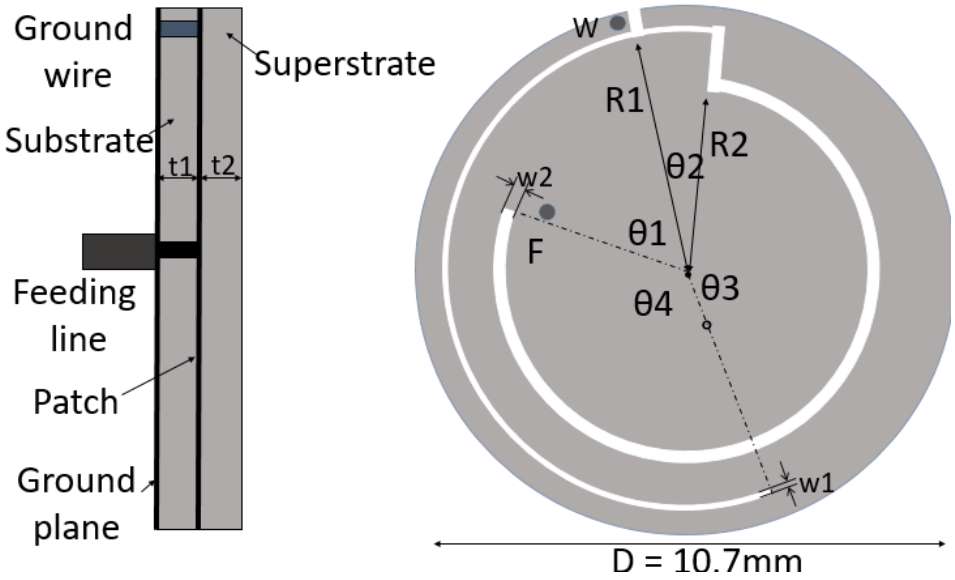

Figure 1 Géométrie de l'antenne circulaire conçu

Tableau 1 Paramètres de l'antenne

Nom du paramètre	Valeur (mm)	Nom du paramètre	Valeur (deg)
R1	4.9	*θ1*	70
R2	3.76	*θ2*	18
w1	0.15	*θ3*	163
w2	0.32	*θ4*	109
t1	0.64		
t2	0.64		
D	10.7		

La conception de l'antenne a fait l'objet de plusieurs phases et a été optimisée. Dans ce chapitre, les détails et les raisons de chaque amélioration sont expliqués. De plus, afin que les lecteurs puissent comprendre la procédure de conception, l'impact de chaque paramètre de la conception est étudié en détail. En outre, afin de choisir la meilleure fréquence de transmission de puissance, divers calculs et simulations sont effectués dans différents types d'environnement tissulaire. Ensuite, les résultats numériques 1D et 2D, y compris S11, le diagramme de rayonnement, le ratio d'absorption spécifique (SAR) et la polarisation sont tous présentés pour cette conception d'antenne. Enfin, quelques instructions de manipulation du logiciel sont présentées à la fin du chapitre.

Le chapitre 3 traite des problèmes d'interaction des ondes entre l'antenne conçue au chapitre 2 et l'antenne d'émission externe. Tout d'abord, l'expression numérique du rendement de transmission de puissance, qui simplifie et clarifie la norme de référence de la transmission, est présentée. Ensuite, deux "célèbres" règlements sur la transmission de puissance qui stipulent la limite d'émission de puissance sont présentés.

Ensuite, la structure de transmission est décrite précisément et deux composants externes pour la charge sont discutés : l'antenne externe et le réflecteur.

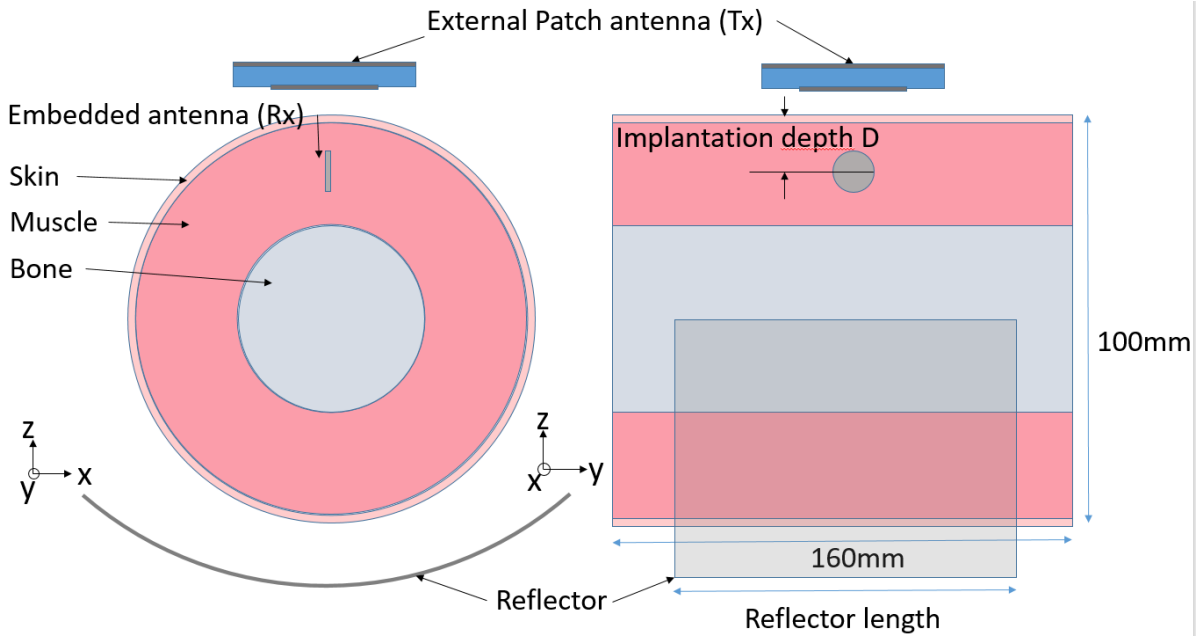

Figure 2 Conception de la liaison de transmission de puissance

Divers résultats numériques sont présentés concernant différents problèmes de positionnement et de réflecteur afin d'optimiser la conception de la transmission : le choix de l'antenne externe, la conception du réflecteur, le positionnement de l'antenne intégrée, la profondeur d'implantation, la distance de transmission et la géométrie, le matériau du réflecteur. Tous ces éléments sont essentiels pour l'optimisation du lien de transmission. Les questions de SAR sont également discutées pour assurer la sécurité du système.

Enfin, une analyse de sensibilité est réalisée sur la base de ce lien de transmission en identifiant et en comparant l'impact de différents paramètres. L'analyse permet de prédire précisément les résultats à partir de quelques configurations possibles étudiées sans perdre trop de précision en créant un modèle numérique. Elle permet également de diagnostiquer le paramètre le plus influent pour le système.

Le chapitre 4 se concentre sur la conception du circuit redresseur pour l'antenne embarquée. Tout d'abord, la topologie du circuit est présentée, y compris les différentes conceptions du circuit d'adaptation d'impédance. Ensuite, la méthode de

combinaison antenne-circuit est également présentée, suivie de la conception imprimée du circuit. Ce circuit redresseur est utilisé pour redresser la puissance reçue par l'antenne embarquée (voir la figure 3.7). Pour le confort du patient, l'ensemble du système (antenne + circuit) doit occuper le moins d'espace possible à l'intérieur du corps humain. De plus, d'après le circuit de rayonnement microbande de l'antenne présenté au chapitre 2, le lobe principal de l'antenne se trouve vers son côté latéral. Par conséquent, une solution possible pour le positionnement du circuit est d'ajouter une autre couche à l'antenne (au-dessus du superstrat ou en dessous du substrat).

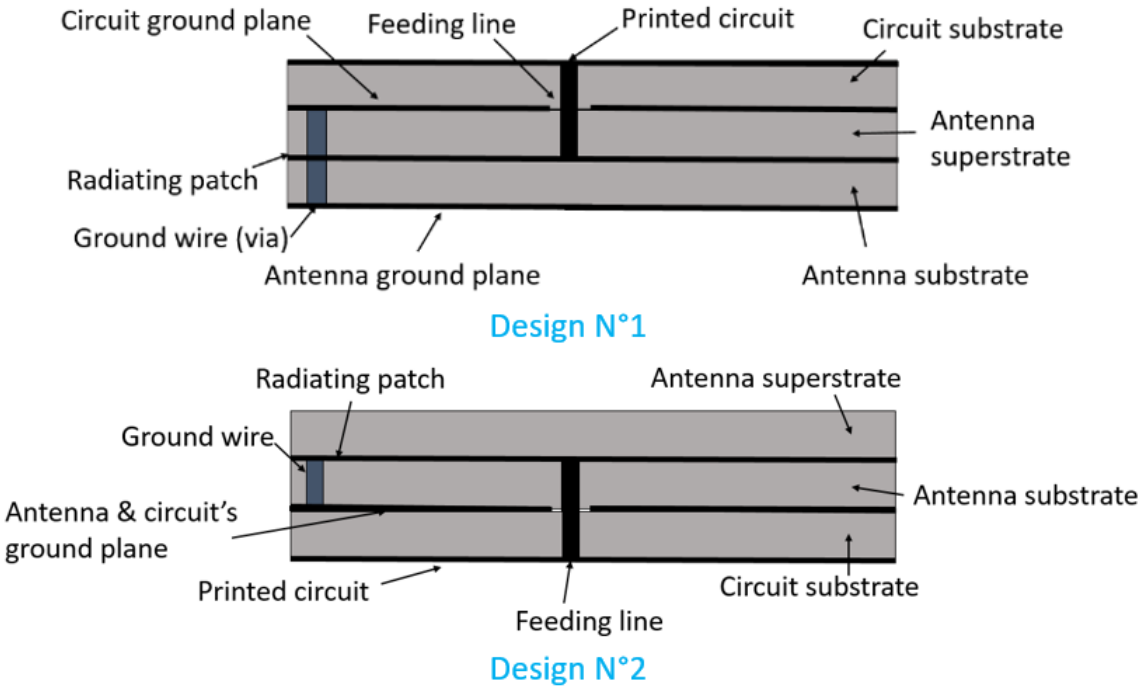

Figure 3 Deux conceptions différentes de combinaison antenne-circuit

Ensuite, plusieurs conceptions possibles sont discutées et comparées. Ensuite, nous utilisons plusieurs comparaisons pour trouver la conception la plus optimisée étape par étape : le type de circuit, le nombre d'éléments, le choix des diodes et même la valeur de la charge sont autant d'améliorations possibles. En raison de la valeur minuscule du composant, les largeurs et longueurs des lignes du circuit sont également prises en compte à cause de la capacité parasite. Plusieurs simulations sont effectuées en vue d'optimiser les performances du circuit. Pour chaque conception, l'efficacité du redressement et la tension de sortie de la charge sont comparées.

Enfin, nous devons intégrer le modèle d'antenne dans le modèle de circuit afin de simuler un cas plus réaliste. La simulation du circuit est basée sur la modélisation électromagnétique du circuit et des composants disponibles dans la bibliothèque ADS. Puisque la co-simulation entre ADS et CST n'est pas possible, il est possible d'intégrer l'antenne comme un bloc de paramètres S qui pourrait également représenter toutes les caractéristiques de l'antenne pour ce type d'utilisation. Comme mentionné dans le

chapitre 3, la puissance d'alimentation maximale autorisée pour une antenne dans la bande 915 MHz est de 30 dBm.

Les résultats de la simulation pour le système de rectenna global sont présentés dans les figures 4 et 5, dans lesquelles la relation entre l'efficacité du redressement, la tension de sortie et la puissance d'entrée dans l'antenne externe est présentée pour différentes distances de transmission. Dans cette simulation, les pertes par désadaptation entre l'antenne et le circuit sont également prises en compte. Comme mentionné au chapitre 2, l'impédance de l'antenne à 915 MHz est d'environ 80 Ω. Comme l'antenne est directement connectée au circuit (plus de câble coaxial), le circuit doit être directement adapté à l'antenne.

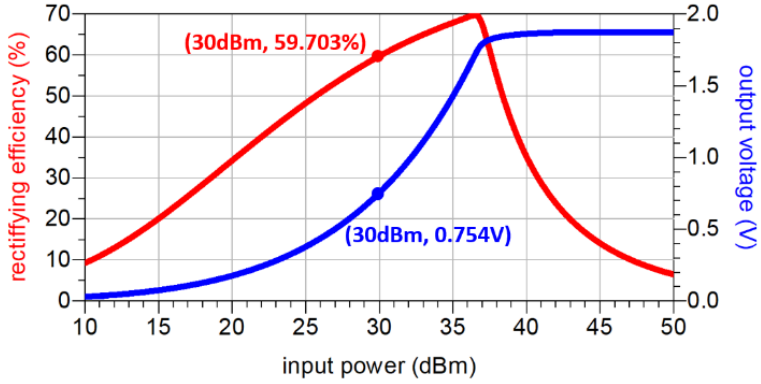

Figure 4. Efficacité globale du système et tension de sortie lorsque le patch externe est à une distance de 400 mm (efficacité de redressement = 59,7 %, tension de sortie = 0,75 V avec une puissance d'entrée de 30 dBm au niveau du patch et pour une charge de 10 kΩ).

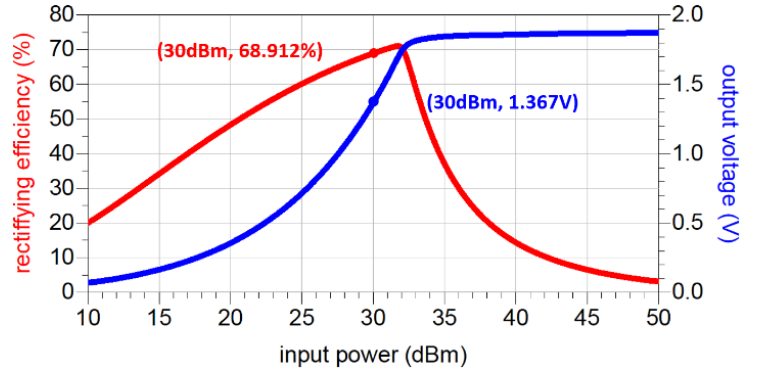

Figure 5. Efficacité globale du système et tension de sortie lorsque le patch externe est à une distance de 200 mm (efficacité de redressement = 68,9 %, tension de sortie = 1,37 V avec une puissance d'entrée de 30 dBm au niveau du patch et pour une charge de 8 kΩ.

Lorsque l'antenne patch externe est alimentée par une puissance de 30 dBm et rayonne à une distance de 400mm (distance de transmission), l'efficacité du circuit est de 59,7%. La valeur de la charge 10 kΩ est choisie afin de maximiser l'efficacité de la

transmission de puissance. La tension continue au niveau de la charge est de 0,75 V et la puissance consommée par la charge est de 56,9 µW à cette distance.

Lorsque l'antenne patch n'est éloignée que de 200 mm (distance de transmission), l'efficacité de redressement du circuit est portée à 68,9 % en raison de l'augmentation de la puissance reçue par l'antenne implantée. La tension de sortie à la charge est de 1,37 V et la puissance continue redressée finale est de 233,6 µW.

D'après le calcul précédent, la puissance qu'un seul système de transmission de puissance dans ce document pourrait recevoir pour différentes distances de transmission est indiquée dans le tableau 1. Une profondeur d'implantation de 16 mm est prise comme exemple ici.

Tableau 1 Puissance reçue à différentes distances

Distance de transmission (mm)	**S_{21}@ 915 MHz**	**Efficacité du circuit (%)**	**Puissance à la charge (µW)**	**Puissance pour l'échange d'informations (µW)**	**Distance maximale entre les patchs externes pour l'échange d'informations (mm)**
200	-36.1	68.9	233.4	23.3	1300
400	-40.4	59.7	56.9	5.7	850
500	-42.4	54.5	28.9	2.9	600

Comme le montre le tableau 1, le système de transmission de puissance est capable d'alimenter plusieurs capteurs en termes de puissance. Les résultats sont calculés par des simulations. Ils sont basés sur la puissance reçue par l'antenne implantée avec la valeur de distance correspondante et les résultats d'efficacité de redressement & de tension de sortie avec la puissance reçue correspondante. Dans les deux simulations, les impédances des ports sont normalisées à 110 Ω et il est supposé que seulement 10% de la puissance redressée est utilisée pour alimenter l'échange d'informations et que tous les ports sont parfaitement adaptés.

Comme calculé, il y a toujours une distance maximale correspondante entre le dipôle de réception et la surface de la peau afin d'assurer la connexion (énergie reçue par le dipôle de réception ≥ -90dBm qui est la puissance minimale qui peut être reçue par les téléphones mobiles sans perte d'information) pour chaque profondeur d'implantation différente.

Pour les valeurs du tableau 1, la puissance d'entrée du circuit redresseur n'est pas de -20 dBm. Cette puissance varie en fonction des distances de transmission. Cependant, en raison des normes d'émission de puissance maximale autorisée, la puissance émise par l'antenne externe ne doit pas être supérieure à 30 dBm. Par conséquent, dans tous les résultats présentés dans le tableau 1, la puissance émise par l'antenne externe est fixée à la valeur maximale de 30 dBm. La valeur de la puissance reçue dans le tableau 1 montre qu'elle pourrait supporter n'importe lequel des capteurs mentionnés dans ce chapitre. Cependant, un amplificateur de tension pourrait encore être nécessaire pour atteindre la tension d'alimentation des capteurs et sera testé à l'avenir.

Enfin, comme au chapitre 2, le logiciel de simulation de circuits micro-ondes est présenté et certaines étapes clés sont expliquées.

Le chapitre 5 traite des résultats des mesures de l'antenne et du circuit. Les équipements utilisés, tels que l'analyseur de réseau vectoriel (VNA) et le câble coaxial RF, sont présentés. Pour la fabrication de l'antenne, deux méthodes de fabrication sont généralement utilisées : La méthode laser et la méthode mécanique. La taille du paramètre de l'antenne étant trop petite (0,15 mm de largeur de la fente) et la machine laser ne pouvant offrir qu'une précision minimale de 0,1 mm, la gravure mécanique est donc choisie pour cette fabrication.

Afin de simuler l'environnement du "bras", il faut utiliser un fantôme cylindrique. Une tasse en plastique dont l'épaisseur est négligeable est utilisée pour maintenir la forme du "bras".

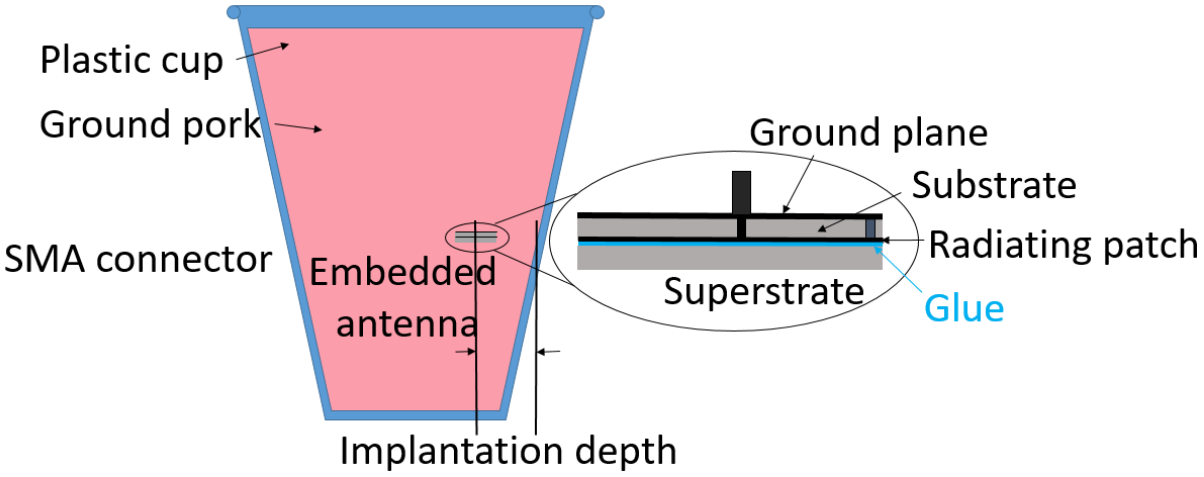

Figure 6 Scénario de mesure avec le gobelet en plastique

L'antenne est insérée verticalement dans le tissu de porc haché puisque son lobe principal est parallèle à la surface de l'antenne. Ensuite, certains problèmes causés par la colle sont détectés. Le problème est ensuite résolu par plusieurs hypothèses et la simulation correspondante. Par conséquent, deux mesures différentes sont introduites,

la seconde tirant parti des problèmes rencontrés lors de la première mesure. De plus, la seconde mesure est réalisée dans une chambre anéchoïque.

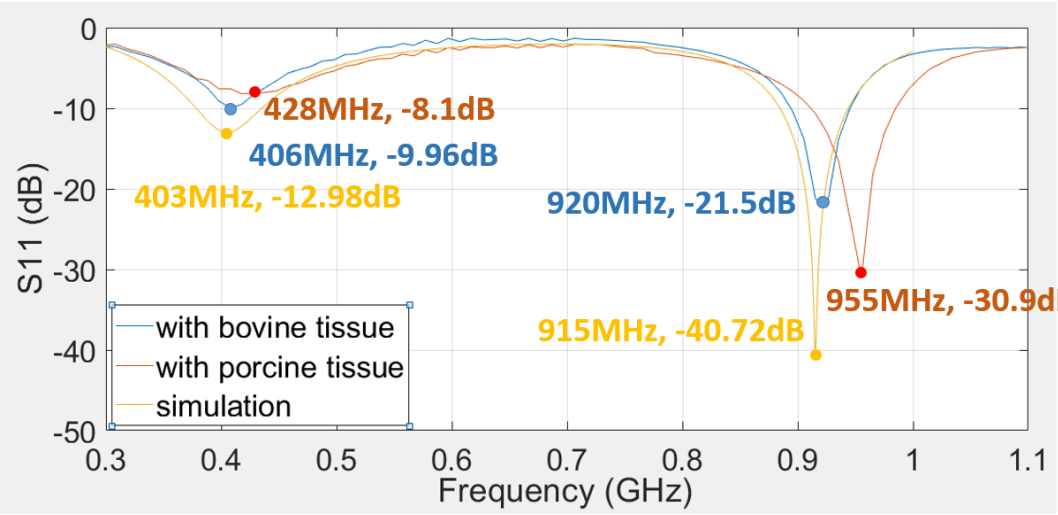

Figure 7 Coefficient de réflexion de l'antenne lorsqu'elle est incorporée dans différents types de tissus animaux, comparé aux résultats de simulation

Comme on peut le constater, les fréquences de résonance de l'antenne, lorsqu'elle est implantée dans des tissus bovins (5% de graisse), se déplacent légèrement vers des valeurs plus élevées, mais restent dans la bande autorisée. Ce décalage peut être causé par deux raisons possibles : Les 5% de graisse dans le tissu et les bulles d'air aléatoires qui existent parmi le tissu. Ces deux facteurs diminuent la permittivité du milieu et modifient la fréquence de résonance de l'antenne.

La viande de porc hachée contient 20 à 30 % de graisse ; la viande de bœuf hachée utilisée contient seulement moins de 5 % de graisse et la graisse a une permittivité plus faible que la viande maigre. Dans les simulations, un muscle humain homogène est utilisé comme environnement d'inclusion. Par conséquent, lorsque le tissu bovin (avec moins de graisse) est utilisé, les résultats sont plus proches de ceux de la simulation. Néanmoins, dans la vie réelle, les personnes ne présentant que 5 % de graisse ne sont pas si courantes, de sorte que les résultats obtenus en utilisant du porc haché sont plus proches de la réalité.

Le scénario de transmission est également mesuré. Et l'effet d'amélioration du réflecteur est validé. Le S21 est amélioré d'environ 7 dB avec la présence du réflecteur à 915 MHz, ce qui valide les résultats de la simulation du chapitre 3.

Le circuit est également mesuré avec son kit d'étalonnage spécial. L'impédance totale du circuit est d'environ 32-31j Ω, ce qui correspond presque à l'impédance standard de 50 Ω à 915 MHz. Le coefficient de réflexion est de -7,8 dB. La tension à la charge est mesurée à 0,07 V par un multimètre placé aux deux extrémités de la charge de 18 kΩ. Cette valeur présente une certaine différence avec les résultats de la

simulation, ce qui est probablement dû à la taille minuscule du circuit. L'impédance de mesure pourrait même être affectée par les différentes tailles du point de soudure.

Cependant, malheureusement, en raison des situations Covid-19, la mesure du système antenne-circuit n'a pas été réalisée. D'autres suggestions pour les recherches futures sont proposées :

1. La mesure de la combinaison antenne-circuit devrait être faite pour une validation plus précise du système. Cela n'a pas été fait pendant la thèse à cause de la situation de Covid-19 en France.
2. La méthode d'analyse de sensibilité présentée à la fin du chapitre 3 pourrait être largement développée.
3. Pour des utilisations réalistes, la graisse est toujours un problème pour l'implantation. Sa permittivité est beaucoup plus faible que celle des autres tissus humains et peut donc poser problème. La graisse pourrait être utilisée comme un matériau spécial "portable" pour la réfraction des ondes et pourrait ainsi contribuer à améliorer la transmission d'énergie.
4. Pour le circuit, un booster DC de faible puissance pourrait être appliqué afin d'augmenter la tension de sortie pour répondre à plusieurs autres cas.
5. Enfin, certaines expériences in vivo pourraient être réalisées.

Declaration

I hereby declare that, the contents and organization of this dissertation constitute my own original work and does not compromise in any way the rights of third parties, including those relating to the security of personal data.

Shuoliang DING
December 2020

Contents

List of Figures

List of Tables

Global introduction

General Introduction

It is estimated that the world population will reach 10-13 billion in the year 2100 and almost 30% of them will be over 60. Nowadays, with the population aging's acceleration and the development of human society, more and more people start to pay attention to their personal health. As we all know, the very first step for curing a disease is to diagnose it by health monitoring. Especially, with the Covid-19 issues recently, we realize that a real-time health monitoring system is of great importance because it could discover and treat the disease at the first stage and thus reduce mortality. However, the traditional health care device has always too many complicated wires and restricts the patient's freedom. For a long time, even now in the hospital, patients still have to wear heavy devices only to monitor their ECG (Electrocardiogram) even for just one day (see Figure 1).

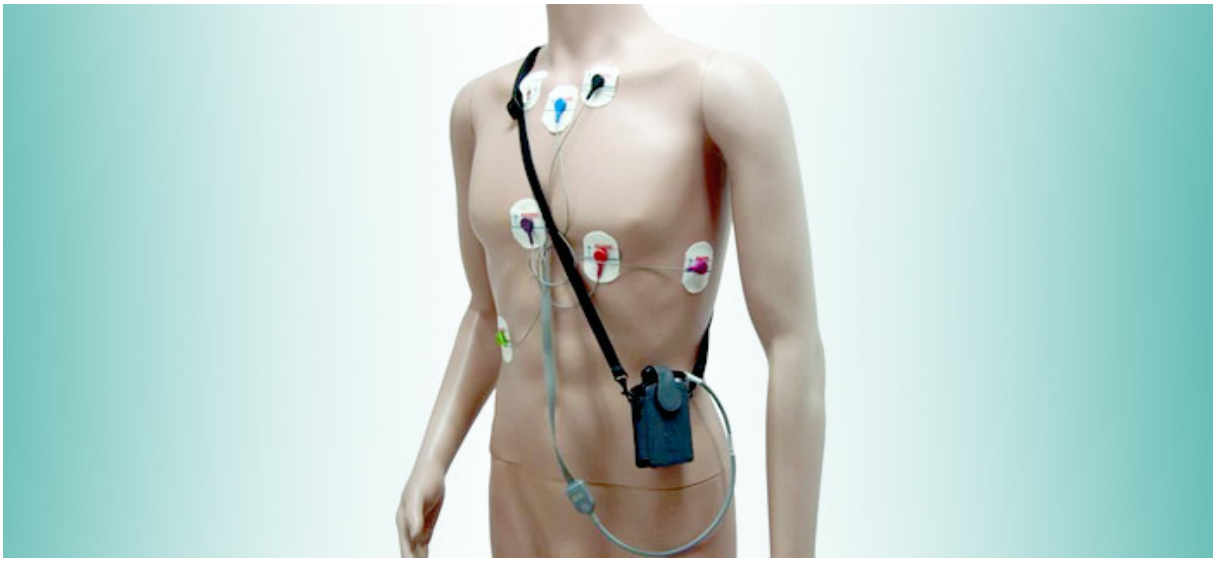

Figure 1. Cardio-monitoring system

As we have entered the Information Age, there has been a great evolution in the field of wireless communication and healthcare monitoring. So combining the two technologies is an inevitable choice. It will ultimately change the medical practice and healthcare.

A lot of research teams in the world have begun their own studies on the construction of an efficient wireless health monitoring system. In this context, GeePs (Group of Electrical Engineering in Paris) has proposed this thesis, financed by CSC (China Scholarship Council).

This project is also based on a collaboration between GeePs laboratory and the University of Patras, in Greece. Dr. Lionel Pichon in GeePs with Dr. Stavros Koulouridis decided to develop the subject together.

Thesis structure

We will present in detail a complete scenario of a biomedical wireless power transmission system by elaborating on each part of the system. The structure is as follows:

Chapter 1 introduces first the general idea of the Implantable Medical Devices (IMDs) and Wearable Medical Devices (WMDs); and discusses their importance in modern society. Current methods of wireless power charging are presented, including electrical and non-electrical methods. Then, three main electromagnetic harvesting techniques are introduced, with their background, main principle, and state-of-art. The radiation charging is especially detailed with recent literature and discussed. Afterward, some important information is listed and categorized, such as authorized operating frequency bands, antenna's information and their simulation/experimental environment. According to the weak points of the previously mentioned designs, the objective of the thesis is determined and some constraints of design are presented.

Chapter 2 is dedicated to the design of the embedded antenna. Firstly, the reason why these two operating frequencies are chosen is explained. Then the shape and dimension of the antenna are presented in detail. The antenna's design has been carried out through several phases and optimized. In this chapter, the details and reasons for each improvement are explained. Also, in order that the readers could understand the design procedure, the impact of each parameter in the design is studied in detail. Furthermore, in order to choose the best power transmission frequency, various calculations and simulations are performed in different kinds of tissue environment. Afterward, 1D and 2D numerical results, including S_{11}, radiation pattern, Specific Absorption Rate (SAR), and polarization are all presented for this antenna design. Finally, some software manipulation instructions are introduced at the end of the chapter.

Chapter 3 deals with the wave interaction problems between the antenna designed in Chapter 2 and the external transmitting antenna. First, the numerical expression of the power transmission efficiency, which simplifies and clarifies the reference standard of the transmission, is presented. Then two "famous" power transmission regulations which stipulate the power emission limit are introduced. After that, the transmission structure is precisely described and two external components for charging are discussed: the external antenna and the reflector. Various numerical results are presented regarding different positioning and reflector issues in order to optimize the transmission design. SAR issues are also discussed. Finally, a sensitivity analysis is performed based on this transmission link by identifying and comparing the impact of

different parameters. The analysis also allows accurate result prediction from a few possible studied configurations without losing too much accuracy.

Chapter 4 focuses on the design of the rectifying circuit for the embedded antenna. Firstly, the topology of the circuit is presented, including the different designs of the impedance matching circuit. Then the antenna-circuit combination method is also presented, which is followed by printed design of the circuit. Due to the tiny value of the component, the circuit line widths and lengths are also taken into account because of the parasitic capacitance. Several simulations are performed focusing on optimizing the circuit performance. Similarly to Chapter 2, the microwave circuit simulation software is introduced and some key steps are explained.

Chapter 5 addresses the measurement results of the antenna and the circuit. Equipment used is introduced before comparing two antenna's fabrication methods. The main differences between the simulation results and the measurements are discussed. Furthermore, two different measurements are introduced, as the second one takes advantage of the problems encountered during the first measurement. The circuit is measured as well. However, unfortunately, due to the Covid-19 situations, the antenna-circuit system measurement was not performed.

Chapter 1

State-of-art

1.1 Thesis context

A biomedical Wireless Sensor Network (BWSN) is a tiny and organized wireless nodes system with the capabilities of capturing, communicating, and processing information in order to support medical applications or provide healthcare services [1]. With its huge conveniences of wearability, an implantable BWSN can not only simplify the diagnostic procedures, but also help the patients with movement difficulties to accomplish their medical treatment in a way much more convenient. Nowadays, wearable medical devices (WMD) and implantable medical devices (IMD) have already been well developed and widely used. Examples include: Pacemakers, pill cameras, artificial arms, and other equipment that can measure human blood pressure or blood sugar in real-time. There are also more common wearable ones, like some wearable watches, which could monitor the heartbeat rate and blood pressure. Regardless of its accuracy problems, it shows the intention of people to monitor their health situation conveniently in their daily lives. For different purposes, these devices are used for body-centric communication [2] and other body parts of telemetry [3–5], or even wearable applications [6].

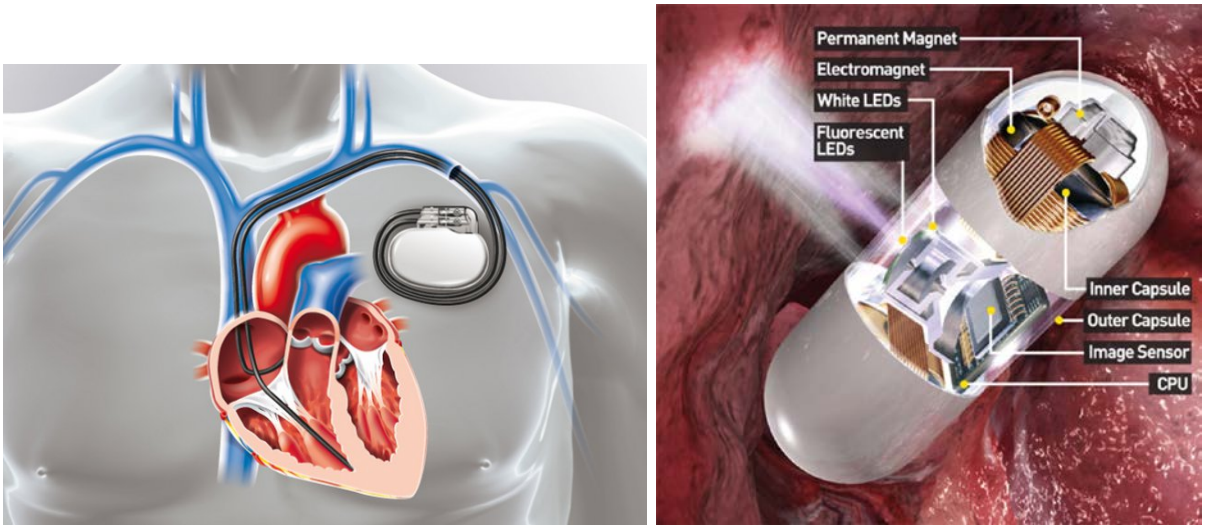

[a] [b]

Figure 1.1 Examples of IMDs [a] Pacemaker [b] Pill camera[7]

Compared to WMDs, IMDs are often more accurate and allow more functions due to direct contact inside the human body. The only disadvantage of an IMD is that once it is embedded inside the body, it cannot be taken out frequently. This means the powering of the IMD should be done without contact. However, due to the strong coupling between human tissue and electromagnetic waves, the human tissue is extremely lossy and absorbs most of the power passing by. So wireless charging for the IMDs is one of the main problems in the area of biomedical electromagnetic engineering.

1.2 State-of-art

In this section, the current development of biomedical wireless power transmission is introduced. Recently, researchers have come up with various ideas to capture energy from the surroundings. Figure 1.2 shows the different energy harvesting methods that exist [8].

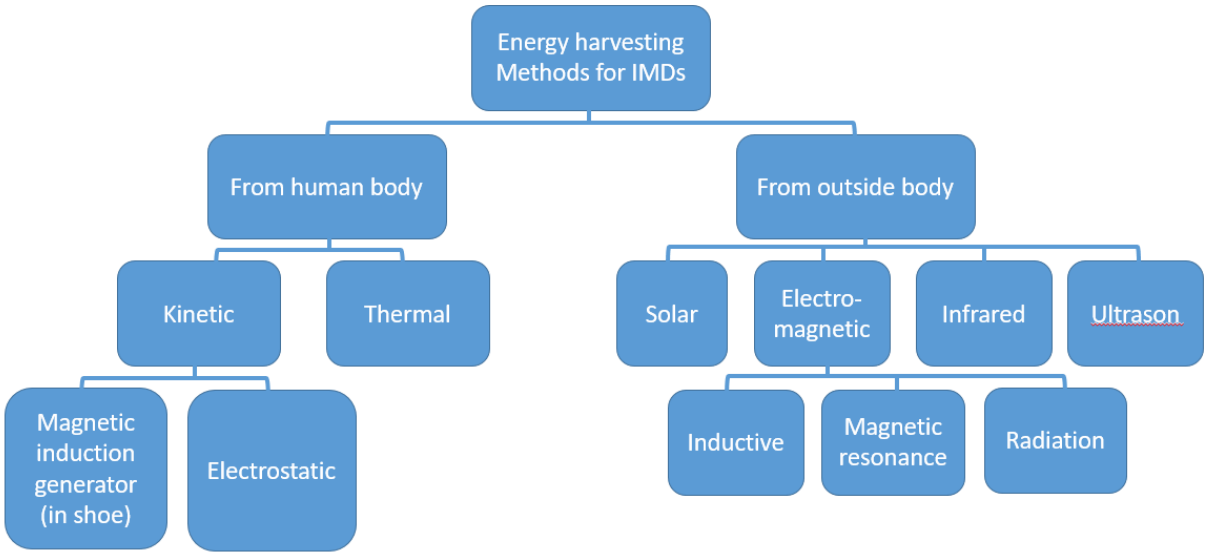

Figure 1.2 Energy harvesting method for IMDs in biomedical applications

Among these various power transmitting methods, we have to study the electromagnetic method which is more efficient, more convenient, and could harvest more power.

1.2.1 Transmission methods comparison

There are 3 main methods in EM wireless power transmission. We can classify them by their operating distance (and operating frequency): Inductive charging by magnetic coupling has the nearest operating range; strongly coupled magnetic resonance has a little bit longer range than the first method and radiation method which operates in the far-field range. Each method has its own advantages and disadvantages; it is important that we benefit from the advantages of each method by using them in appropriate ways.

1.2.1.1 Inductive charging

Using the magnetic coupling method for wireless power transfer has a long history. Early in the 19th century, Michael Faraday has already found the relationship between a magnetic field and electrical current [8]. After two centuries, there has been a great amount of interest in this near field wireless power transmission, including Near Field Communication (NFC) which is usually used for data exchange, fintech applications,

and various small devices, Radio Frequency Identification (RFID) which is usually used for access control and healthcare applications [9].

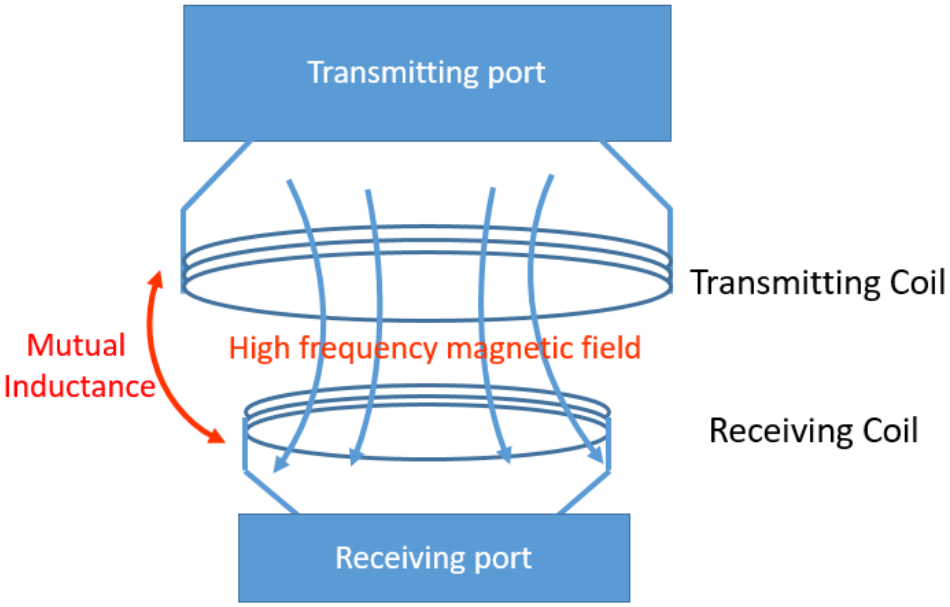

Figure 1.3 Working scenario for inductive charging

Due to the EM properties of the coils, the inductive charging method could only be used for low RF frequency range, since the parasitic capacity could be a problem in high frequency range.

However, with a short operating distance, the efficiency of an inductive charging system could be high enough, especially in the case of high power delivery, the efficiency could even achieve over 95% [10]. The 13.56 MHz band is a common choice for inductive charging since it is also the working frequency of the NFC connection in mobile phones. Many researchers have worked on transmitting data and power at the same time in this frequency band [11] [12]. Meanwhile, an electrocardiogram system using inductive charging was invented by the team of Ko et al. [13], etc. The inductive method has been very well developed in recent years.

1.2.1.2 Strongly coupled magnetic resonance

The Strongly Coupled Magnetic Resonance (SCMR) method, which can transfer power with excellent efficiency in the mid-range, has been developed in recent years rapidly. Mid-range, different from the radiative range, is still in the reactive near field range. However, it is around ten or twenty times longer than the traditional near field inductive charging range and thus is call mid-range [14].

The SCMR, as its name suggest, benefits from the syntony effect between the two identical resonators to transfer power. Conventional SCMRs usually employs four separate loops that occupy significant volume and they cannot be easily applied in IMDs [15]. The idea of conformal SCMR (CSCMR) was proposed in 2013 to resolve this

problem [16]. In [14], the research team of A. Kurs has proposed an air-air transmission by using two identical 60 cm diameter helices, and it has achieved an efficiency of 40%. However, both the conventional SCMR and the CSCMR provide optimum transmission efficiency at transmission distances in relation to the size of the resonators [17]. Beyond this optimal transmission range, the efficiency of SCMR drops very quickly, which is still a challenge for the patient's movement.

1.2.1.3 Microwave power transfer

Despite the two previous methods that work in the nearfield, radiation (radiative transfer) is the only method whose operating field is in the far-field range. The ability to transmit power by radiation has been discovered since the early work of Heinrich Hertz [18]. Hertz demonstrated the propagation of the electromagnetic waves in free space by using a complete system with a spark gap to generate high-frequency power and to detect it at the receiving end. This is the very first experience of wireless power transmission by radiation.

After years of development, radiation has matured enough to become a choice for transmitting power wirelessly. Different from other power transfer methods, the radiation method has more advantages and is more suitable for certain uses.

First of all, the implants could be extremely small as compared to those used with other methods. While inductive charging and SCMR have implants of a radius of several centimeters to ensure the transmitting efficiency [19] [20] [21], the embedded antenna used by the radiation method could be only of a few millimeters radius or even smaller [1] [22] [23]. This is because in higher frequency ranges, the wavelength is smaller and thus the implants could be physically smaller with the same proportion of the wavelength (electrical length). With smaller devices, these implants could be more "implantable" without hampering the patient's movement and minimizing any possible negative side effects caused by implantation, measure some biological parameters that could not be measured on the skin surface.

Secondly, the radiation method does not have very strict limits for positioning criteria during the power transmission process. If the implant is embedded 24h a day in a patient, it is not convenient for them to go to a hospital or any specific location just for charging. However, when charging at home, it is nearly impossible for patients to obey very strictly any positioning rules during the charging process. As a consequence, a charging system that is robust or nearly immune to slight disorientation is necessary. Nonetheless, neither near field inductive charging nor SCMR is able to accomplish the mission. These two methods lose a great amount of efficiency with any disorientation or misplacement.

Nevertheless, every coin has two sides. The radiation method has its own limits. Despite the convenient tiny size, the efficiency is usually low as compared to the near field methods. This almost makes radiation charging impossible for pacemakers or any other big devices. However, the pacemaker is not the only target. It will be presented in detail that with some low power-consuming sensors, as in [24], it is possible to build some small self-powered systems of measuring and data transmitting. It is a completely different scenario from the pacemaker case but feasible and has a bright future.

1.2.2 Antenna power transmission

A Radio Frequency (RF) medical energy transmission system normally consists of two parts: An antenna for capturing energy and a circuit for converting alternating current (AC) power to direct current (DC) power. In recent years, many research teams have studied wireless power transfer antennas in biomedical implants.

Since the team of L.C. Chirwa [25] has published an early study about the performance of an implanted source in the human intestine under different frequencies in 2003, many research teams have carried out successively their own designs or analyses [26-27]. The team of Meng [28] from Hongkong has carried out research about how the intensity of electromagnetic wave varies according to the different location and position of the radiating source; Rahmat-Samii et al. [29] from the University of California at Los Angeles proposed a PIFA (Planar Inverted-F Antenna), then explored the difference between one-layer and three-layer model by making it communicating with an external dipole. In the same year, Furse et al. [30] from the University of Utah investigated the impact of the antenna's substrate material and compared two kinds of PIFA, finding out that the spiral PIFA has better performance than the serpentine one in his case. Also, Soontornpipit [31] from the same university succeeded in using genetic algorithm methods to design new antennas. M. Zada et al. has also designed two dual-band antennas (one dipole one PIFA) that operates at 403 MHz and 915 MHz [32]. The design is for implantation in mouth so where muscle tissue is not very thick and the implantation depth is only around 3 mm. The research team of Topsakal [33] from Mississippi University published their studies about the electrical properties of rat skin and the compositions of skin mimicking gel, which could be an instruction for measurements.

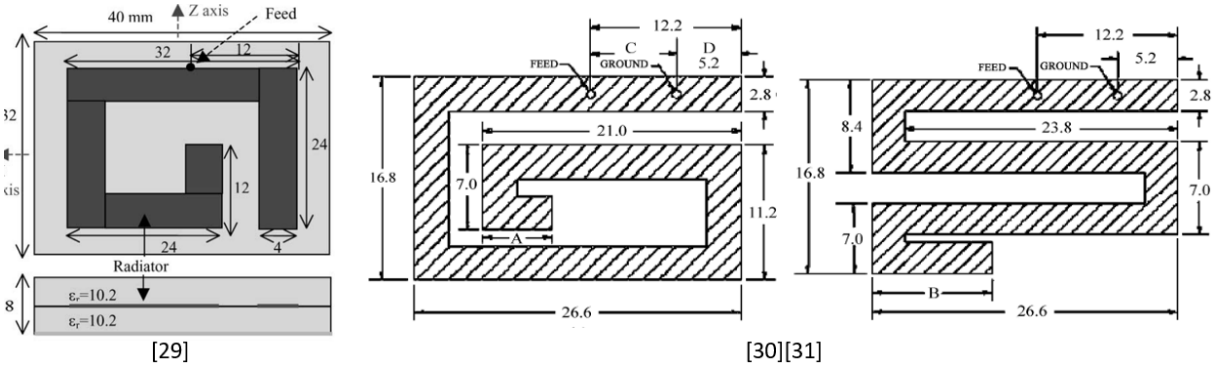

[29] [30][31]

Figure 1.4 Antenna examples from literature (ref [29-31])

There are also many other research teams who have carried out various kinds of antennas for implantation: The team of Lazzi [34-35] from North Carolina State University has done several pieces of research about the dipole kind of implantation antenna; meanwhile, the research team of Guo et al. from National University of Singapore Suzhou Research Institute proposed many examples of PIFA and slot antennas for human implantation design [36-40]. Moreover, Skrivervik et al. from Ecole Polytechnique de Lausanne [41-42], Nikita et al. from National Technical University of Athens [43], Sanchez-Fernandez et al. from University Carlos III of Madrid et al. [44] and etc. [45-49] have also done much remarkable research about the design of implantation antennas. Some representative examples of each kind of antenna are shown in Figure 1.5.

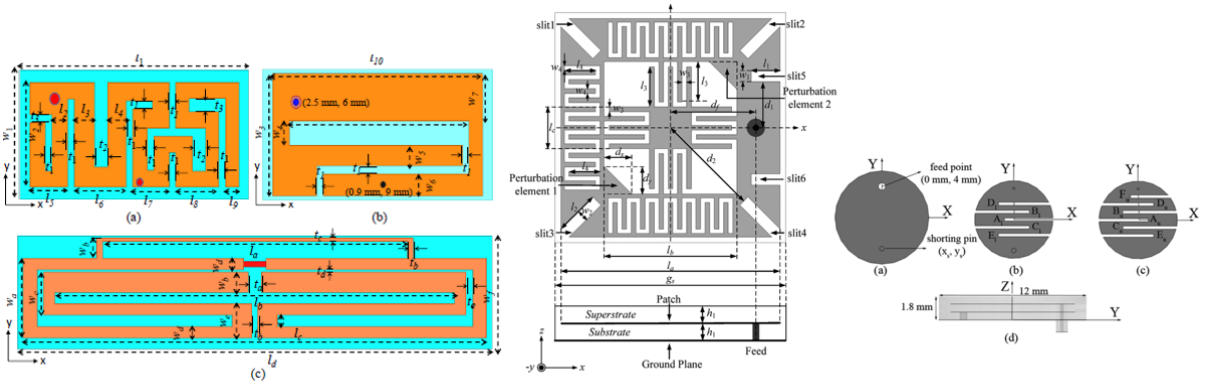

[32] [38] [43]

Figure 1.5 Antenna examples from literature (ref [35] [38] [43])

In recent years, more new approaches have appeared. In 2020, the research team of P. Anacieto from the International Iberian Nanotechnology Laboratory (INL) has proposed a self-folded micro antenna that measures only 500 x 500 x 500 μm^3 for biomedical applications. The antenna is cubic and operates at over 7 GHz [50]. Also, in 2017, the team of Stavros Koulouridis has proposed a combination of antenna and coil to enhance the power receiving efficiency [51] which is very interesting. It uses a small coil that is positioned inside the slot of an embedded antenna to enhance the power transmission link (see Figure 1.6). A. Basir *et al.* has studied another system in a capsule with four resonating frequencies for multitasking applications [52].

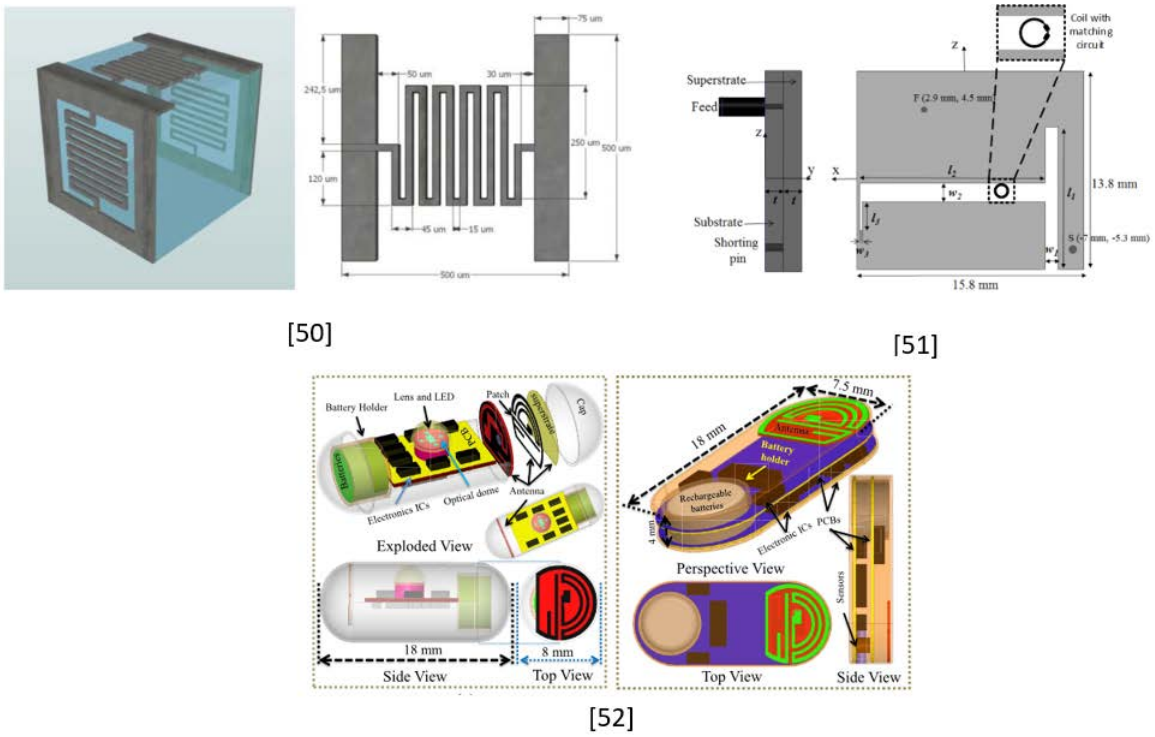

[50] [51]

[52]

Figure 1.6 Examples of creative systems in recent three years (ref [50] [51] [52])

1.2.2.1 Authorized frequency band

Before the design of the antenna, the authorized frequency band must be figured out. Table 1.1 shows the authorized frequency bands that could be used for biomedical applications.

Table 1.1 Authorized frequency bands for biomedical applications[1]

Authorized band	Frequency range
MICS (Medical Implant Communication Services) band	401 MHz – 406 MHz (core 402 MHz - 405 MHz)
WMTS (Wireless Medical Telemetry Services) band	608 MHz - 614 MHz
	1.395 GHz – 1.4 GHz
	1.427 GHz – 1.432 GHz
ISM (Industrial Scientific and Medical) band	Low frequencies [2]
	433 MHz – 434.8 MHz
	868 - 868.6 MHz
	902 MHz - 928 MHz
	2.4 GHz – 2.5 GHz
	High frequencies [3]
IR-UWB (Impulse Radio Ultrawideband)	3 GHz - 5 GHz

1 Data from Wikipedia.com
2 Including 6.765 – 6.795 MHz; 13.553 – 13.567 MHz; 26.957 – 27.283 MHz; 40.66 – 40.7 MHz
3 Including 5.725 – 5.875 GHz; 24 – 24.125 GHz; 61 – 61.25 GHz; 122 - 123 GHz; 244 - 246 GHz)

1.2.2.2 Antenna types, sizes, and operating frequencies

As discussed before, there are many interesting designs and Table 1.2 shows a comparison of their antenna type, size, operating frequencies, and corresponding tissue model.

Table 1.2 Comparison of antennas in current literature

ref	Antenna's type	Operating frequency (GHz)	Antenna size (mm^3)	Tissue model (simulation)	Tissue model (measurements)
[35]	Dipole	1.41	5.25 x 5.25 x 1.5	Eye model	Eye Phantom
[34]		2.4	5.25 x 5.25 x 4	Eye model	Eye Phantom
[54]		0.95	164 x 86	Pacemaker	Rat body
[40]	Dipole/PIFA	0.4/0.43/2.45	17 x 16.5 x 2.5	Skin cube	Skin Phantom
[29]	PIFA	0.4	40 x 32 x 8	3-layer model	None
[32]		0.4/0.9	17.25 x 8 x 0.635	Mouth model	3D head model
[43]		0.4/0.43/ 0.87/0.915	12 x 12 x 1.8	Head model	Head phantom
[38]		0.4/2.4	20 x 19.4 x 1.3	Skin cube	Skin phantom
[55]		0.4/1.4	23.6 x 19.4 x 2.4	3-layer model	None
[37]		0.4	10 x 16 x 1.27	Skin cube	Skin phantom
[31]		0.4	36 x 30 x 3	2/3 muscle	None
[39]		2.4	10 x 10 x 1.3	Skin cube	Skin phantom
[26]	Monopole	0.4/2.4	$\pi \times 16^2 \times 16$	Skin cube	Skin phantom
[27]	Spiral	0.4/2.4	$\pi \times 10^2 \times 32$	Body model	Body phantom
[44]		0.4/2.4	$\pi \times 14^2 \times 3$	Skin cube	Skin phantom
[45]	Cavity slot	2.4	4 x 7 x 10	2/3 muscle	Muscle phantom

As we can observe in the table, PIFA is the most used antenna type for this biomedical use due to its miniaturization and directivity. It is usually more directive than dipole or other kinds of antenna thanks to its ground plane.

1.2.2.3 Simulation environment

The most important factor for biomedical wireless power transmission is the biological environment. When using modeling techniques, the quality of the simulation environment determines the accuracy and usability of the system. The properties of four kinds of common human tissues (bone, muscle, fat, and skin) in the frequency bands which are dedicated to biomedical applications are presented in Table 1.3.

Table 1.3 Electrical properties of human tissue in common frequency bands [56] [57]

Tissue name	Frequency	Relative permittivity (dielectric constant)	Conductivity (S/m)
Bone	402 MHz	13.14	0.09
	433 MHz	13.07	0.09
	915 MHz	12.44	0.15
	1.4 GHz	12.05	0.21
	2.45 GHz	11.38	0.39
	4 GHz	10.53	0.73
Muscle	402 MHz	57.11	0.80
	433 MHz	56.87	0.81
	915 MHz	55.03	0.95
	1.4 GHz	54.11	1.14
	2.45 GHz	52.73	1.74
	4 GHz	50.82	3.02
Fat	402 MHz	5.58	0.04
	433 MHz	5.57	0.04
	915 MHz	5.46	0.05
	1.4 GHz	5.40	0.06
	2.45 GHz	5.28	0.10
	4 GHz	5.125	0.18
Skin	402 MHz	46.7	0.69
	433 MHz	46.1	0.70
	915 MHz	41.3	0.87
	1.4 GHz	39.7	1.04
	2.45 GHz	38.0	1.46
	4 GHz	36.6	2.34

There are many kinds of simulation environments that could represent a biological tissue: Single-layer tissue model; 2/3 muscle model; multi-layer human model and an accurate numerical human model.

The most commonly used is the single skin cube (see Table 1.2). From the previous literature comparison, many research teams have chosen this model for the simulation environment thanks to its simplicity in order to save the computation time. Nevertheless, the model is too simple to represent the human tissue as shown by the statistics in Table 1.3. Also, the skin layer is too thin for any kind of implantation and thus it is not realistic for simulations.

The multi-layer model is a more accurate model simulating the human tissue environment. The most commonly used tissues in the layers are bone, muscle, fat, skin, whose properties are shown in the Table above. The multi-layer model is able to simulate the reflection between the different layers that exist in the real application. Many research teams have already applied this model [46] and it is considered to be a good compromise between the model accuracy and the computation time. Figure 1.7 shows model that is used in [58] where first appears this three-layer 'arm' model. This model is also used in this thesis.

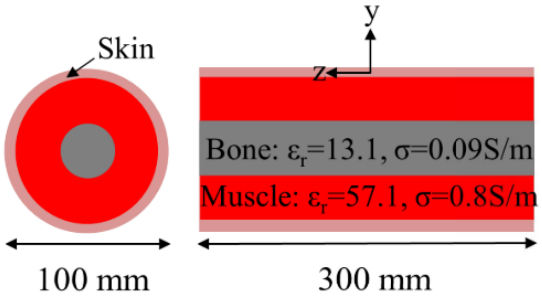

Figure 1.7 A three-layer human tissue model [58]

The 2/3 muscle model is also found in the literature. It is also a single-layer model but with a "tissue" that has special electrical properties equivalent to the multi-layer model. It is more advanced model than the single-layer skin model but not as precise as the multi-layer model. For example, a 2/3 muscle model at 402 MHz has a relative permittivity of 42.91 and conductivity of 0.65 [30]. These values are the "equivalent" electrical properties of the human body if the real human body is considered as a homogeneous tissue. However, it is not as precise as multi-layer model because it could only simulate human tissue around a certain frequency and some reflections between layers are neglected.

The most precise and accurate model is a 3D human model. This model is normally trustworthy for antenna design simulations since several existing models have been created from Magnetic Resonance Imaging (MRI) scans. CST (Computer Simulation

Technology) Studio Suite [56] has several 3D human models aged from 8 weeks to 43 years old as presented in Figure 1.8.

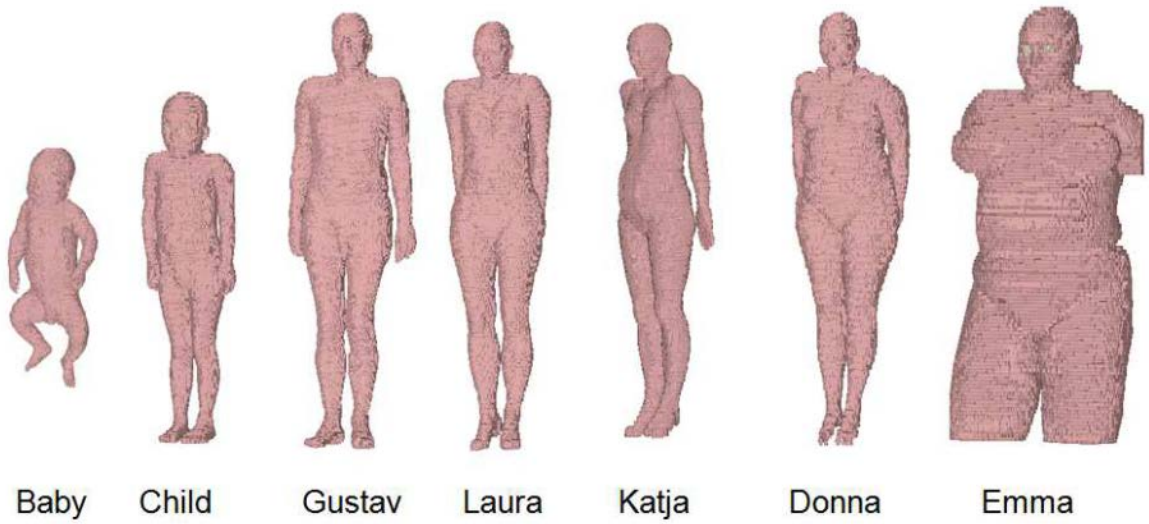

Figure 1.8 3D human models provided by CST Studio suite [59]

1.2.2.4 Experimental environment

After simulated in the simplified human tissue environment, the power transmission system must also be tested in a realistic environment to validate its design and characteristics. The testing methods could be largely subdivided into 2 groups: in-vitro and in-vivo. In-vitro is the method which is performed outside any live creature and in-vivo is done with animals.

As presented in the previous articles, above 90% of proposed systems are tested in an in-vitro environment: Phantom. Many chemical compounds are dissolved in water which makes the solution have the same electrical properties as human tissue at a fixed frequency. This solution is called phantom. For each frequency, the percentage of each component is different. Normally, for every 100 ml of the solution liquid, 1 g of agarose is also added, as the liquid is turned into gel [60]. A gel is more convenient than a liquid solution since an antenna could be easily placed inside the phantom. Table 1.4 shows the solution liquid ingredient for several commonly used frequencies.

Table 1.4 Solution ingredient for commonly used frequencies [61]

Ingredients (% by weight)	Frequency (MHz)									
	450		835		915		1 900		2450	
Tissue Type	Head	Body	Head	Body	Head	Body	Head	Body	Head	Body
Water	38.56	51.2	41.5	52.4	41.1	56	54.9	40.4	62.7	73.2
Salt (NaCl)	3.95	1.49	1 .45	1.4	1.35	0.76	0.18	0.5	0.5	0.04
Sugar	56.32	46.8	56	45	56.5	41.8	0	58	0	0
HEC	0.98	0.52	1	1	1	1.21	0	1	0	0
Bactericide	0.19	0.05	0.1	0.1	0.1	0.27	0	0.1	0	0
Triton X-100	0	0	0	0	0	0	0	0	36.8	0
DGBE	0	0	0	0	0	0	44.9	0	0	26.7
Dielectric Constant	43.42	58	42.5	56.1	42	56.8	39.9	54	39.8	52.5
Conductivity (S/m)	0.85	0.83	0.91	0.95	1	1.07	1.42	1.45	1.88	1.78

In the Table 1.4, Salt stands for 99^{+}% Pure Sodium Chloride; Sugar for 98^{+}% Pure Sucrose; Water for De-ionized water with 16 MΩ^{+} of resistivity; HEC for Hydroxyethyl Cellulose; DGBE for 99^{+}% Di(ethylene glycol)butyl ether, [2-(2-butoxyethoxy)ethanol] and Triton X-100 (ultra-pure) for Polyethylene glycol mono [4-(1,1, 3, 3-tetramethylbutyl)phenyl]ether.

Apart from phantoms, using animal meat tissue for biomedical testing is also an efficient method. As shown in Figure 1.8, some ground pork could be used for antenna testing. Comparing with phantom testing, using animal tissue is more convenient, more realistic and insensitive to any frequency changes.

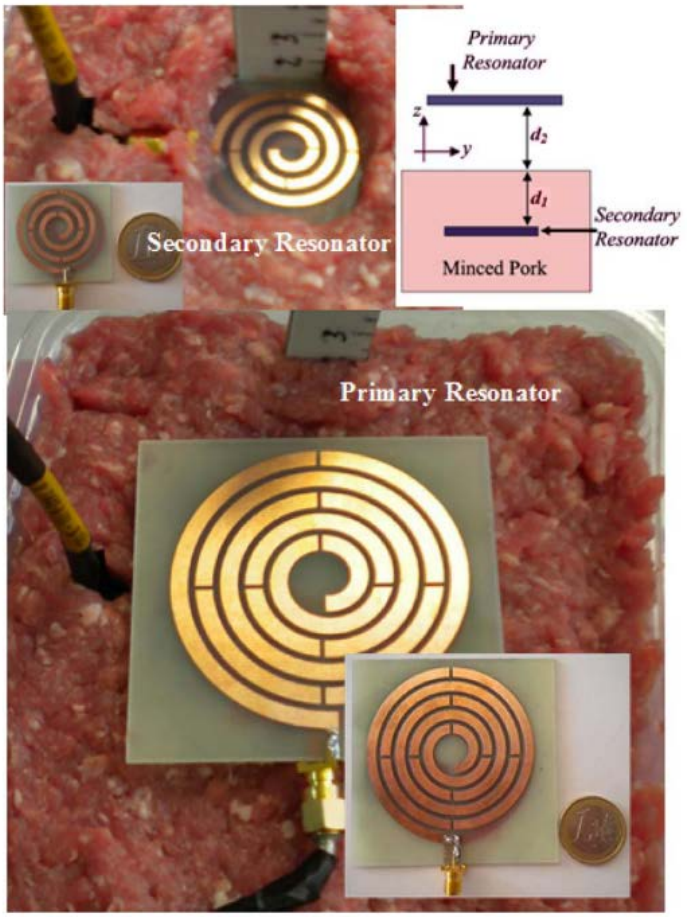

Figure 1.9 Animal tissue (minced pork) used as experimental environment material [62]

1.2.3 Rectifying circuit

A Radio Frequency (RF) medical energy transmission system normally consists of two parts: An antenna for capturing energy and a circuit for converting alternating current (AC) power to direct current (DC) power. The circuit has to match the antenna in order to achieve the best performance.

As mentioned in the previous sections, many studies have been focused on the antenna part. Meanwhile, the rectenna (rectifier-antenna) system has been also widely studied in the world: For example, in [63], an equivalent global circuit simulation of a rectenna was proposed by H. W. Cheng et al. They have studied a rectenna system that operates at 405 MHz with an identical circuit input power of 10 dBm and rectifying efficiency of 76%. Figure 1.10 shows the structure of the rectenna. The rectifying circuit is a half-wave rectifier that only reserves half of the power. However, in reality, in such systems, available power is of the order of -20 dBm. Indeed, most of the researchers focus on such power levels. For example, B. J. DeLong et al. propose a rectenna structure that operates at 2.4 GHz in free space, but the efficiency at -20 dBm is only around 7% [64]. Also, C. Liu et al. have worked on a rectenna system that only has an

efficiency of 20% with an input power of -20 dBm and implantation depth of 4 mm which is implanted in the body [65].

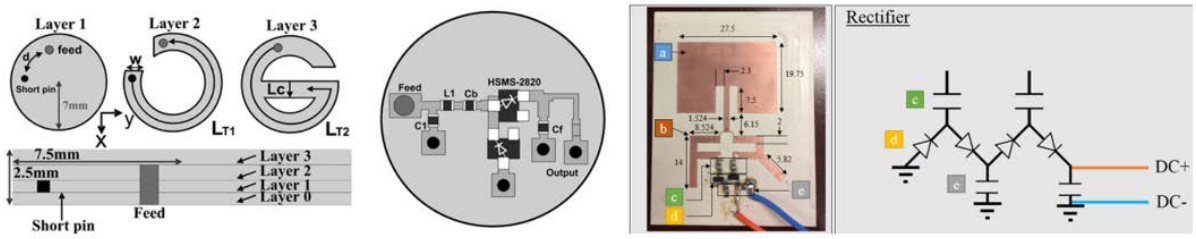

[60] [61]

Figure 1.10 Rectenna examples in literature [63] [64]

It is expected that an implanted rectenna system is efficient at low power levels. In [66], a free space compact rectenna system for ambient energy harvesting is proposed, but the introduced system is not dedicated to biomedical applications. As for implanted rectenna systems, D. Vasisht et al. have studied the back-scattering method for communication and localization, in which signal reflection, attenuation, phase change, and refraction are discussed [67]. X. Fang et al. proposed a system working at Ultra High Band (UHB, 3.1- 5.1 GHz). However, at this frequency region, losses could be very high during the power transmission step even with a small implantation depth (-42 dB at 18 mm) [68]. Recent wireless power transfer rectenna systems have been investigated at 2.45 GHz or various other frequencies in the GHz range but with a total footprint larger than 5 cm^2.

In conclusion, due to its high operating frequencies and low input power level, the design of a miniaturized deep-implanted and efficient energy transmitting rectenna remains a challenge for researchers.

1.3 Thesis objective

In order to decide the thesis objective, it is necessary to figure out the weak point of each design and improvement approaches.

Firstly, for most of the designs, antennas have still big sizes [25-33], which will add a great challenge for the patients as well as the surgeons. A big-size implanted antenna may hamper the patient's movement and also cause unnecessary damage. There are some antennas, small enough for implantation, but they operate at high frequencies [34] [38] [39]. High frequencies cause higher loss, which may saturate the SAR (see chapter 2) with only a little power delivered. Secondly, many antenna designs do not have a suitable rectifying circuit [34-49]. RF power could not be used directly by any sensor and an unmatched rectifying circuit may strongly attenuate the power transmission efficiency. Even for designs that have their own rectifying circuits [60-65], the circuits are not simulated and tested with a real input power level, which may lead to a completely

different result. Thirdly, the simulation environment for many works is a skin box which is not realistic enough (see Table 1.2). This environmental difference may cause significant resonant frequency shifting and the transmission efficiency would be seriously reduced at a non-resonant frequency. Some of the researches discussed implants in the skin layer which is also not feasible due to the skin thickness. Finally, for their measurements, most of them use human tissue phantom. Phantom is convenient but could only simulate the human tissue at a fixed frequency. During measurements, it is very likely that fabricated antennas do not resonate at preset frequencies with slight shifting. With this phenomenon, the phantom is not a suitable choice for measurement.

Based on the previous discussions, the objective of the thesis becomes clear. First of all, the antenna together with the rectifying circuit must occupy little space without losing much efficiency. A convenient choice of operating frequencies and antenna's shape is quite necessary. Then, a matched rectifying circuit has to be designed, simulated, and tested together with the antenna. A completely designed system could minimize the mismatch loss and optimize the power received by the load. After that, a realistic simulation environment must be constructed to avoid inaccuracy in designs. In addition, an adequate simulation model should be defined by using the optimum amount of computation and without compromising the precision of the computation. Last but not least, the measurement has to be done under a more realistic biological environment than the phantom.

In conclusion, in order to construct such an efficient wireless power transmission system, the following criteria must be fulfilled:

- Small size but with high transmission efficiency
- Antenna and rectifying circuit need to be both designed and matched with respect of all necessary safety (and other) constraints
- System tested in a realistic environment

1.4 Conclusion

This chapter presents the current development of wireless power transmission technology. Many methods have been used by researchers and three of them are based on the standard electromagnetic theories: Inductive charging, strongly coupled magnetic resonance and microwave power transfer. Generally, these three methods are different because of their operation distance. Microwave power transfer has been finally chosen for this thesis due to its advantages of implant miniaturization and positioning robustness (comparing to the other two methods) while charging. Several important aspects of recent studies about this method were introduced and compared, such as: Implanted antenna's type, size, operating frequency band, simulation and

experimental environment, and rectifying circuit. Finally, the disadvantages of these studies are concluded and analyzed.

The state-of-art chapter is very important since it gives us the direction in which the thesis should be directed.

Chapter 2

Antenna design and simulation

2.1 Introduction

In this chapter, a miniaturized deep in-body implanted circular antenna is presented. The design process of the antenna will be carefully studied and presented. The global transmission scenario is presented in Figure 2.1.

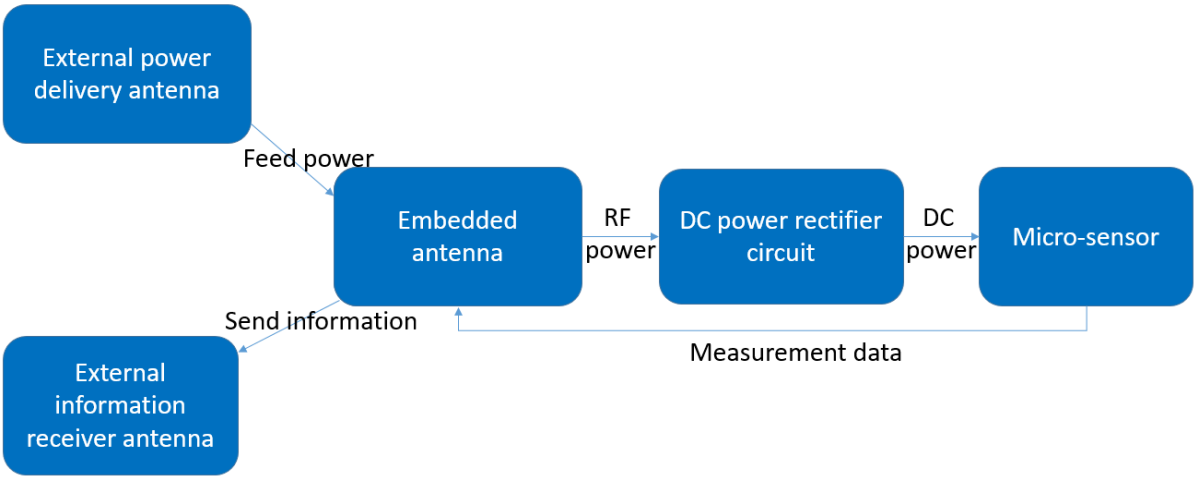

Figure 2.1 Simplified wireless power system operation

An external power delivery antenna emits power. The embedded antenna receives this power and converts this Radio-Frequency (RF) power into Direct-Current (DC) power. This DC power is used directly to feed the pre-implanted micro-sensor. In a real scenario, the sensor returns the measurement results and the embedded antenna sends the information to a received outside the body.

Since the embedded antenna is responsible for two functions: power transfer and data transmission, the design of a dual-band antenna that could support both wireless power transmission and wireless information communication is thus necessary.

2.1.1 Frequency range

Since the antenna is dedicated to biomedical applications, according to the international regulations, several frequency bands are authorized, for example:

- Medical Device Radiocommunication (MedRadio) Service band: 401-406 MHz
- Industrial, Scientific, and Medical (ISM) bands: 433.1-434.8 MHz, 868-868.6 MHz, 902.8-928 MHz, and 2.4-2.5 GHz
- Wireless Medical Telemetry Services (WMTS) band: 1395-1400 MHz
- Impulse Radio Ultrawideband (IR-UWB) band: 3-5 GHz

All frequency bands have their own advantages and disadvantages: For lower frequency bands, the wavelength is longer and thus a shorter period of the signal propagates inside the tissue. The loss is therefore low for the same thickness of lossy

tissue than higher frequencies (see formula 2-6). However, if the wavelength is long, the antenna physical size will also be bigger which is not convenient for implantation.

In order to minimize all the disadvantages and find a compromise, the 401-406 MHz MedRadio band and 902.8-928 MHz ISM band are chosen for the operation band of the antenna. Also, the authorized bandwidths are relatively large which may also simplify the antenna design and increase the robustness of the system since it is much easier to fit in the standard.

Furthermore, for the two chosen frequency bands, there are two existing regulations [69] [70] which indicate that at 401-406 MHz band (bandwidth 6 MHz), the maximum authorized emission power is -16 dBm while for 902.8-928 MHz (bandwidth 25.2 MHz) is 30 dBm respectively. Therefore, the 902.8-928 MHz band is chosen for the power transmission. This will be explained in detail in the next chapter.

For the design, the CST Studio Suite software is used [56]. CST Studio Suite is a multi-domain, high-performance 3D Electromagnetic analysis software for designing, analyzing, and optimizing electromagnetic (EM) components and systems utilizing finite-element modeling method. It is own by the Dassault Systems Company. The computation and designs presented in this chapter are all supported by CST Microwave Studio Suite, version 2017.

In the following section, we discuss the antenna design and simulation results.

2.2 Antenna Design

2.2.1 Preliminary design

A precise parametric model of the antenna is shown in Figure 2.3. It is made up of a ground plane, a patch, a substrate between them, a superstrate over the patch, and a coaxial feeding. The substrate and superstrate are made from the same material: Rogers RO 3210 (ε_r = 10.2, tanδ = 0.003). Both the patch and the ground plane are circular, connected with a ground wire (located at point W, diameter 0.3 mm) which helps to decrease the antenna size. Two circular slots are also cut from the patch in order to have two operating frequencies at 403 MHz and 915 MHz. The coaxial cable (located at point F) is standardized to 50 Ω impedance. All the parameters marked in Figure 2.2 are presented in Table 2.1.

The reason why we chose the Rogers RO3210 as the antenna's substrate is as following:

- It has high permittivity which could help the miniaturization of the antenna
- It has similar permittivity with another bio-friendly material, Alumina (

ε_r = 9.9). However, Alumina is expensive and difficult to manufacture. The Rogers RO3210 is cheaper and more accessible for scientific research.

The antenna has a circular shape to avoid sharp edges. Table II presents the comparison results between the circular PIFAs that are designed in previous publications and the antenna designed in this paper, which is smaller, embedded deeper, and resonating at lower frequencies to reduce losses.

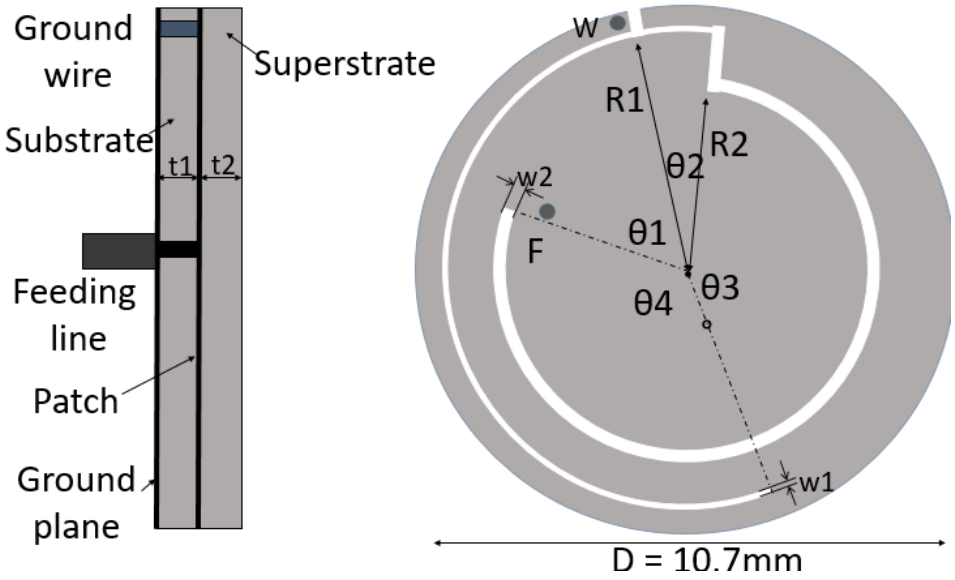

Figure 2.2 Geometry of the developed circular antenna

Table 2.1 Antenna Parameters

Parameter Name	Value (mm)	Parameter Name	Value (deg)
R1	4.9	*θ1*	70
R2	3.76	*θ2*	18
w1	0.15	*θ3*	163
w2	0.32	*θ4*	109
t1	0.64		
t2	0.64		
D	10.7		

2.2.2 Design parameters effect on the antenna performance

The antenna has two resonant frequencies at 403 MHz and 915 MHz that correspond to data and power transmission respectively. For this antenna design, the following parameters are vital for determining the antenna's resonant frequencies and these

parameters are discussed below (it is worth pointing out that all the comments here are only suitable for the antenna in this thesis, it does not represent other ones):

- *R1* and the first arc's angle (*θ1*+ *θ2*+ *θ4*) determine the placement of the first resonant frequency at 403 MHz. As we increase the length of the first arc, the antenna resonates at a lower frequency than 403 MHz since the 'resonating arm' becomes longer.
- *w1* affects the real part of the antenna's impedance at the first resonant frequency. The resistance of the antenna at 403 MHz decreases as *w1* decreases. However, due to the fabrication limit, w1 is restricted to be higher than 0.15 mm.
- *t1* and *t2* affect the impedance of the antenna at both frequencies. A thicker substrate may cause an increase of the antenna's resistance at 403 MHz. However, since the Rogers company provides only the 0.64 mm thickness, the value 0.64 is used in simulations.
- *R2*, *w2*, and the inner arc's angle (*θ3*+ *θ4)* affect the second resonant frequency in the same way as *R1* and *w1*.
- The feeding point *F* affects the length of the current circulating on the radiating patch thus affects the antenna's impedance at both resonant frequencies. The longer the current path, the higher the resistance.
- The via at *W* allows the appearance of the double resonant frequencies of the antenna.

2.2.3 Simulation environment

2.2.3.1 Propagation in tissue

Human tissue is an inhomogeneous material that contains many kinds of biological elements, such as: Bone, muscle, fat, skin, blood, and also some various organic materials. Among those elements, bone, muscle, fat, and skin are the most common and take the most volume percentage. Among those four kinds of tissue, bone and fat contain much less water than muscle and skin, and thus have less loss due to less free charge electron which could respond to an alternating electromagnetic (EM) field. The distribution of the time-harmonic EM field is mainly determined by its complex permittivity ε:

$$\varepsilon = \varepsilon_0 \varepsilon_r \tag{2-1}$$

where ε_0 is the permittivity of the vacuum and ε_r is the complex relative permittivity, which could be defined as:

$$\varepsilon_r = \varepsilon_r' - j\varepsilon_r'' \tag{2-2}$$

where ε'_r is the real part of the permittivity and ε''_r the imaginary part with loss tangent's definition:

$$tan\theta = \frac{\varepsilon_r''}{\varepsilon_r'} \tag{2-3}$$

and

$$\varepsilon_r'' = 2\pi f \frac{\sigma}{\varepsilon_0} \tag{2-4}$$

where σ is the conductivity of the material and f the frequency. Thus the complex relative permittivity could be expressed as:

$$\varepsilon = \varepsilon_0 \varepsilon_r' - 2\pi j f \sigma = 2\pi f \sigma \cdot (\frac{1}{\tan\theta} - j) \tag{2-5}$$

There is another important definition called skin depth δ, which is defined as the depth for which the magnitude of the electromagnetic wave is attenuated with a ratio of 1/e:

$$\delta = \frac{1}{2\pi f \sqrt{\frac{\mu\varepsilon_{real}}{2} \cdot \left(\sqrt{1+\frac{\sigma^2}{4\cdot\varepsilon^2\pi^2 f^2}} - 1\right)}}$$

$$= \frac{1}{\sqrt{\mu\pi f \cdot \left(\sqrt{16\pi^4 f^4 \sigma^2 \cdot \left(\frac{1}{\tan\theta} - j\right)^2 + \sigma^2} - 4\pi^2 f^2 \sigma (\frac{1}{\tan\theta} - j)\right)}} \tag{2-6}$$

where μ is the permeability of the tissue.

Main losses normally exist in muscle and/or skin since such media have a higher conductivity than the fat or bone. For example, at 402 MHz and at a distance of 10 cm EM power is attenuated by 29% in fat while in muscle is attenuated by 89% [71].

Also, in order to decrease the losses in the tissue, the implantation depth needs to be much smaller than the skin depth, which requires a low frequency. By considering the high gain and small size for high-frequency antennas, a compromise should be made and 902.8 MHz to 928 MHz ISM band is temporarily chosen for the power transmission, more details about the power transmission band choice issues are discussed in the next chapter 3.

2.2.3.2 Single tissue (muscle) box

There are different simulation environments that are currently used by researchers, for example: Skin box, muscle box, three-layer model or even anatomic head model [43]. Among all the human tissue, muscle is the lossiest one (see Table 2.2).

Table 2.2 Dielectric constants of human tissue [56]

Frequency		Bone	Muscle	Skin
403 MHz	ε_r	13.22	57.15	46.81
	σ (S/m)	0.09	0.79	0.69
915 MHz	ε_r	12.45	54.98	41.35
	σ (S/m)	0.15	0.93	0.85

In order to investigate the impact of tissues' properties on EM losses, a simple electromagnetic problem is modeled. A box of muscle and a simple dipole are considered, as shown in Figure 2.3.

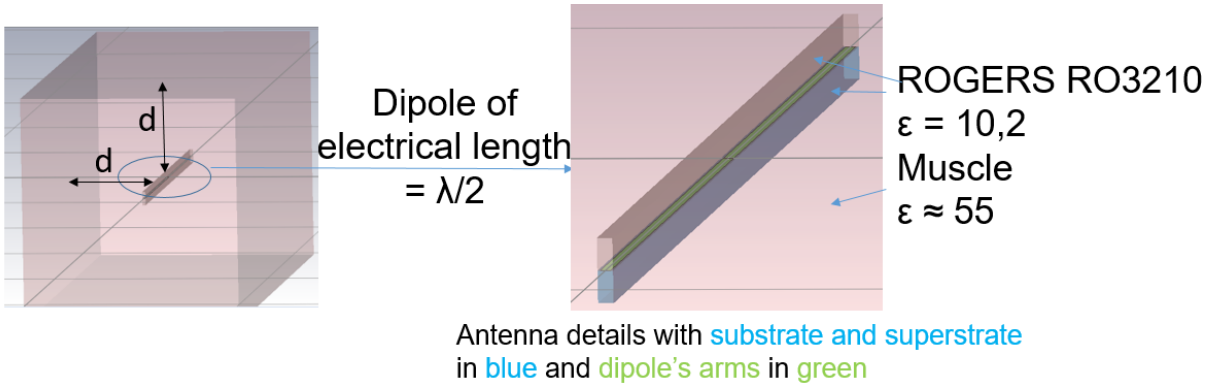

Figure 2.3 Model with muscle box environment

The analysis is performed for a frequency range from 400 MHz to 1.5 GHz, and since the dipole radiates from the direction which is perpendicular to the box surface, the muscle's thickness around the dipole arm is set to d (from 15 mm to 40 mm). For each thickness d, a corresponding frequency is found for which the radiated power outside the muscle box is maximized. Results are shown in Figure 2.4. Obviously, for different antenna types and sizes, the results might vary, but this could still serve as a reference for the choice of the power transmission frequency band.

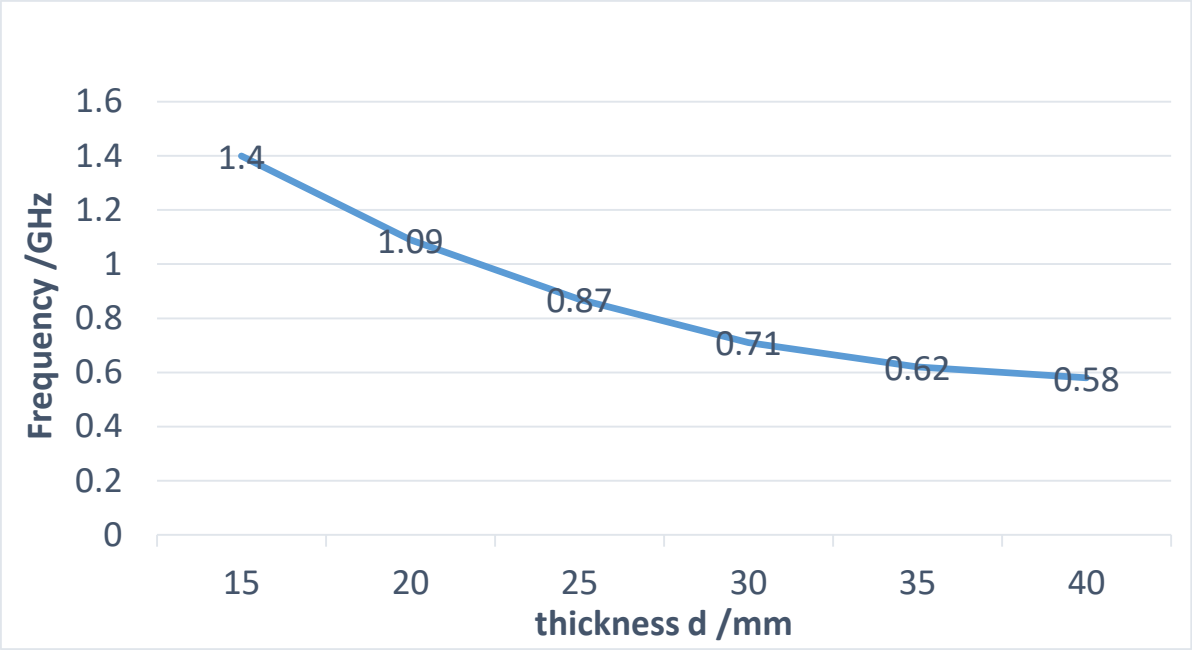

Figure 2.4 The most optimized frequency for the muscle box model with different muscle

As in the real case, it is very likely that the embedded antenna be implanted no more than 20 mm deep in muscle due to the high loss and surgical problems, which validates also the choice of the 902.8-928 MHz band for the power transmission frequency. However, if, for any reason, the implantation depth is deeper than 30 or 35 mm, a lower frequency should be applied.

2.2.3.3 Three-layer model

In order to find a compromise between the computational accuracy complexity and the representativeness of the environment, in this work, a three-layer model is chosen. The three layers are the most common tissues of the human body: bone, muscle, and skin. As fat has much less conductivity than muscle or skin and is less lossy, it is neglected in the purpose of model simplification. The radius of each layer is: Bone (25 mm), muscle (25 mm-47.5 mm), and skin (47.5 mm-50 mm). The implantation depth is calculated as the distance between the center of the radiating patch and the external surface of the skin layer. The length of the "arm" is set to the minimum value to ensure proper consideration of a "realistic" case and avoid heavy calculations. The details of the environmental model and the dielectric properties of the three kinds of human tissue are given in Figure 2.5 and Table 2.2. The contents in Table 2.2 are extracted from the CST database.

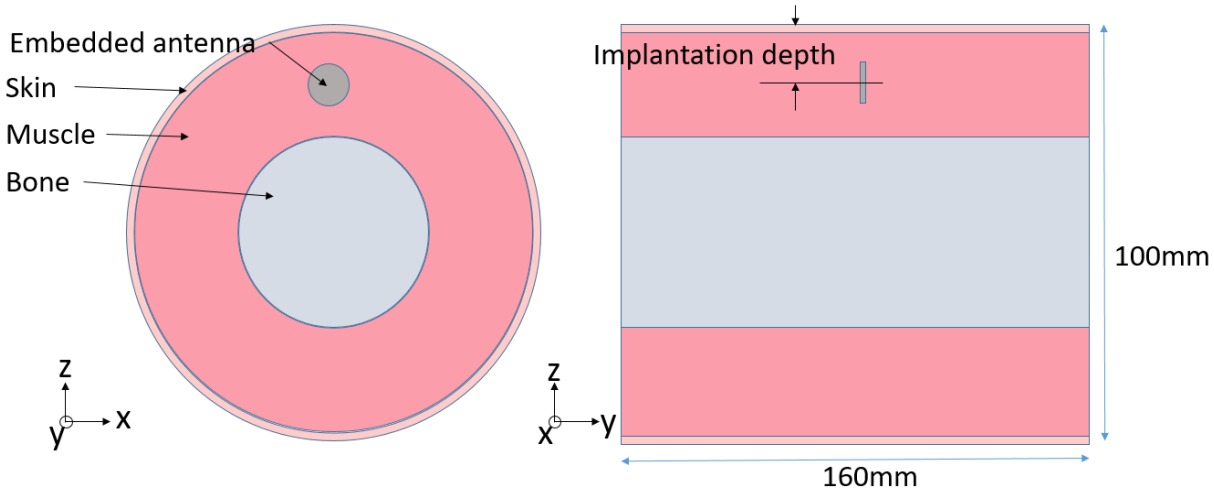

Figure 2.5 Geometry of the implantation environment

2.2.4 Advanced design

Unlike the ideal simulation environment, the experimental real case is more complex and more difficult to control. Thanks to the experimental validation that will be described later in the document, a second design of the antenna is proposed with some slight modifications.

In the simulation, the metallic radiating patch has the same size as the substrate, which leads to direct contact with the biological tissue. Due to this contact, the resistance (the real part of the impedance) of the antenna at its first resonant frequency (403 MHz) is smaller and the reactance (the imaginary part of the impedance) of the second resonant frequency (915 MHz) is larger than without contact.

However, in the real case, some glue is used so as to stick the superstrate with the substrate. During the first measurement, since the edge of the metallic patch is thin, some glue covered it and hence isolated it from the surrounding biological tissue, which avoided the contact mentioned before and thus led to shifting of the resonant frequencies (this will be proved in Chapter 5). This simulation model is presented in Figure 2.6.

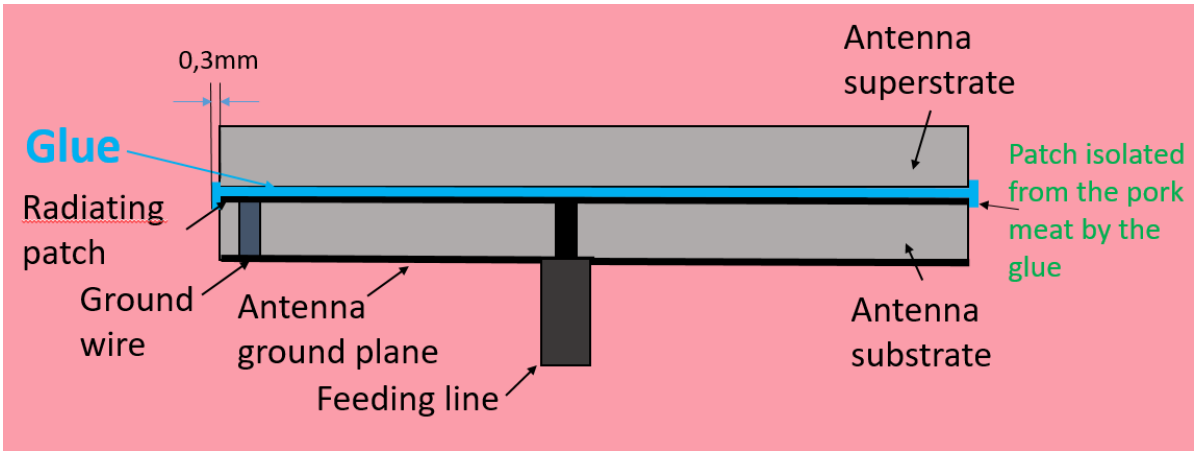

Figure 2.6 Representing schema for experimentation

As seen in Figure 2.6, the concept of making the radiating patch have the same size as the substrate is not practical. Even though the two resonant frequencies are well-positioned and impedances are well-matched, the contact between the lossy tissue with the metallic patch must be ensured in the real case in order to have good performance. Furthermore, this contact may also decrease the radiation efficiency. Therefore, an advanced design is proposed here in Figure 2.7 with all necessary values in Table 2.3.

Table 2.3 Advanced antenna parameters

Parameter Name	Value (mm)	Parameter Name	Value (deg)
R1	4.82	θ1	22
R2	3.7	θ2	18
w1	0.15	θ3	141
w2	0.32	θ4	179
t1	0.64		
Dpatch	10.8		
Dground	11		

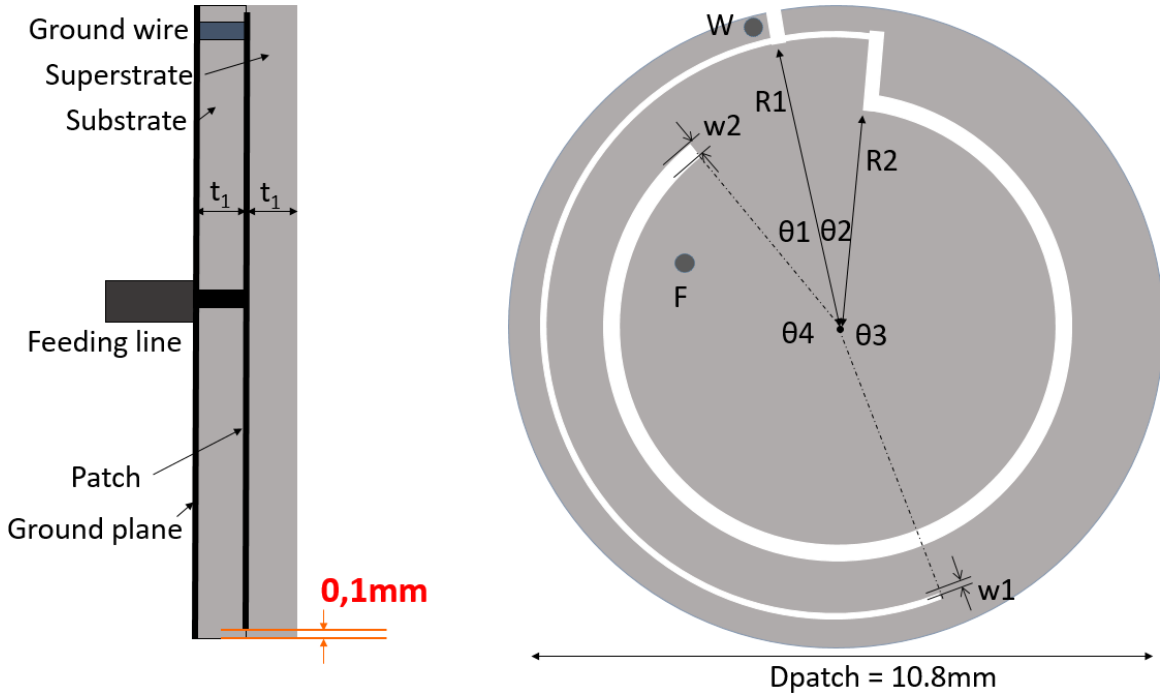

Figure 2.7 Advanced design of the antenna

As presented in the previous Figure 2.7 and Table 2.3, the substrate together with the superstrate has increased slightly their diameters by 0.1 mm in order to prevent contact between the metallic patch and the surrounding human tissue. The design is also slightly adjusted to ensure the accuracy of the new antenna's resonant frequencies.

2.3 Numerical results

All the numerical results in this chapter are obtained with CST Microwave Studio software [56]. CST Microwave Studio Software is a multi-physic simulation platform that supports electromagnetic modeling and simulation in Radio Frequency. In this chapter, all calculations are achieved with a frequency domain analysis and based on tetrahedral mesh.

2.3.1 Reflection coefficient and impedance

The Scattering matrix simply characterizes how RF power flows through a multi-port network. For example, for a two-port system presented in Figure 2.8, the S-parameter matrix can be defined as following Figure 2.9, where:

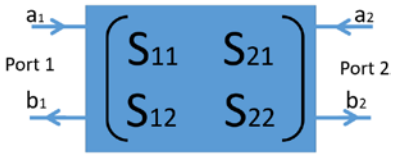

Figure 2.8 Two-port system

$$\begin{bmatrix} b_1 \\ b_2 \end{bmatrix} = \begin{bmatrix} S_{11} & S_{21} \\ S_{12} & S_{22} \end{bmatrix} \begin{bmatrix} a_1 \\ a_2 \end{bmatrix}$$

Figure 2.9 Two-port S-parameter matrix definition

Considering that port 2 has the same impedance as port 1, the corresponding S parameters are defined as:

$$S_{ij} = \frac{b_i}{a_j} \ , \forall i, j \in \{1,2\} \tag{2-7}$$

The reflection coefficient S_{11} is a key factor to characterize the resonant frequency of an antenna. It represents the ratio between the incident signal and the reflected signal. Lower the S_{11} value, higher power is radiated instead of being reflected. Figure 2.10 characterizes the reflection coefficient (S_{11}) of the proposed antenna when implanted into the three-layer arm model at the depth from 10 mm to 16 mm at 403 MHz and 915 MHz. As seen, the designed antenna is not sensitive to implantation depths. The -10 dB bandwidth at 403 MHz and 915 MHz are 80 MHz and 60 MHz, which covers the entire corresponding authorized band.

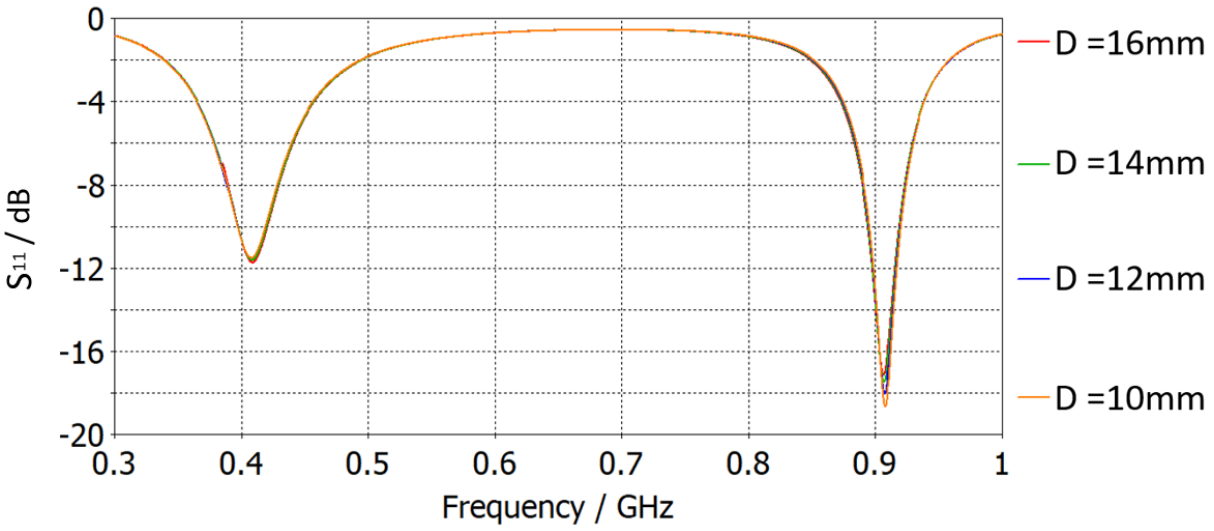

Figure 2.10 Reflection Coefficient (S_{11}) of the antenna (advanced design)

In Figure 2.11 and Figure 2.12, the real part (resistance) and the imaginary part (reactance) of the two different versions of the antenna are presented. Since the antenna's S_{11} is almost immune to implantation depth changes, only the case when implantation depth = 10 mm is presented. It shows clearly that the reactance becomes null at 403 MHz and 915 MHz, where are located the two resonant frequencies.

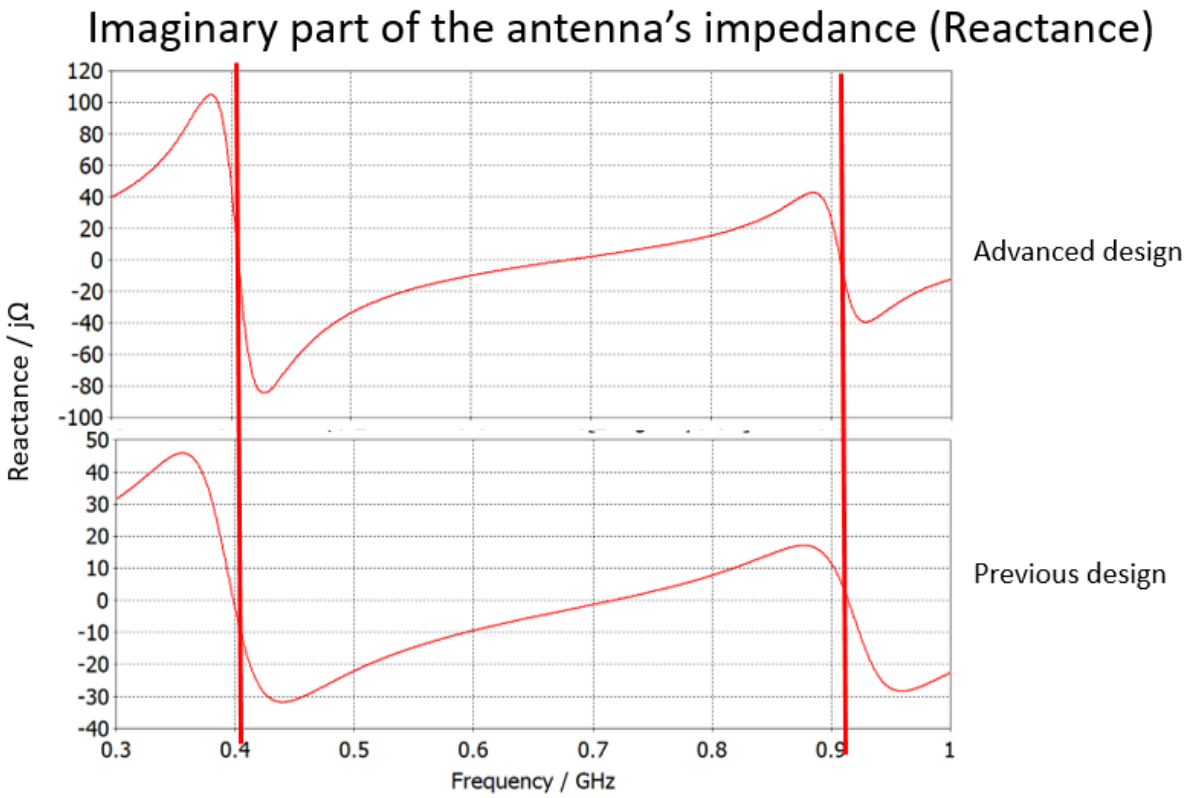

Figure 2.11 Reactance of the two designs of the antenna

However, it is easy to observe that the impedance of the antenna increases significantly when the antenna is isolated from the surrounding human tissue by the substrate and superstrate. The resistance of the antenna has increased from 80 Ω to 190 Ω at the 403 MHz band and from 50 Ω to 80 Ω at the 915 MHz band. Therefore, the port impedance should also be increased to 110 Ω in order to match the new design. The value of the port impedance is chosen closer to the resistance at the power transmission band (915 MHz) for reasons that will be explained in Chapter 3.

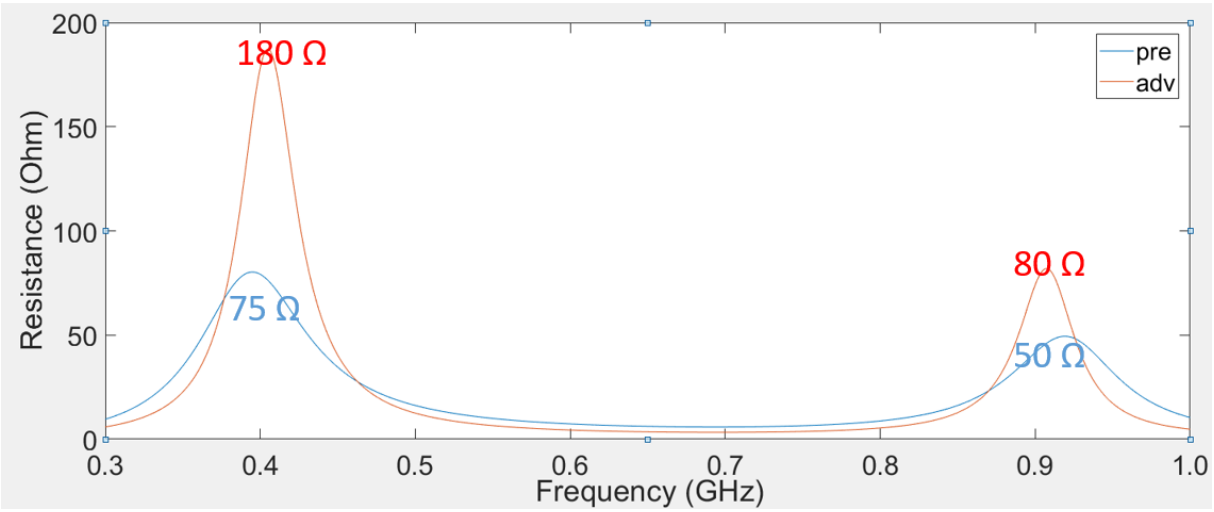

Figure 2.12 Resistance of the two designs of the antenna

2.3.2 Radiation pattern and efficiency

The radiation pattern describes the radiation of antenna and indicates the direction of the main lobe at far-field range. This helps to identify the direction in which it could receive more power and adjust the design. The radiation pattern is calculated in the center of the frequency band: 403 MHz and 915 MHz. Since the "human arm model" (the three-layer cylinder) is positioned along the Y-axis, the 2-D radiation patterns in xz plane for the first design are presented in Figure 2.13.

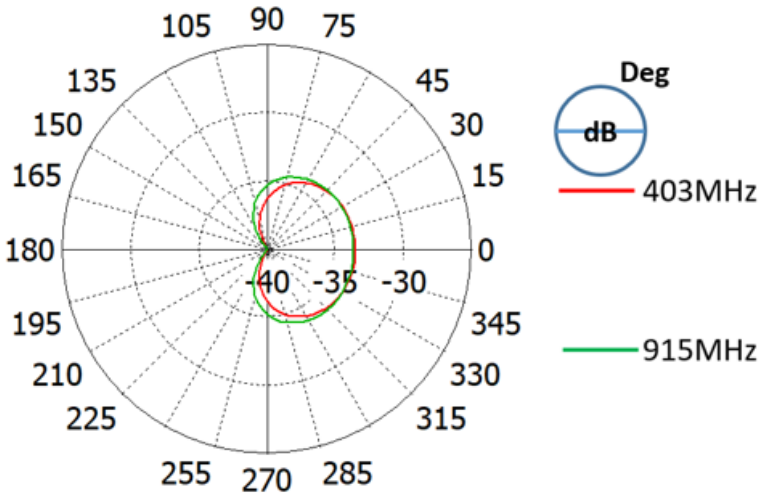

Figure 2.13 2D radiation pattern of the antenna at 10 mm implantation depth for the old design

The antenna is implanted with 10 mm depth. At MedRadio band (403 MHz), the maximum gain in far-field is around -33.5 dBi and towards Z-axis (see Figure 2.7 for axis positioning). At the ISM band (915 MHz), the maximum gain is -33.65 dBi. It is worth pointing out that the antenna has better maximum gain at a deeper location: At 16 mm depth, its maximum gain increases to -31.6 dBi at 403 MHz and -33.1 dBi at 915 MHz since the radiation pattern has a narrower main lobe.

For the advanced design, the radiation pattern at 10 mm implantation depth is shown in Figure 2.14. For the purpose to compare the radiation pattern between figure 2.13 and figure 2.14.,they are already in the same scale.

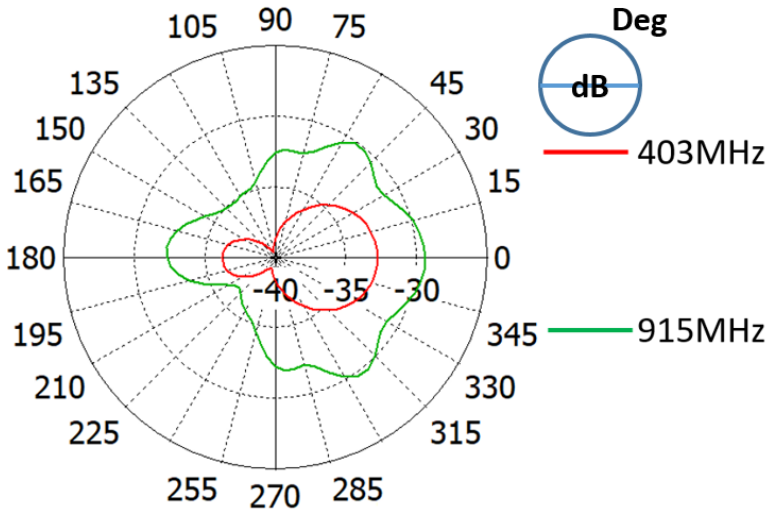

Figure 2.14 2D radiation pattern of the antenna at 10 mm implantation depth for the new design

As seen in Figure 2.14, the new design antenna still has the main lobe facing the same direction. However, the maximum gain of the antenna at 915 MHz has increased from -33.65 dBi to -29.45 dBi, which is around 2.5 times stronger. This validates the idea that avoiding the human body-antenna contact could enhance the radiation efficiency of the antenna at the 915 MHz band, which will be determined as the power transmission band. It is worth mentioning that the radiation pattern is more 'disturbed' here for the new design. This is because the new design has a coaxial arm that simulates the coaxial cable. The coaxial arm was not included in the first design. At the information exchange band (403 MHz), the efficiency is -32.8 dBi. This is acceptable since the signal is still receivable.

2.3.3 Specific Absorption Rate (SAR)

Specific Absorption Rate (SAR) is a vital parameter that indicates the safety level of an embedded antenna, it represents the average amount of electromagnetic power that is absorbed by per unit mass of the human body when exposed to an electromagnetic field. The SAR value for a certain biological tissue is defined as the following formula:

$$\mathrm{SAR} = \frac{1}{V}\int_{sample} \frac{\sigma|E|^2}{2\rho} \quad [W/kg] \tag{2-8}$$

where

- V is the volume of the analyzed sample
- E is the RMS value of the electric field
- σ is the electrical conductivity
- ρ is the mass density

The two IEEE standards about SAR limits [72] [73] refer to the value of SAR averaged every 1 g or 10 g of human body.

- In the United States, the Federal Communication Commission (FCC) stipulates that for every 1 gram of human tissue, the maximum SAR value must not exceed 1.6 W/kg.
- In the European Union, the European Committee for Electrotechnical Standardization (CEN-ELEC) stipulates that for every 10 g of human tissue, the maximum SAR must not exceed 2 W/kg.

Usually, the FCC rules are stricter than the CEN-ELEC regulations.

Considering a one-port system of the antenna, in order not to exceed the SAR limits, the maximum power feed into the antenna should be limited. In Table 2.4, the maximum input power for the antenna that satisfies each SAR limit at 403 MHz and 915 MHz for implantation depths of 10 or 16 mm are given.

Table 2.4 Maximum input power for antenna

Max input power	**1 g-average**		**10 g-average**	
Implantation depth (mm)	**10 mm**	**16 mm**	**10 mm**	**16 mm**
403 MHz	15.38 mW	14.99 mW	72.22 mW	71.17 mW
915 MHZ	14.08 mW	14.01 mW	86.33 mW	91.19 mW

As seen in the table, the FCC regulation is truly stricter in this case than the other one. Therefore, when the antenna operates as a receiver device, the SAR safety regulation could be easily met, since either emitting or receiving 14 mW is a hard task.

2.3.4 Surface current and polarization

The surface current density is also an important factor, especially during the antenna's design. It shows the polarization mode of the antenna and the current path on the patch. This helps to adjust the antenna in order to resonate at the right frequency range or even to create another resonant frequency. Figure 2.15 shows the surface current density distribution on the radiating patch at 402 MHz and 915 MHz.

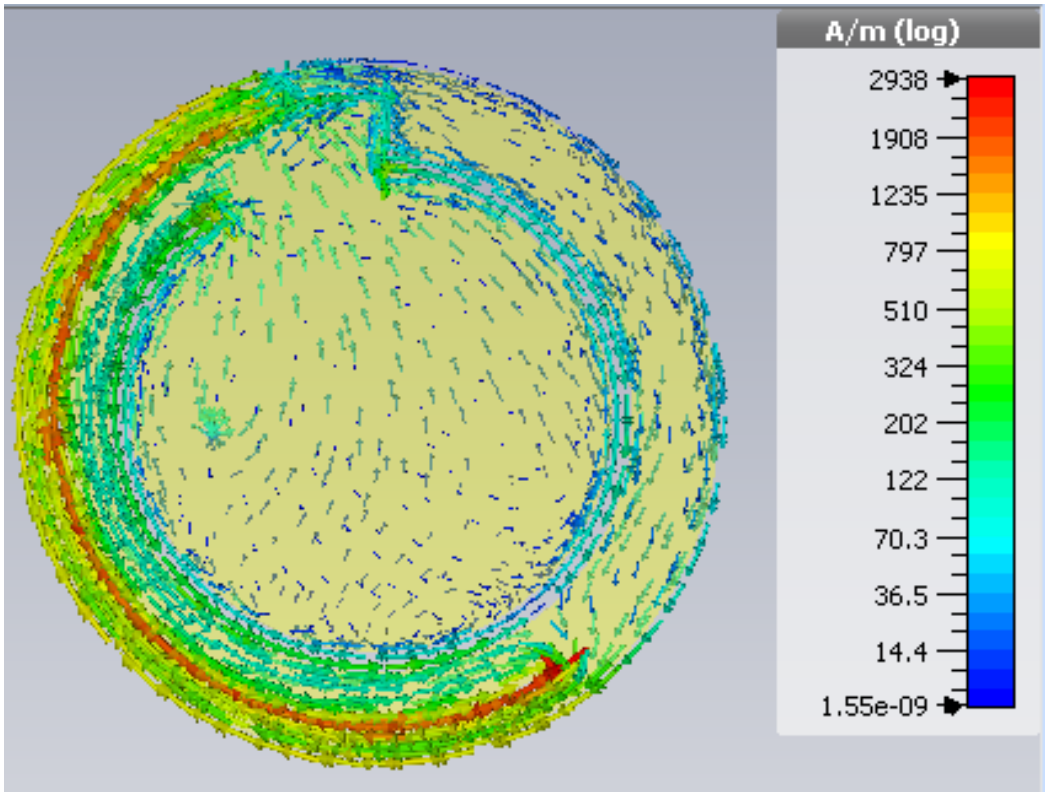

[a]

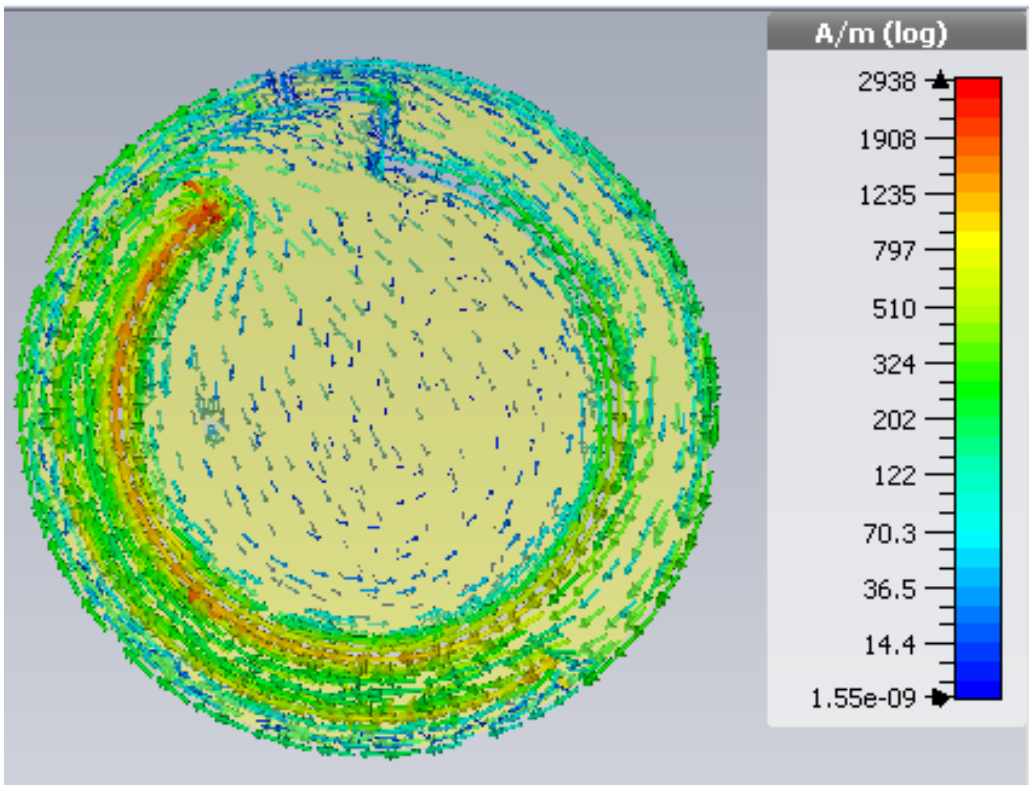

[b]

Figure 2.15 Surface current density on the radiating patch at around phase = 250°([a] at 402 MHz and [b] at 915 MHz)

As seen, the current along the external slot reaches its peak value when the antenna resonates at 402 MHz and the current along the internal slot reaches its peak at 915 MHz. This shows the radiation and the polarization mode of the antenna. As the current always flows along with the slots, the antenna is linearly polarized.

2.4 CST configuration

Some necessary CST configurations are presented in this section.

2.4.1 Before simulation

First of all, a new project of the "Bio-Medical device-MRI" should be created. Then the prototype of the antenna including antenna, substrate, superstrate, and ground plane. Also, a tri-layer cylinder represents the human arm as a simulation environment. Followings are some suggestions on the special configurations for this simulation:

- In the **simulation-frequency** panel, the frequency range should be set appropriately because the mesh depends on this frequency range and may lead to different results. An example is shown in Figure 2.16

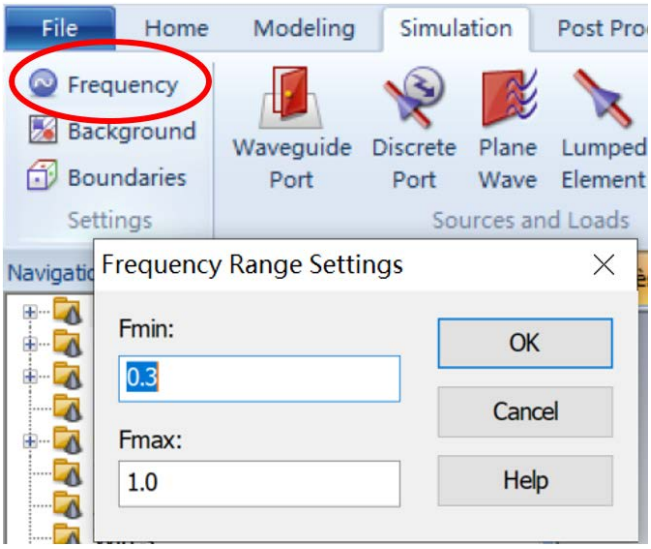

Figure 2.16 Frequency setting in CST

- **Background** should be set to the environmental material.
- **Boundaries** are the boundary condition of this calculation field established by the Finite-element method so it must be set properly. There are six kinds of boundary conditions and each of them corresponds to special conditions. For example, if in the design, the model is established in open space without any perturbations, there will be two choices to make: **Open and open (add space)**. Choose "**open**" if the calculation is too heavy or "**add space"** may be closer to an anechoic chamber.

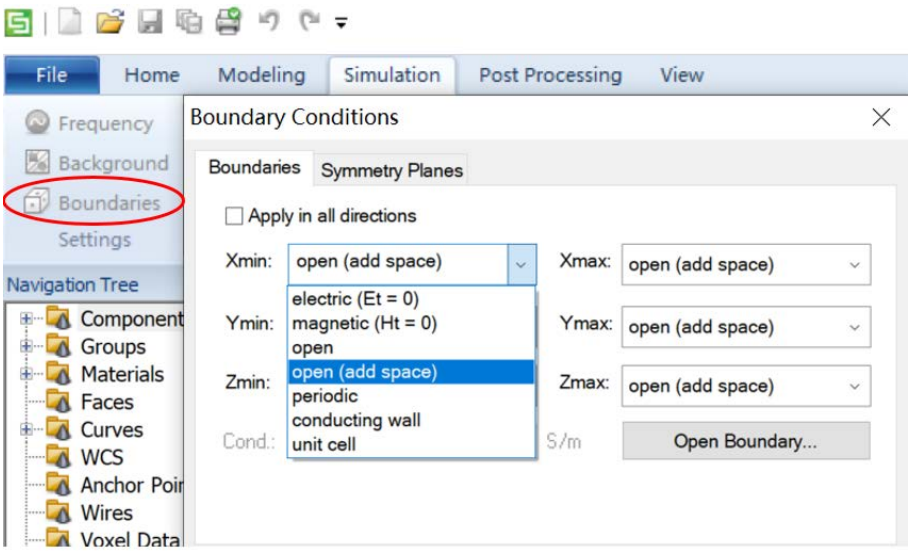

Figure 2.17 Boundary condition setting in CST

Before simulations, necessary field monitors have to be created to observe the results, otherwise, the simulation will be run in vain. For other results that are more complicated, **Post Processing-Results templates** panel should be used.

2.4.2 Setup solver

In CST, there are in total 6 kinds of solver that we could use. For modeling that uses the Finite Integration Technique, the time domain (TD) solver and the frequency domain (FD) solver are usually in use. For these two different type of solvers, their configuration panels are shown in Figure 2.18.

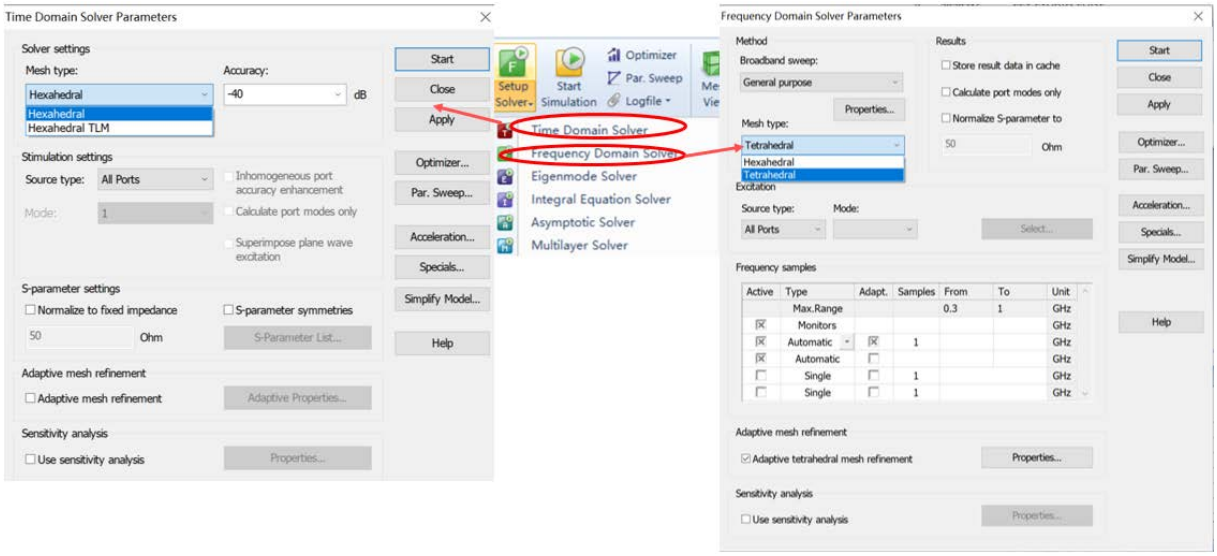

Figure 2.18 Panel comparison between the time domain solver and the frequency domain solver

The most evident difference between the two kinds of solvers is that: TD solver could cover a large band of frequency without too much calculation while FD solver takes

longer time but with higher accuracy at each frequency point. Also, TD solvers only allow hexahedral mesh while FD solvers allows also the tetrahedral mesh. With an hexahedral mesh, the computation is faster but it is not possible to change the mesh density along any axis direction in the calculation box (see Figure 2.18). Since the studied model has a huge difference in size (antenna is of tiny size. the finest slot measures only 0.1 mm large and the arm model is 160 mm long), using hexahedral mesh may cause a lot of unnecessary calculations.

Furthermore, TD solver is configured by the attenuation rate, it ceases calculating when the signal becomes weaker than a certain value while FD solver is configured by the mesh refinement at defined frequencies.

The mesh density should also be configured before the simulation starts.

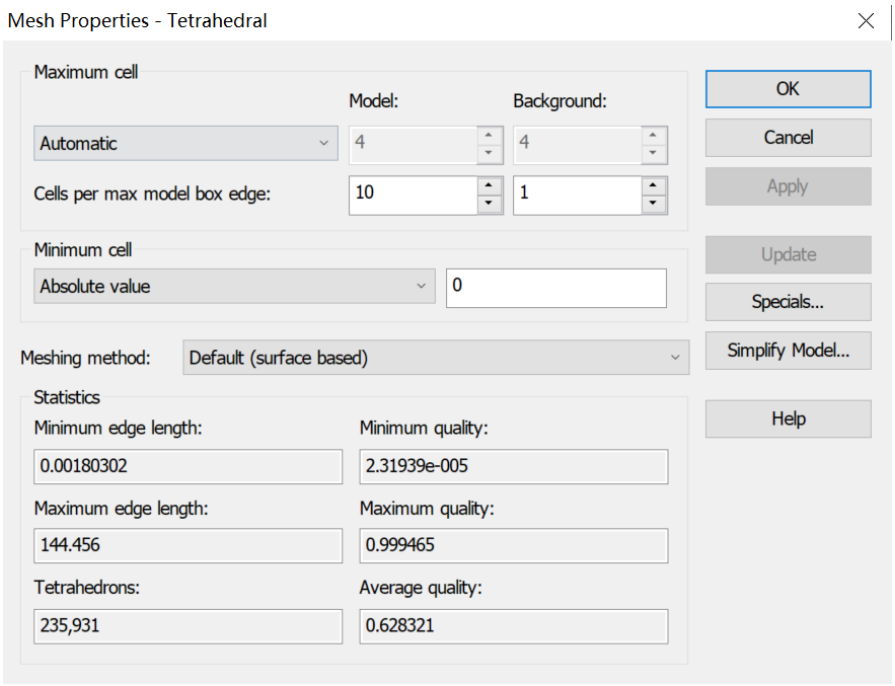

Figure 2.19 Mesh configuration panel

There are two kinds of zones to be configured. The simulation model and the zone inside the calculation box where there is no model. By changing the "**automatic"** to "**cell per wavelength",** the mesh density could be modified manually.

Finally, by applying "**parameter sweep**", a series of simulation could be launched successively without pause, all 1D and 2D results are saved and numbered automatically. See Figure 2.20, three kinds of parameter's variations are possible.

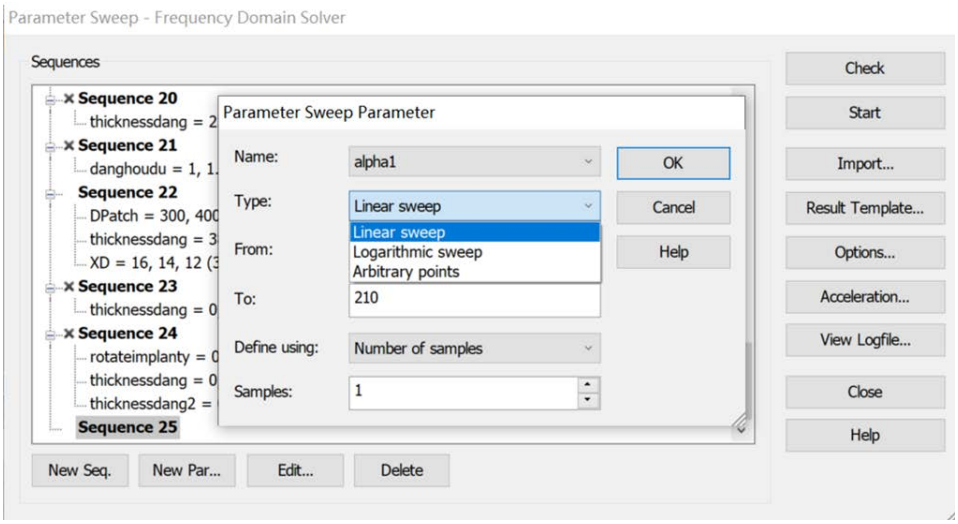

Figure 2.20 Parameter sweep panel

2.4.3 Results observation

After the calculation is finished, the visualization of results is possible through the result menu on the left side (see Figure 2.21).

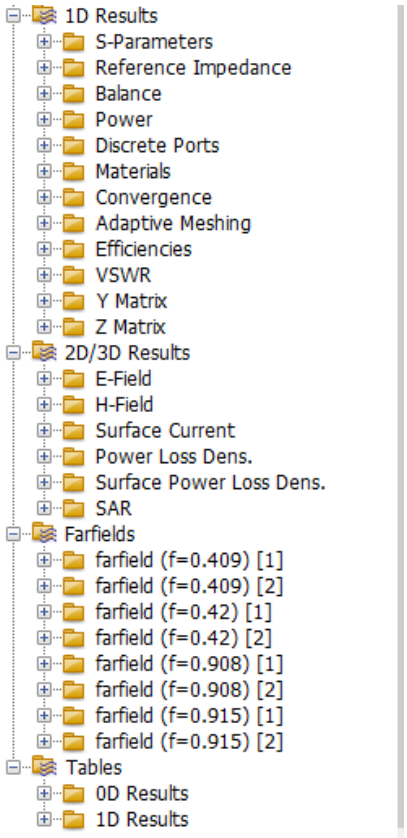

Figure 2.21 Results visualization menu

The result types are preset in the 1D results folder. For the rest, they are defined by users by adding monitors. **Far-field** results could be visualized for each port, but only

for the frequencies that are defined by the user before the simulation. In **Tables** are the results defined in "**Results templates"** panel.

Among all results, only **1D Results** and **Tables** could be saved for each simulation during the **parameter sweep.**

2.5 Conclusion

In this chapter, a miniaturized circular antenna is designed for a deep-body wireless biomedical application. The antenna is circular and miniaturized, as it only has a radius of 5.5 mm. It has 2 different resonant frequencies: 403 MHz (MedRadio band) and 915 MHz (ISM band). The impact of various parameters of the antenna (ex. slot radius) is discussed. The three-layer cylindrical human tissue model (bone 25 mm, muscle 25 mm-47.5 mm, and skin 47.5 mm-50 mm) is used in the simulation. For each resonant frequency of the antenna, the gain of the antenna (in-body) is -33.65 dB for the 403 MHz band and -29.45 dB for the 915 MHz band. Finally, some CST manipulation details are discussed.

Comparing with the antennas mentioned in Chapter 1, the antenna in this thesis is smaller, non-sharp-edge, and with relatively high efficiency among those who have similar sizes. This proves the superiority of the proposed design above other existing works mentioned in chapter 1 and the value of current work.

Chapter 3

Transmission link establishment and results

3.1 Introduction

In this chapter, the transmission scenario between an external patch antenna as an emitter, and a miniaturized deep in-body implanted circular antenna as a receiver is presented. The scenario with link budget will be carefully studied and presented. The global transmission scenario is presented in Figure 3.1.

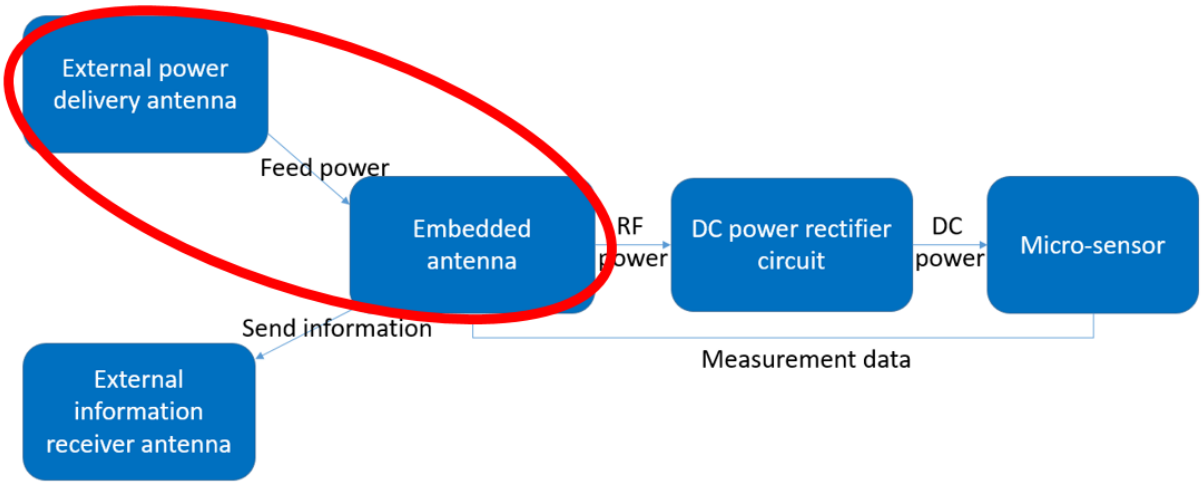

Figure 3.1 Simplified wireless power system operation (circled)

An external power delivery antenna emits power from the outside, and the embedded antenna receives this power inside the human body.

3.2 FRIIS equation and transmission efficiency [74]

Let us assume that one antenna is transmitting power to another one, and the distance between them is $R > 2 \cdot \frac{L^2}{\lambda}$ (the Fraunhofer distance, which defines the far-field range) where L is the largest dimension of each antenna and λ is the operating wavelength. The transmitting scenario is presented in Figure 3.2.

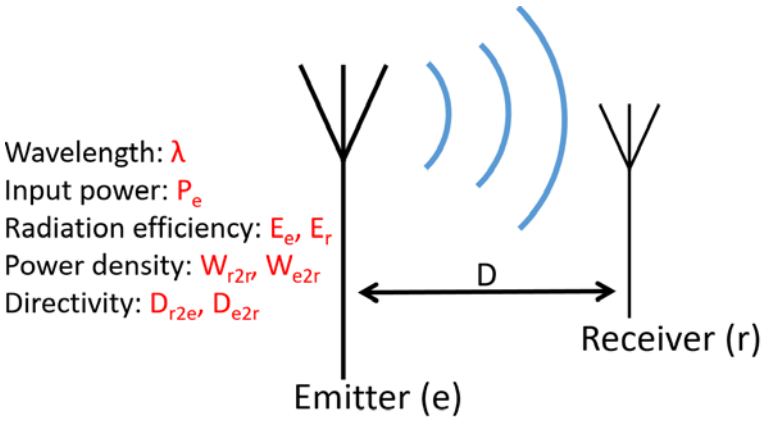

Figure 3.2 Simplified power transmitting scenario (two antennas)

The power density that the Emitter radiates in the direction of the Receiver is [74]

(3-1)

$$W_{e2r} = \frac{P_e \cdot E_e \cdot D_{e2r}}{4\pi R^2} \cdot (1 - |S_{11}|^2)$$

where P_e is the input power into the Emitter, E_e is the radiation efficiency of the Emitter antenna (the ratio between the power radiated and the input power), D_{e2r} is the directivity of the Emitter antenna towards the Receiver antenna, S_{11} is the reflection coefficient of the Emitter antenna.

The effective area of the Receiver antenna is defined as:

$$A_r = \left(\frac{\lambda^2}{4\pi}\right) \cdot E_r \cdot D_{r2e} \cdot (1 - |S_{22}|^2) \tag{3-2}$$

where λ is the wavelength, E_r is the radiation efficiency of the Receiver antenna and D_{r2e} is the directivity of the Receiver antenna towards the Emitter antenna, S_{22} is the reflection coefficient of the Receiver antenna. Under the hypothesis in [74], the relationship between the power received by the Receiver antenna P_r and the input power into the Emitter antenna P_e is written as follows:

$$P_r = W_{e2r} \cdot A_r = \left(\frac{\lambda}{4\pi R}\right)^2 \cdot P_e \cdot E_e \cdot E_r \cdot D_{e2r} \cdot D_{r2e} \cdot (1 - |S_{11}|^2) \cdot (1 - |S_{22}|^2) \tag{3-3}$$

by ignoring the reflection losses, reflection coefficients are all equals to 0. Thus the simplified transmission efficiency is

$$\frac{P_r}{P_e} = (\frac{\lambda}{4\pi R})^2 \cdot (E_e \cdot D_{e2r}) \cdot (E_r \cdot D_{r2e}) \tag{3-4}$$

Meanwhile, in the scattering matrix form, considering the transmission system is a two-port system (see Figure 2.8), the input power into the Emitter antenna is written as:

$$P_{input} = P_e = \frac{P_{radiated}}{(1 - |S_{11}|^2)} \tag{3-5}$$

By applying the previous assumption, the input power is equal to the radiated power, during the transmission:

$$P_{radiated} = \frac{|V_1^+|^2}{2Z_0} \tag{3-6}$$

where $V_1^+$is the incident wave of this two-port system and assuming that Z_0 is the standardized impedance for port 1 and port 2. Since Z_0 has the same value at both 2 ports, the power transmission efficiency is now written as:

$$\frac{P_r}{P_e} = \frac{P_{received}}{P_{radiated}} = \frac{\frac{|V_2^-|^2}{2Z_0}}{\frac{|V_1^+|^2}{2Z_0}} = \frac{|V_2^-|^2}{|V_1^+|^2} = |S_{21}|^2 \tag{3-7}$$

As in CST Software, the $|S_{21}|$ value in Decibel is calculated as 20log(S_{21}), when the antenna is matched, the S_{21} value in dB is considered approximately as the power transmission efficiency of this power transmission system.

3.3 Power emitter standard

As mentioned in chapter 2, the designed antenna has two different operating frequencies in MedRadio band (402 MHz) and in ISM band (915 MHz). It is important that the designed system fits the international regulation when it operates. Also, a major point is to identify the frequency band in which the antenna can receive more power.

3.3.1 MedRadio band (402 MHz)

For the 402MHz MedRadio band, it is noted in "Electronic Code of Federal Regulations (e-CFR), CFR § 95.2567-MedRadio radiated power limits." that [69]:

"95.2567 MedRadio radiated power limits.

…

(b) Transmitters excepted from frequency monitoring - 401-402 MHz and 405-406 MHz. For MedRadio transmitters that are excepted under § 95.2559(b)(2) or (3) from the frequency monitoring requirements of § 95.2559(a): The Maximum EIRP of any transmitter operating in the 401.85-402 MHz band must not exceed 25 microwatts in any 150 kHz bandwidth."

https://www.law.cornell.edu/cfr/text/47/95.2567

The maximum EIRP of the antenna at 402 MHz cannot exceed -16 dBm according to this regulation. (EIRP, whose full name is Effective Isotropic Radiated Power, which is the total power in watts that would be radiated by an isotropic antenna (ex. half-wave dipole antenna) to give the same radiation intensity as the actual source antenna at a distant receiver located in the direction of the antenna's main lobe.)

3.3.2 Industrial, Scientific, Medical (ISM) band

For the 902.5-928 MHz band, it is marked in "FCC 15. 209, Standard Specification for Radiated emission limits, general requirements" that [70]:"

- **Maximum transmitter output power, fed into the antenna, is 30 dBm (1 watt).**
- **Maximum Effective Isotropic Radiated Power (EIRP) is 36 dBm (4 watt). One can obtain the EIRP by simply adding the transmit output power, in dBm, to the antenna gain in dBi (if there is loss in the cable feeding the antenna you may subtract that loss). "**

http://afar.net/tutorials/fcc-rules/

The maximum EIRP of the antenna at this frequency band cannot exceed 36 dBm with the input power fed into the antenna not exceeding 30 dBm.

By applying these regulations and the gain results in the previous chapter, the transmission is at much higher levels in ISM band than in the MedRadio band. Due to this huge difference (-16 dBm vs 30 dBm), the power transmission is realized in the ISM band around 915 MHz. The MedRadio band is chosen to be the information exchange link.

3.4 Transmission structure

In the previous chapter, the positioning of the embedded antenna according to the three-layer cylinder (simplified as "arm" below) was already presented. The structure of the power transmission system is described in Figure 3.3. The three-layer model is used as an electromagnetic simulation environment. Differently from the previous model, an external antenna represents the Emitter antenna and is placed at the same side of the "arm" with the embedded antenna. This is a rectangular patch antenna of 62.5 mm x 43.5 mm, fed by a microstrip at the longer edge. The reason of this choice will be explained in section 3.4.1 below. A metallic reflector is placed behind the "arm" in order to reflect the wave and thus to enhance the power reception. The geometry of the reflector will be discussed in 3.5.2.

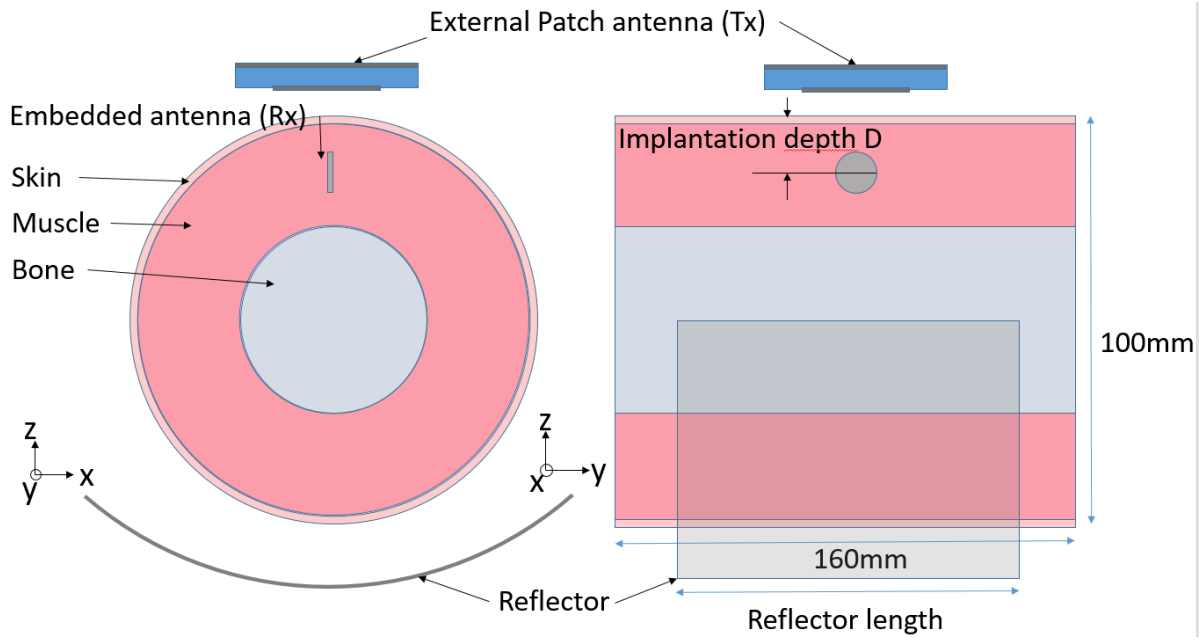

Figure 3.3 Power transmission link design

3.4.1 External antenna choice

Since the antenna is miniaturized and embedded deep inside the body (which leads to higher losses and lower transmission efficiency), an appropriate and independent external power emitter is necessary in order that the in-body antenna could capture more power. Since the external antenna is placed outside the body, the size is no longer a constraint for it. So here a half-wavelength dipole and a standard size patch antenna are chosen for the first hand due to the simplicity. The dipole antenna has lower gain in one direction, but it has a larger radiation area which is immune to the disorientation while patch antenna has a more concentrated radiation zone (a half-wavelength dipole has a directivity of 2.6 dB while a patch antenna should have a gain over 4 dB).

With the same transmission distance of 600 mm and implantation depth of 14 mm, the S_{21} values of the dipole-antenna system and the patch-antenna system are shown in Figure 3.4:

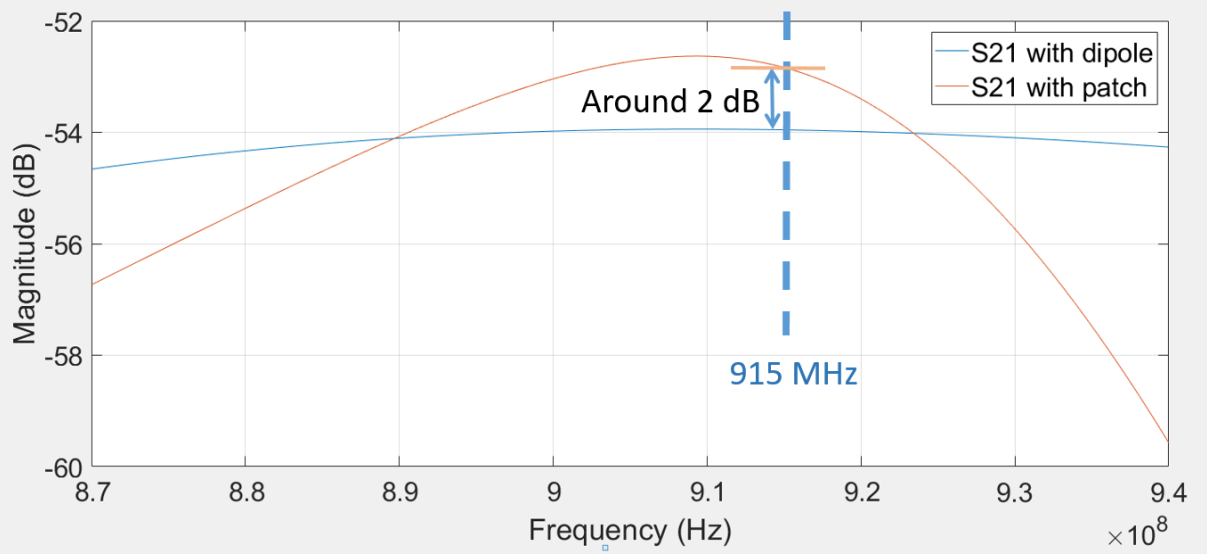

Figure 3.4 Comparison of the transmission system with dipole or patch as emitter

As we can see, when using the patch antenna, in the same condition, the S_{21} value is higher for about 2 dB than using the dipole, which corresponds approximately to the gain difference of the two antennas. Therefore, the patch antenna is chosen as the emitter since it could deliver about 4 times more power to the Receiver antenna.

3.4.2 Reflector design

The metallic reflector is created with the aim of enhancing the transmission link. The basic ideal transmission enhancement is shown in Figure 3.5. It is worth saying that the reflector, together with the Emitter antenna, is fixed but not to be worn by the patient.

This whole transmission system should be only in use while the embedded medical device needs to be charged.

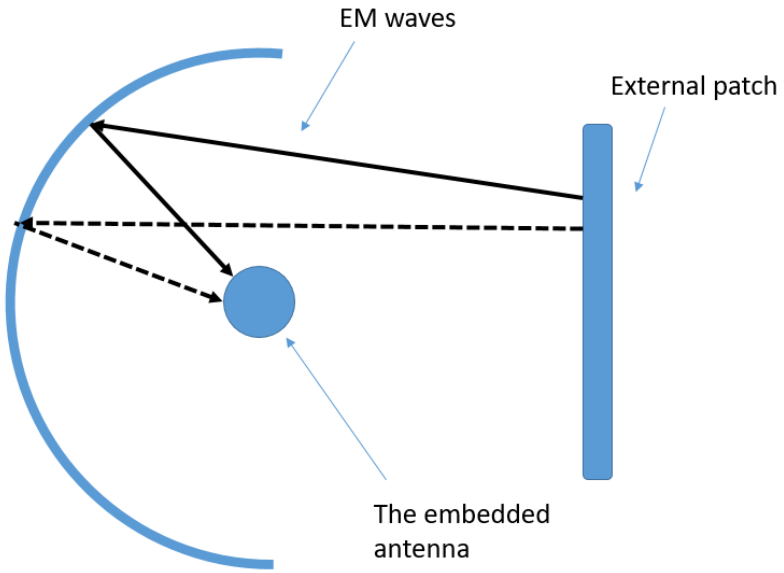

Figure 3.5 Ideal transmission scenario

The EM waves (which are simplified to arrows and illustrated in Figure 3.5) which come from the external patch antenna (simplified as "the patch") are reflected and concentrated on the embedded antenna. This minimizes the power flowing in other directions apart from the embedded antenna. Since the patch is a surface and the embedded antenna's size is much smaller than the patch so that it could be considered as a point, the reflector should be designed as a shape between parabolic and elliptic in order to maximize the enhancement due to geometric reasons.

However, due to the complexity of fabrication, a cylindrical reflector is more practical and simpler to handle. A comparison between the elliptical and cylindrical reflector will be presented in the following numerical results section.

The material of the reflector could be chosen as copper, iron or aluminum, since the corresponding skin depths at 915 MHz are all very tiny (<10 μm). As for a reflector of 1 mm thickness, the gain enhancement of the embedded antenna should not have much difference between the three materials, which will be illustrated in section 3.5.

3.5 Numerical results

This section presents the different numerical results under various conditions which implement the best parameters for the design in each case. In the following studies, S_{21} is considered as the judging standard.

3.5.1 Antenna's positioning

As studied in the previous chapter, the antenna is linearly polarized and radiates towards its lateral side direction. The possible positioning of the antenna still has two free dimensions to decide: The rotation around Y and X axis. Due to the symmetry, for the rotation around Z-axis, only two positions are tested: Embedded antenna's (simplified to 'implant') ground plane in XY plane (0°) and in XZ plane (90°), with the external patch fixed at 200 mm away from the implant. The comparison is shown in Figure 3.6:

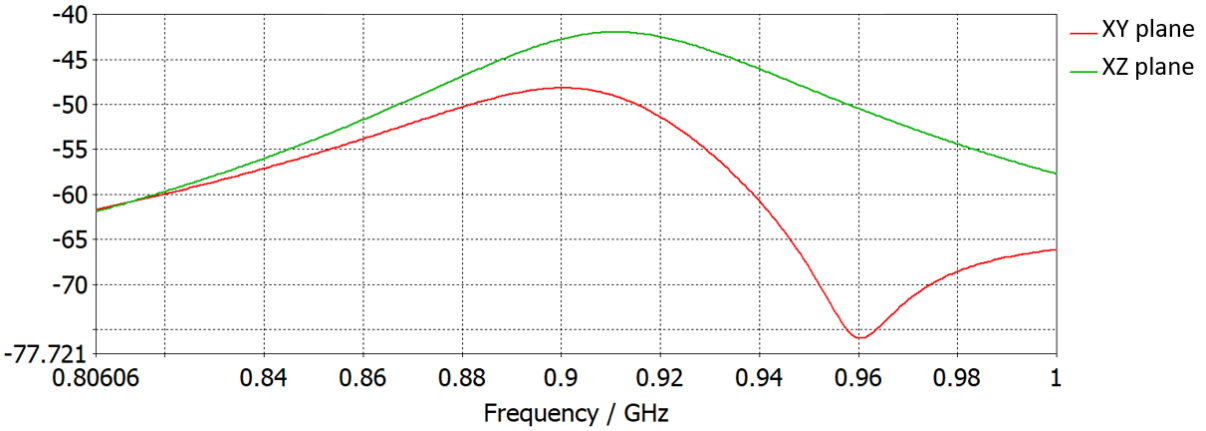

Figure 3.6 Comparison of the implant's positioning

As we can see, the power transmission efficiency is around 5 dB stronger in XZ plane than in XY plane, thus the implant should be implanted in the XZ plane as shown in Figure 3.3. Furthermore, the implantation in this direction could also ease the movement of the patient's arm, since it is implanted in the same direction as the muscle fiber [75]. This would not hamper the contraction of the muscle fibers.

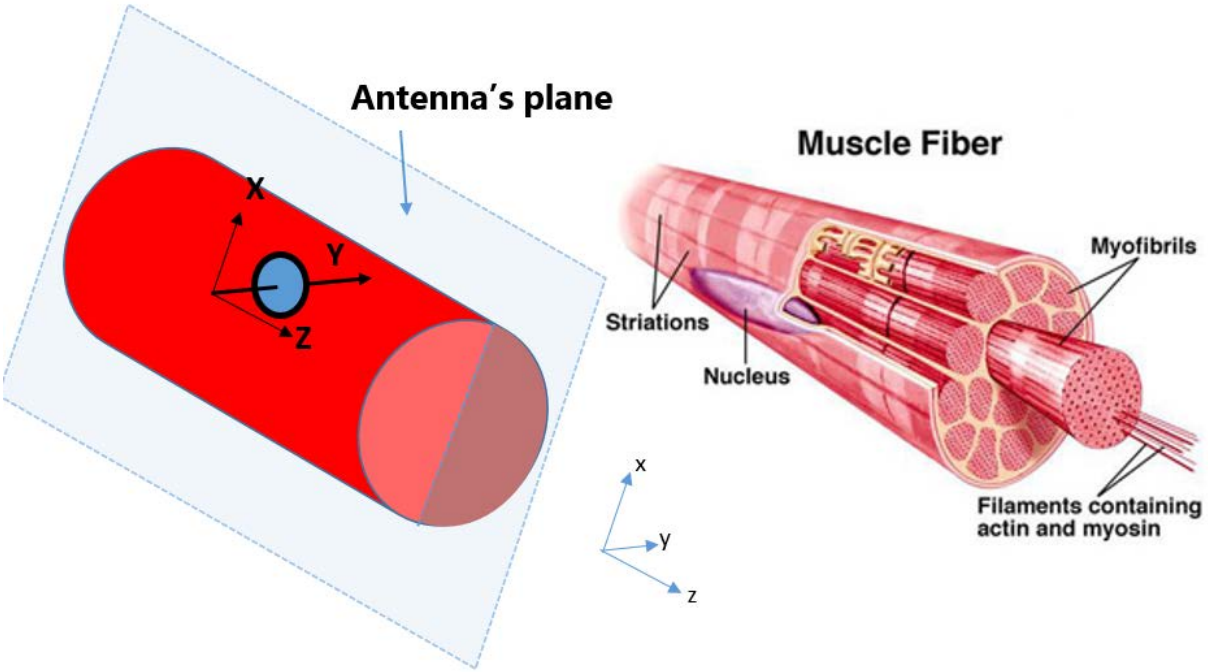

Figure 3.7 Simplified Figure of the antenna and the muscle fiber in arm [74]

For the rotation around Y axis, there is not much symmetry. Therefore, testing values are set every 40° to find out the best position. The result Figure is presented as follows in Figure 3.8:

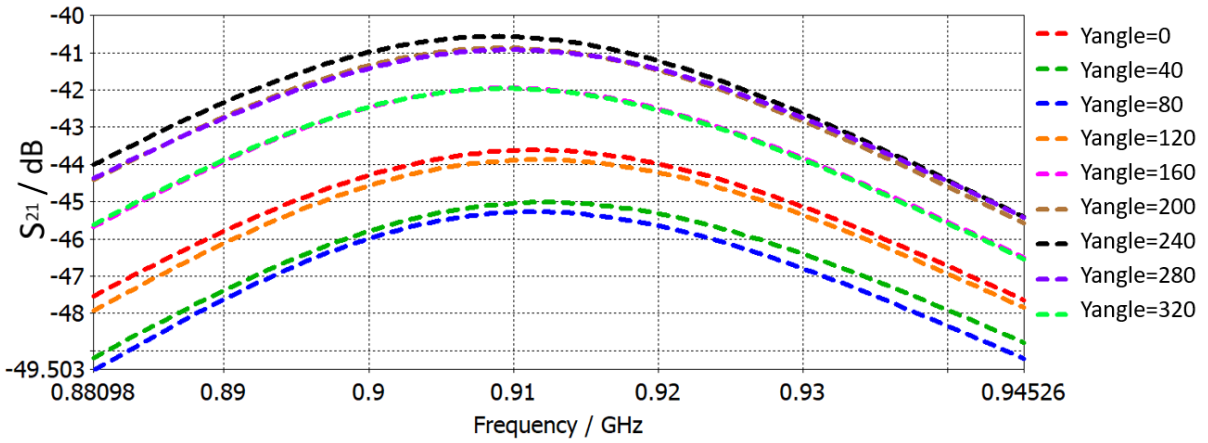

Figure 3.8 Transmission efficiency with rotation angle around Y axis

We can observe in Figure 3.8 that there exists an optimum angle which has the highest S_{21} value. When the Yangle is 240°, the antenna position is presented in Figure 3.9:

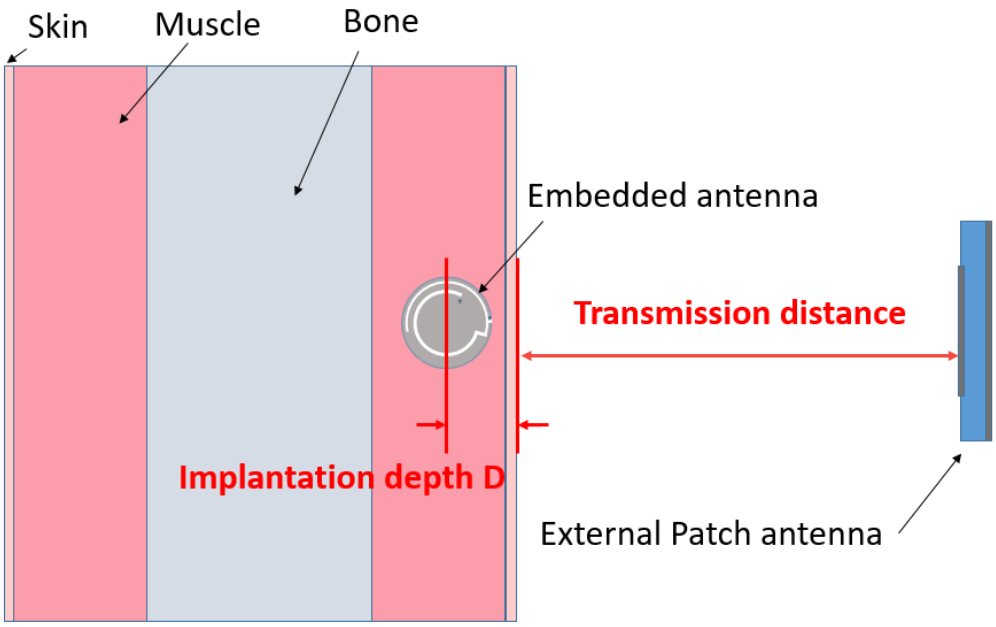

Figure 3.9 Embedded antenna positioning in the 'arm' model

In a realistic use, it should be indicated on the antenna's surface in which direction it shall be implanted, since a bad positioning may cause in maximum 10 dB difference in power transmission efficiency

3.5.2 Transmission distance

3.5.2.1 Implantation depth

As we mentioned before in Table 2.2, since human tissues have high conductivity and thus are lossy, the implantation depth should have impact on the transmission efficiency. Here we analyze the example where the external patch is 400 mm away from the implant. The implant positioning is chosen as the most optimum as previously calculated. In each case, the implant is embedded 10, 12, 14, 16 mm from the skin surface (see Figure 3.9). The transmission efficiency is calculated in Figure 3.10:

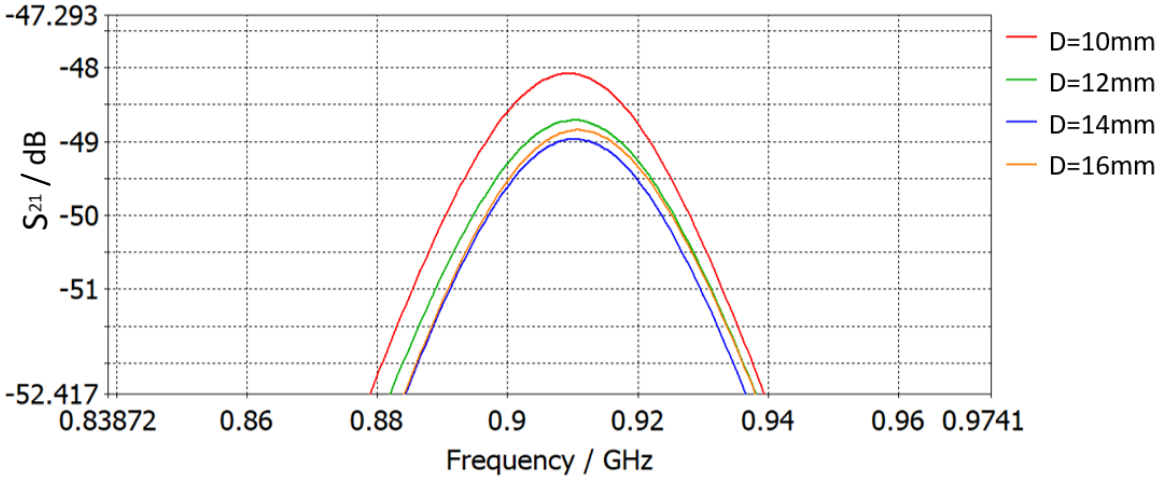

Figure 3.10 Transmission efficiency with different implantation depth D (external patch at 400 mm away)

As we can see, the deeper the implant is embedded, the lower the transmission efficiency is. However, when a certain depth is reached, for example 14 mm, the S_{21} value does not change as much as before. From this value, the implantation depth does not affect the nearfield of the antenna anymore, thus it has less effect.

3.5.2.1 Transmission distance

Apart from the implantation depth, the location of the external patch emitter is also important. However, first of all, in order that the transmission be stable, it must operate at far-field range. The criteria to identify the far-field range is the Fraunhofer distance:

$$d = \frac{2L^2}{\lambda} \tag{3-8}$$

where L is the largest dimension of the antenna.

Since the external patch is larger than the embedded antenna, its Fraunhofer distance should be the criteria to judge the far-field operation range. By taking into account the environmental change and other issues, the external patch antenna measures 63.5 mm x 43.5 mm with the same substrate as the embedded antenna (Rogers RO3210). Therefore, the reactive nearfield range ($0.62 \cdot \sqrt{\frac{D^3}{\lambda}}$) is 23.1 mm and the radiative far-field range is 36.1 mm. In Figure 3.11, several transmission distances (defined in Figure 3.9) are tested in order to obtain the transmission efficiency results. The result for 200 mm is also evaluated since it is in the far-field range of the embedded antenna.

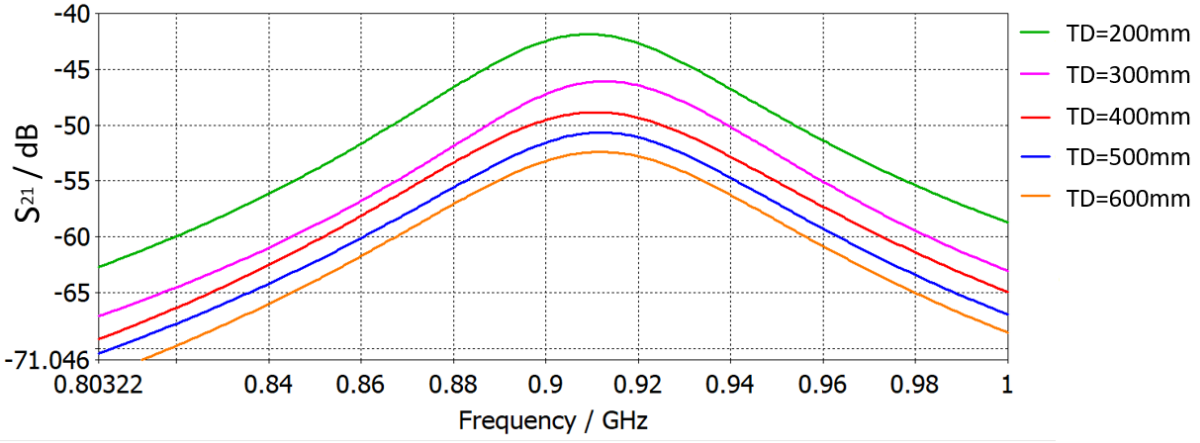

Figure 3.11 Transmission efficiency with different transmission distance (implantation depth = 14 mm)

As we can see, the transmission efficiency lessens homogenously as the operation distance reaches the far-field range. When the emitter antenna is 300 mm away from the implant, the ideal transmission efficiency is around -46 dB.

3.5.3 Reflector issues

This section mainly discusses the impact of different parameters of the reflector on the enhancement of the transmission efficiency.

3.5.3.1 Reflector's geometry

Figure 3.5 shows the ideal structure of a reflector and how it works. According to the geometrical optics approaches, if high frequency EM wave could be represented as a distribution of vectors in a 2D plane, the reflector should be parabolic with a planar incident wave. But the external patch is not far or large enough to produce plane wave, so an elliptical reflector may be more appropriate. The ellipse has its two focal points at the embedded antenna's and the external antenna's positions. Its focal distance equals to the average of the sum of transmission distance and implantation depth. The geometry of the elliptical reflector is shown in Figure 3.12.

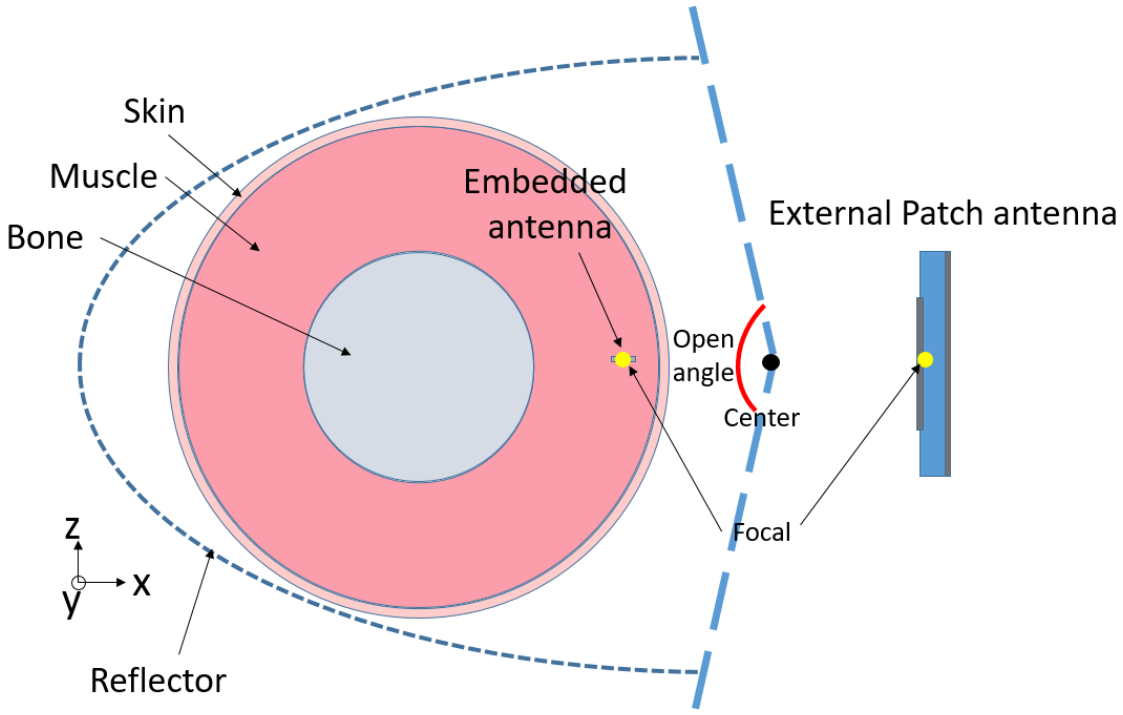

Figure 3.12 Reflector's geometry (elliptical)

However, due to the complexity for the fabrication and the difficulty to find the focal point in the realistic case, an elliptical reflector is not as practical as a cylindrical one. Therefore, a comparison of enhancement capacity (the S_{21} difference) between an elliptical and a cylindrical reflector is necessary. In Figure 3.13, the transmission efficiencies are compared with transmission distances of 400 mm (far-field), implantation depth of 14 mm and a copper reflector with open angle = 210°. For the

cylindrical reflector, the antenna is located at the half-radius point of it. For the results in Figure 3.13, the reflector is made in copper.

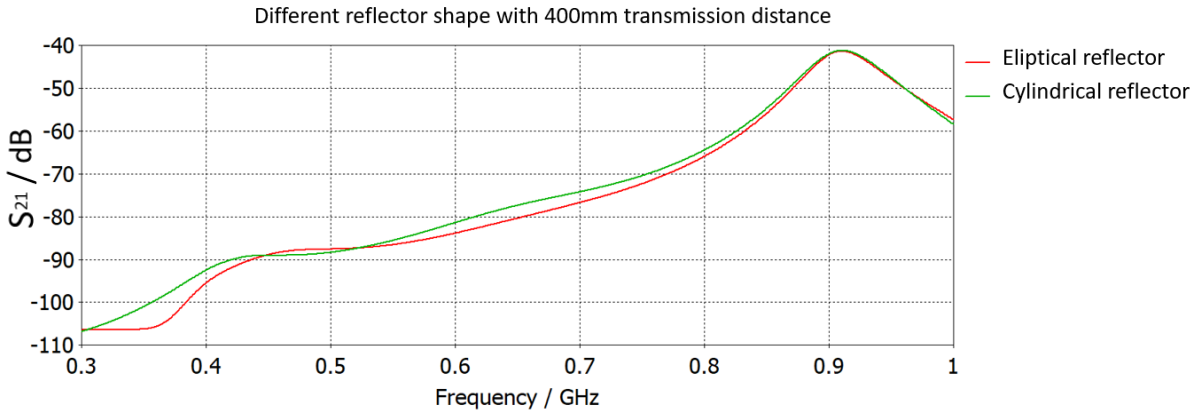

Figure 3.13 Transmission efficiency with different reflector's geometry

As observed in the two Figure 3.13, in the mid-field range (a distance between Fresnel distance and Fraunhofer distance), the elliptical reflector has better enhancement than the cylindrical one but when comes to the far-field (further than Fraunhofer distance), the enhancement at 915 MHz has no longer difference. In fact, according to simulations results, with a transmission distance less than 500 mm, a cylindrical reflector could replace the original theoretical elliptical one since they have no significant difference. Therefore, in the following simulations, the reflector is all cylindrical.

3.5.3.2 Reflector's material

In the reflector's design section, we have mentioned that at 915 MHz, all the common metals such as: Copper, aluminum, iron have low resistivity and thus have extremely small skin depth. This means they are suitable as the reflector's material. However, it is still worthy and necessary to compare their enhancing abilities in order to optimize the results. In Figure 3.14, the S_{21} comparison between different reflector's materials are presented:

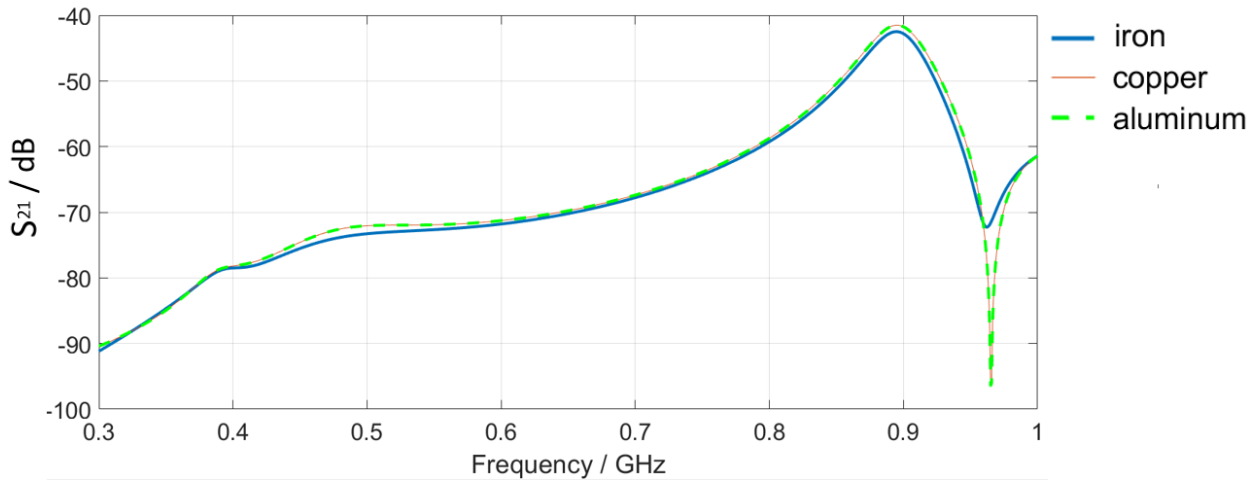

Figure 3.14 Transmission efficiency with different reflector's material

As observed, the reflector in copper (resistivity = 1.7×10^{-8} Ω·m) and the one in Aluminium (resistivity = 2.8×10^{-8} Ω·m) have almost the same enhancing effect. As for the one in iron (resistivity = 1.0×10^{-7} Ω·m), the S_{21} value is slightly (1 dB) lower than the other two. This is because comparing with aluminum and copper, iron has a higher resistivity and thus more power is dissipated inside the reflector.

3.5.3.3 Reflector's open angle

The open angle of the reflector is a key factor. It determines the amount of power that could be reflected and received by the embedded antenna. Here the transmission scenario is realized with a transmission distance of 600 mm (far-field) and an implantation depth of 14 mm. The reflector is made of aluminum. The relationship between the transmission efficiency enhancement and the reflector's open angle at 915 MHz band (defined in Figure 3.12) is presented in Figure 3.15:

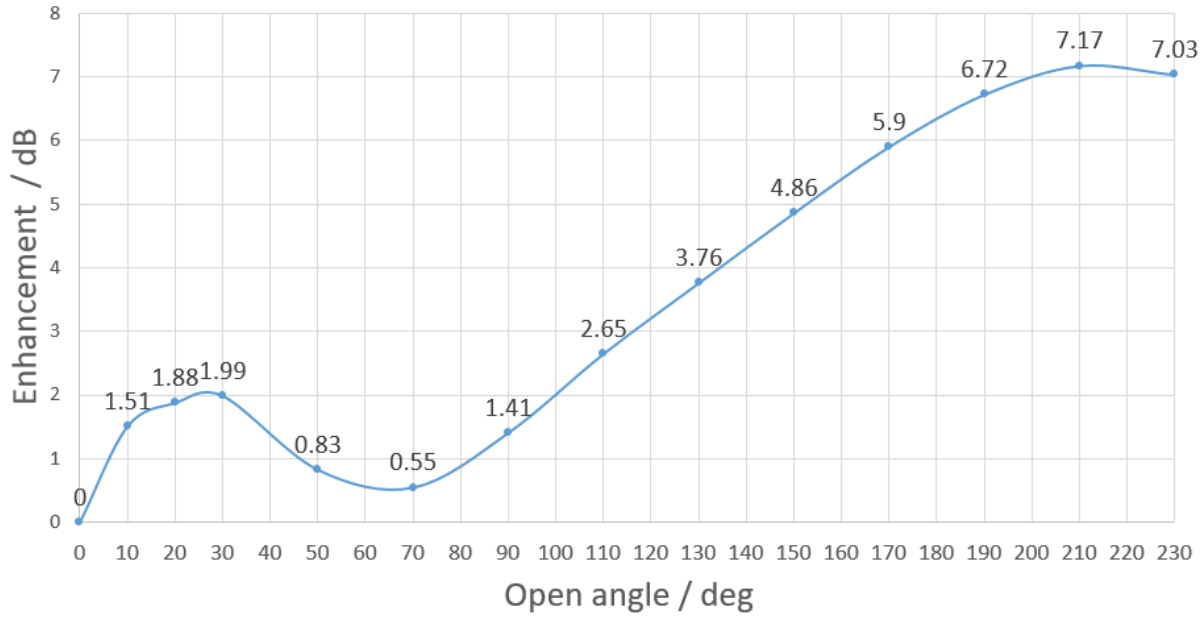

Figure 3.15 Transmission efficiency with reflector open angle

The S_{21} results are not monotonous with the increase of the open angle. There exists a local extremum at 30°. The enhancement at 30° is the best among all angles under 100°. The other extremum appears at 210° which is also the highest value. Therefore, in realistic cases, it is suggested that with a limited space which could not afford a reflector larger than 100°, a 30° reflector appears the best option.

Last but not the least, we include all previous results in order to achieve the highest enhancement value. The transmission efficiency enhancement (increased value of S_{21}) caused by the reflector at 915 MHz band is presented in the following Table 3.1.

Table 3.1 Reflector enhancement in different situations

Enhancement (dB)		Transmission distance (mm)			
		300	400	500	600
Implantation depth (mm)	12	6.3	7.3	8.3	7.2
	14	6.5	7.8	7.5	7.5
	16	6.7	7.7	7.7	7.6

It can be observed that the enhancement reaches its maximum value when the transmission distance is around 500 mm, which is in the far-field range. In fact, for different transmission distances, the position of the reflector should be slightly adjusted in order to fit this change.

3.5.3 SAR issues

It has been introduced in the previous chapter that SAR is an important standard to measure if there is any negative effect from the EM device on human body. Here, for the 915 MHz band, for different implantation depths and transmission distances, the corresponding SAR of human tissue every 1 g-average and 10 g-average is shown in the following Table 3.2. It needs to be verified that even with the reflector, all are in the safe range. For the 402 MHz band, the power is a lot lower than the value below so those values are not presented here.

Table 3.2 SAR values in different situations

SAR value (W/kg)		Implantation depth (mm)	Transmission distance (mm)			
			300	400	500	600
With reflector	1 g-average (<1.6)	12	0.128	0.103	0.061	0.041
		14	0.122	0.097	0.057	0.039
		16	0.130	0.099	0.059	0.040
	10 g-average (<2)	12	0.093	0.076	0.045	0.030
		14	0.093	0.074	0.044	0.030
		16	0.095	0.073	0.044	0.030
Without reflector	1 g-average (<1.6)	12	0.039	0.023	0.016	0.010
		14	0.037	0.021	0.015	0.009
		16	0.038	0.022	0.015	0.009

	10 g-average (<2)	12	0.029	0.018	0.012	0.007
		14	0.029	0.018	0.012	0.007
		16	0.028	0.017	0.011	0.007

It is not difficult to see from the statistics in the Table 3.2 that even in the strongest case, the SAR value is much lower than the limit, which means the system does not have any safety problem. Even when the transmission is in the mid-field range, the SAR value still does not exceed the safety limit.

Also, as we have observed in previous figures, the transmission efficiency is much lower for the other operation frequency band. Therefore, the SAR for the other 403 MHz band is not presented here.

3.6 Sensitivity analysis

3.6.1 Polynomial Chaos Expansion (PCE) Method

In the previous sections, a large number of simulations were realized in order to calculate various results. It is interesting to study the impact of each parameter on the results and the relationship among them. Furthermore, when the system will be put in use, a surgery is necessary so as to embed the implantable device. As we studied previously, the positioning of the antenna is of vital importance. Therefore, if there is any unexpected difficulty during the implantation process, knowing which parameter to prioritize is of great necessity.

Polynomial chaos expansion methods are non-intrusive methods and can use 3D solvers as black boxes. They can provide a simple surrogate model of a complex configuration from which values about an observable quantity can be easily studied. Let M be a mathematical model that from N input values (parameters) $x = (x_1, x_2, \dots, x_N)$ generates the output (observable) y given by:

$$y = M(x), \tag{3-9}$$

The input values maybe affected by some random variations or uncertainties. Assuming that the components of the input random vector X are independent, it can be shown that if the random response of the physical phenomena Y has a finite variance, then it can be expressed as an infinite modal expansion, denoted polynomial chaos:

$$Y = \sum_{\alpha} y_{\alpha} \Psi_{\alpha}(X) \tag{3-10}$$

where α is a multi-index, y_{α} are the coefficients, Ψ_{α} are basis functions, multivariate orthonormal polynomials. These polynomials are built using tensor products:

(3-11)

$$\Psi_{\alpha}(x) = \prod_{i=1}^{N} \Psi_{\alpha_i}^{(i)}(x_i)$$

where α denotes the N-uplet $(\alpha_1, \alpha_2, \ldots, \alpha_N)$ divided by subheadings.

These univariate polynomials are a family of orthonormal polynomials with respect to the margin probability density functions (pdf) given by:

$$E[\Psi_k^{(i)}(X_i), \Psi_j^{(i)}(X_i)] = \delta_{jk} \tag{3-12}$$

where δ_{jk} is the Kronecker symbol.

If $f_{X_i}(x_i)$ is the marginal pdf of the random input variable X_i, then from the independence of the input variables then the pdf of X is given by:

$$f_X(x) = \prod_{i=1}^{N} f_{X_i}(x_i) \tag{3-13}$$

In case of uniform or Gaussian input distributions, the corresponding polynomial basis are the Legendre and Hermite polynomials families, respectively. The PCE coefficients can be estimated by using spectral projections or via the use of least-square regressions. The "projection" approach takes advantage of the orthogonality of the chaos polynomials [76].

Let us consider an approximate model $\tilde{Y}$ of the exact model M. The corresponding random output is given by a truncated sum of P polynomials expressed as:

$$\tilde{Y} = \sum_{k=0}^{P-1} a_k \Psi_k(\mathrm{X}) \tag{3-14}$$

The unknown coefficients of the truncation can be estimated through least square regression while minimizing a root mean square error. If we denote y the output vector collecting n values in the vector $y = \left(y^{(1)}, y^{(2)}, \ldots, y^{(n)}\right)$ corresponding to the n inputs x(i) (i=1,...,n) given by $x^{(i)} = \left(x_1^{(i)}, x_2^{(i)}, \ldots, x_N^{(n)}\right)$, then the estimated unknown coefficients derived from a regression approach are given by:

$$\tilde{a} = \{\Psi^T \Psi\}^{-1} \Psi^T y \tag{3-15}$$

where Ψ is the matrix whose coefficients are $\Psi_k^i = \Psi_k(x^{(i)})$.

The validation of the truncated model can be checked using Bootstrap or LOO (Leave-One-Out) validation error. This last approach is a natural definition. If we consider n input values $x^{(i)}$giving n output $y^{(i)} = M(x^{(i)})$, one sample point $x^{(j)}$can be removed and a new surrogate model $M^{PC\backslash i}$ can be built on the basis of $n - 1$ sample values. Then a comparison between the predicted output value with this surrogate

(3-16)

model and the value $y^{(j)}$ can reflects the accuracy of the approach. This leads to the LOO criterion defined as:

$$LOO = \frac{1}{n}\sum_{i=1}^{n}\left(M\left(x^{(i)}\right) - M^{PC\backslash i}\left(x^{(i)}\right)\right)^2 / Var[M]$$

Depending on the targeted accuracy new samples can be added. From computational efficacy point of view, it is important to select the most important polynomials. Then, a further reduction of the basis size can be performed using an adaptive technique, the so-called LARS algorithm (Least angle regression method) [77]. This algorithm identifies the polynomials having the most impact on the output response and on the sensibility indices.

For a global sensitivity analysis, the "Sobol" decomposition [78] is well known. Quantitative estimates of the output sensitivity both to each input individually and to each of possible combinations as well, are straightforward: Thanks to the orthonormality of the polynomial chaos basis, the global variance $\widetilde{D}$ and the partial variances $\widetilde{D}_{i_1,\dots i_s}$ can be expressed with the coefficients of the expansion:

$$\widetilde{D} = Var\left(\tilde{Y}\right) = \sum_{k=1}^{P-1} a_k^2 \tag{3-17}$$

$$\widetilde{D}_{i_1,\dots i_s} = \sum_{\alpha\in\tau_{i_1,\dots,i_s}} a_\alpha^2 \tag{3-18}$$

where $\tau_{i_1,\dots,i_s}$ is the set of α tuples such that only the indices $i_1, \dots, i_s$ are non-zero:

$$\tau_{i_1,\dots,i_s} = \{\alpha\,, \alpha_k > 0, \forall\, k = 1, \dots, N\; k \in (i_1, \dots, i_s)\} \tag{3-19}$$

The indices can be analytically extracted from the PCE [75] and are defined as:

$$S_{i_1,\dots,i_s} = \frac{\widetilde{D}_{i_1,\dots i_s}}{\widetilde{D}} \tag{3-20}$$

3.6.2 Results and discussion

In realistic cases, situations are usually different from that in simulations. Many uncertainties could occur, and some might be important and affect heavily the results. Therefore, studies about probable uncertainties could be useful and necessary for those applications in real life.

Here, some physical variable parameters concerning the human body are discussed. For different people, the radius of their bones, the thickness of their muscle, fat and skin are all different. Also, during the surgery process, the implantation depth and orientation could not be controlled too accurately, so that it could be an uncertainty too.

Moreover, the positioning of the implant in human body could also change due to some bad gesture or possible cases that patient run into. It has been studied in the previous sections that the positioning is important because it could have strong effects on the transmission efficiency. Therefore, the rotation angles of the implants inside the human body should also be considered as uncertainties.

In total, the probable variabilities are listed in the following Table 3.3.

Table 3.3 uncertainty variables and their analyzed range

Physical dimensions	**Name**	**Bone radius B**	**Reflector to skin distance R**	**Fat thickness F**	**Muscle thickness M**	**Implantation depth I**
	Range (mm)	20–40	0–20	1–20	25–40	10–20
Angular dimensions	**Name**	**Around X axis**	**Around Y axis**	**Around Z axis**		
	Range (deg)	0-180	0-360	0-90		

All the calculations in this chapter are performed by the UQLab module in Matlab. [79]

The different variable ranges of human tissue are all determined according to common people. The angles ranges are decided by the geometrical symmetry of the implantable antenna. Due to the different characteristics of the two groups of variables, a separated calculation is necessary.

3.6.2.1 Leave-one-out (LOO) validation error

It could be observed from the formula 3-16 that the LOO is a global indicator of the method's accuracy. Let's assume that all sample points form a set with which a metamodel is established. Then we take out one point and try to reconstruct the value of the point with the metamodel that we just established. Then we compare the reconstructed point with the original result, and calculate the average of the result by traversing all the sample points. Then this average is the LOO error. The less this LOO error is, more accurate is the metamodel.

For distance variables, with 3 sample points for each variable, a set of 3^5 =243 variables is used. The LOO error tendency for distance variables is shown in Figure 3.16.

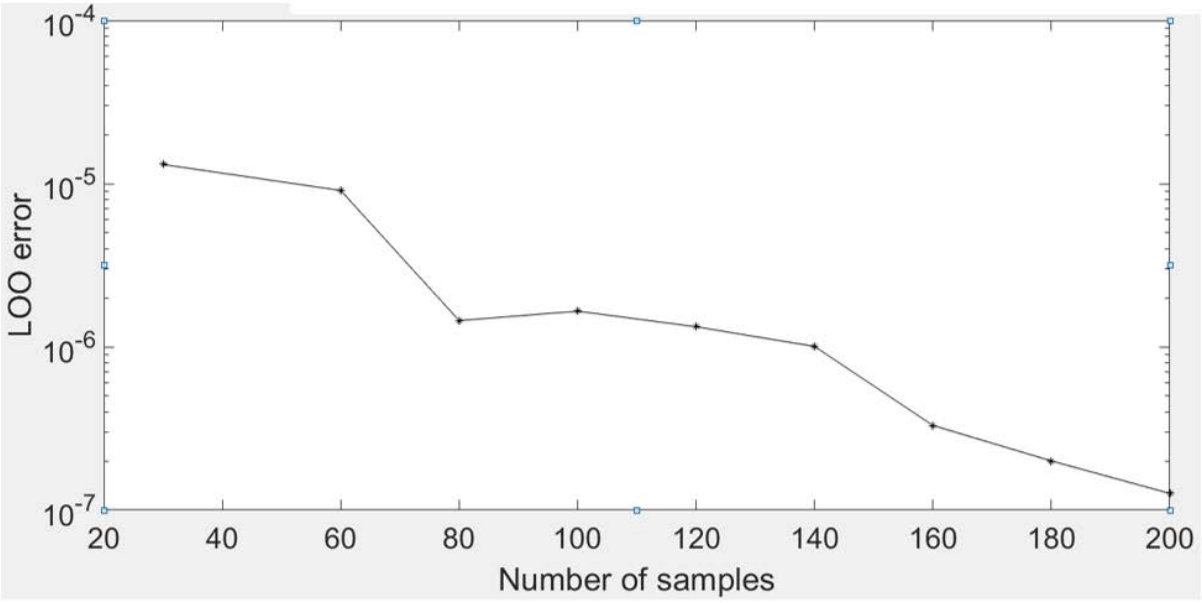

Figure 3.16 LOO Error in log VS number of samples for distance variables.

The LOO error decreases effectively as more samples are included into the database. When 200 sample point are taken into account, the LOO error is 1.2×10^{-7}.

For the angular results, 6 x 8 x 3 (for angles around X, Y, Z axis respectively) =144 configurations are calculated and analyzed. The results are shown in Figure 3.16. The same tendency is observed.

The LOO error results prove the trustworthy of the results. This validates the reliability of the established PCE model and ensure the correctness of the following results.

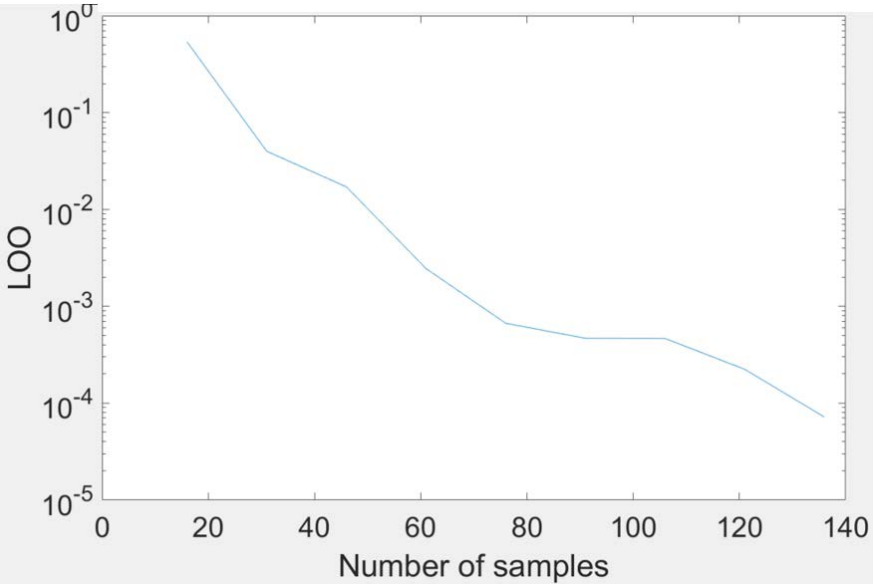

Figure 3.17 LOO Error VS Number of samples for angular variables

3.6.2.2 Sobol indices and sensitivity analysis

Sobol Index is a value that varies from 0 to 1 which indicates the sensitivity of the output against each parameter. More the index is close to 1, more influence this parameter has on the result. With the value of Sobol indices, it is easy to figure out the parameter that should be paid more attention and which one less attention. Each Sobol index of the output S_{21} = S (bone radius B, reflector distance R, fat thickness F, muscle thickness M, implantation depth I) is defined as

$$SobolIndex = \frac{Var\left[E[S_{21}|P]\right]}{Var[Gain]} \tag{3-21}$$

where P is one of the variables (B, R, F, M, I) that affect the output. With the different distance variables, the total Sobol indices for the distance variables are shown in Figure 3.18.

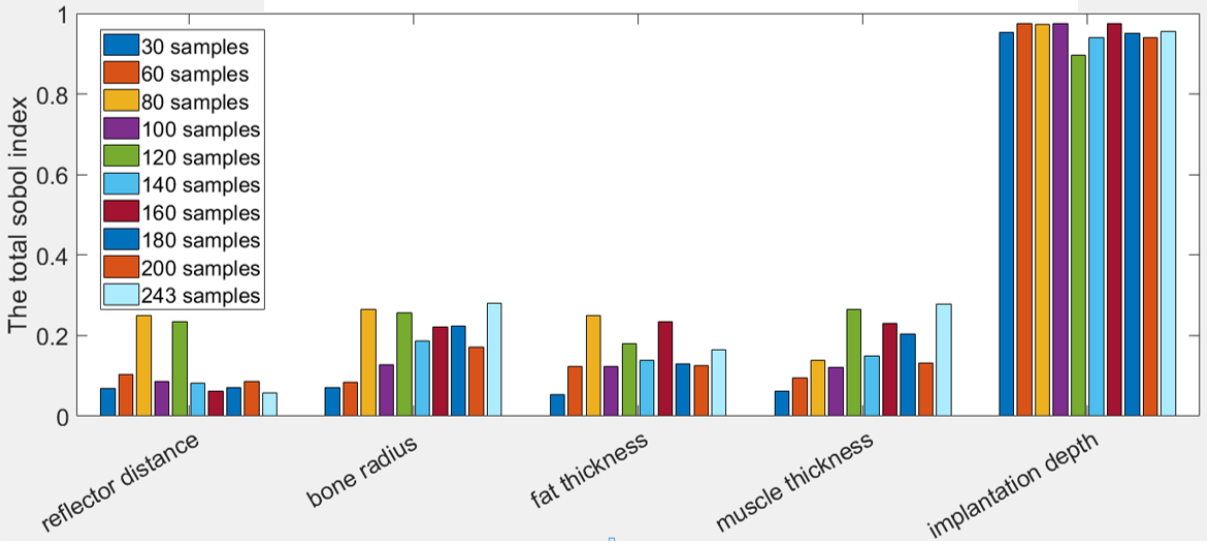

Figure 3.18 Sobol indices VS different parameters under different number of distance samples

As shown in Figure 3.18, the implantation depth is the most important factor among the five different parameters. It is worth pointing out that the implantation depth refers to the distance between the muscle-fat interface and the antenna center. This conclusion could be deduced even with only 30 samples. Therefore, the implantation depth should always be considered during the design and analyze for a wireless power transmission system. For the realistic uses, the biological difference between people are not that important for the transmission efficiency as the implantation depth. This transmission system is suitable for different people.

As for angular variables, the results are as followings:

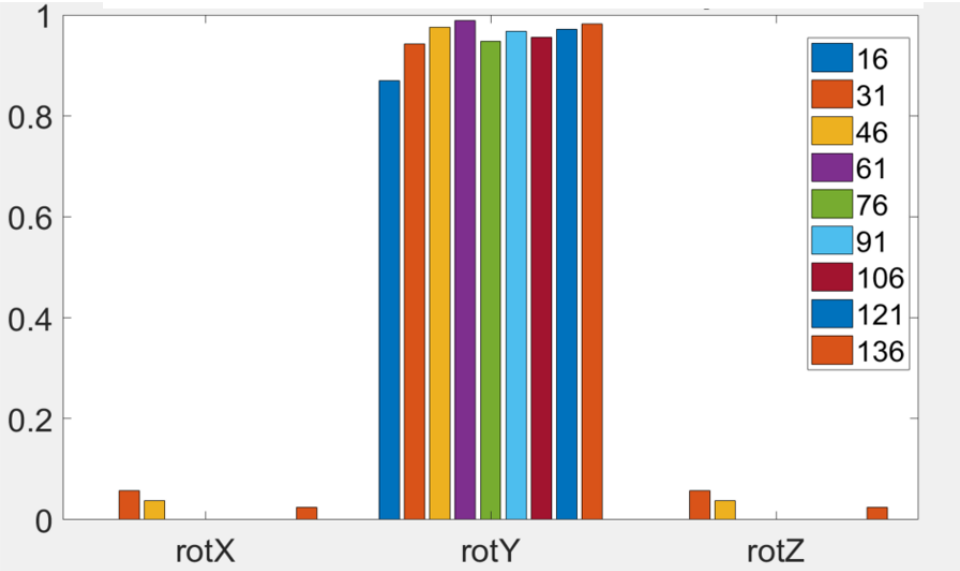

Figure 3.19 Sobol indices VS different parameters under different number of angular samples

As shown in Figure 3.19, the values of the first Sobol index for rotZ and rotX are clearly less important than that of rotY, which shows that the rotation around Y axis (the antenna's symmetric axis) should be paid more attention with. Thus it is strongly suggested that the insert orientation should be marked on the antenna's surface in order to facilitate the surgery procedure and make the insertion angle correct.

3.6.2.3 Result prediction

Another tremendous advantage of using PCE metamodel is that it could predict data points by using only a limited numbers of sample points. This could reduce largely the computation time, especially when the calculation model is complicated or a great number of calculations are needed.

In Section 3.6.2.1, the LOO error value shows that the estimation model could be established with at least 30 samples (LOO error less than 1‰). Here, we take the example for the distance variables, an estimation model is built basing on 60 samples in order to be more accurate. In Table 3.4, some random data points (different from the 60 that build the estimation model) are estimated by using the PCE model and compared with the values that calculated by CST Studio. The absolute errors and relative errors are calculated and presented in Table 3.4. The test sample vector is (bone radius B, reflector distance R, fat thickness F, muscle thickness M, implantation depth I).

Table 3.4. Estimation error at random points for distance variables

Test samples (B, R, F, M, I) (mm)	Simulated gain (dB)	Estimated gain (dB)	Absolute error (dB)	Relative error (%)
(10; 30; 10.5; 37.5; 15)	−29.74	−29.47	0.26	0.90
(10; 36.67; 10.5; 37.5; 15)	−29.03	−28.61	0.42	1.45
(3.3; 30; 10.5; 27.5; 11.67)	−27.81	−27.55	0.26	0.94
(10; 23.33; 10.5; 37.5; 15)	−28.79	−29.25	0.46	1.60
(16.67; 0; 10.5; 32.5; 15)	−28.20	−28.64	0.44	1.56

As presented in Table 3.4, the five randomly chosen points are well estimated with an average relative error around 1.3%. Therefore, this surrogate model established by 60 samples could be used to estimate the real simulation results with an error tolerance less than 2%.

3.7 Conclusion

This chapter mainly discussed the problems about the transmission. It first introduces the theoretical basis of the entire transmission structure and several new configurations in addition to that of chapter 2, including the emitter antenna and the reflector design. Then several comparison results are presented, including the transmission distance issues, the reflector issues. It particularly we discussed the reflector design, from its material to the size and the shape of it by comparing the transmission efficiency. This implantable antenna could achieve around -35 dB (around 0.1%) power transmission efficiency from 400 mm far with all respect of the SAR safe limit. This shows that the design in this thesis has a better performance than any other recent published work considering size and transmission efficiency [43][55].

Finally, a PCE surrogate model is introduced and several meaningful parameters are analyzed for a series of variables. This new analytical method helps to identify the most important parameters and save the computation time with an appropriate accuracy.

Chapter 4

Rectifying circuit design and simulations

4.1 Introduction

In this chapter, a Direct Current (DC) power rectifier circuit is designed and discussed. Several types of designs are compared and analyzed in order to optimize the performance. This part is an important converter which aims at converting the harvested power into the power that could be directly used by an embedded micro-sensor. In many other works, the rectifying circuit part is not completely discussed [34-45]. Some authors think that it is not vital or it refers to another domain - electronics which is different from electromagnetics and belongs to another community.

CST studios could only perform time domain circuit analysis, but frequency domain analysis is more suitable here. Therefore, all the simulations in this chapter are performed by Advance Design System™ (ADS) [80],

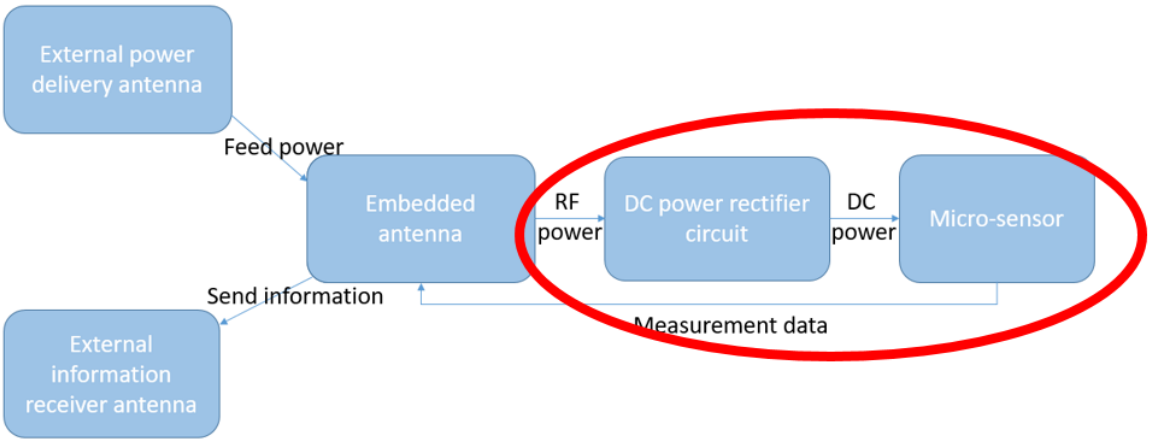

Figure 4.1 Simplified wireless power system operation (circled)

4.2 Circuit design

4.2.1 Rectifying circuit comparison

There are many types of rectifying circuits which could convert high frequency RF power into DC power. A rectifying circuit usually consists of three parts: Impedance matching part, current rectifying part and power stabilizing part. In order to minimize the loss, the number of elements in use should be minimized.

4.2.1.1 Circuit structure

In general, a one-diode rectifying circuit or a voltage doubler could be functional. But each circuit has its own advantages. The one-diode circuit could only rectify half of the waveform power but it has low losses because of the diode. The voltage doubler could rectify the currents from either flowing direction but it could be more lossy with

the presence of one diode at a time. Therefore, the choice should be made by comparing the two circuits.

The choice of diodes is important, as diodes are the core of the entire circuit. The performance of the diodes mainly determines the performance of the circuit. From the literature, it appears that HSMS 2850 diodes are frequently used in previous researches and Skyworks 7630 was used recently as a new choice [81] [82]. For determining the circuit structure, we choose HSMS 2850 as an example as its model already exists in the ADS library.

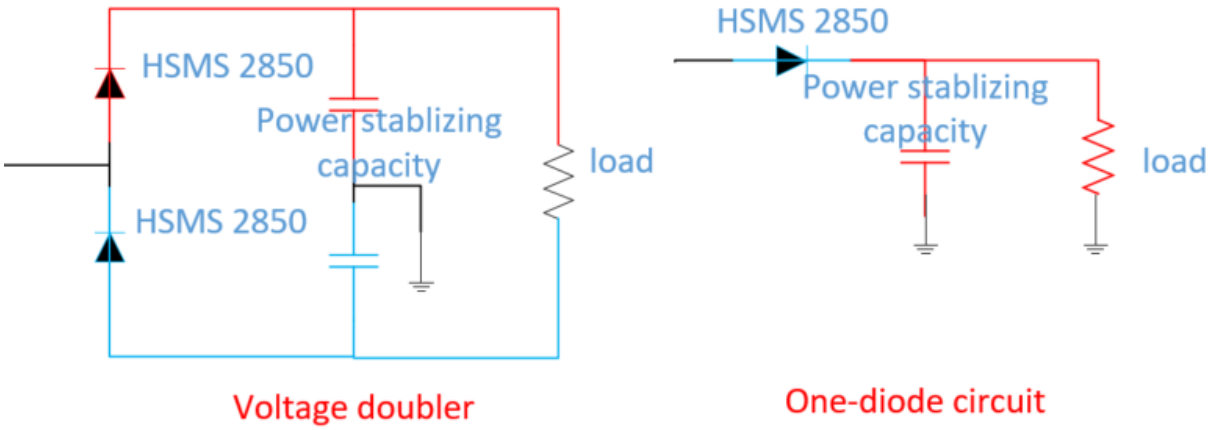

Figure 4.2 Two different kinds of rectifying circuit

Figure 4.2 shows the structure of the two different kinds of rectifying circuit. For simplicity, the Figure only shows the circuit after the impedance matching part. The working states for each half periods are marked in red and blue color (positive and negative current). As shown in Figure 4.2, the voltage doubler uses the two diodes alternatively (one at a time) while the one-diode circuit uses it only half time. However, the voltage doubler can rectify the current in both directions. Adding a low loss well performing diode should increase the total efficiency. It could thus minimize the disadvantage of the voltage doubler. The doubler is chosen.

4.2.1.2 Impedance matching

In order to reduce the mismatch loss between the feeding port and the rectifying circuit, the impedance matching circuit is necessary. It helps the circuit to change its own impedance to match that of the feeding port (the embedded antenna in our case). In previous chapter, it is obtained with simulations that the antenna's impedance is close to 80 Ω at its resonant frequency (915 MHz). Therefore, the impedance of the circuit should be measured under the operating frequency (915 MHz) and then the matching circuit is calculated according to the results to match.

In order to fulfill the "minimization of the number of elements" request, a configuration with only two or three components circuit is considered. Figure 4.3 shows

the types of components and their calculated values for the impedance matching circuit. Having only 2 components could reduce the power dissipated to these components, while 3 components could match the impedance more accurately.

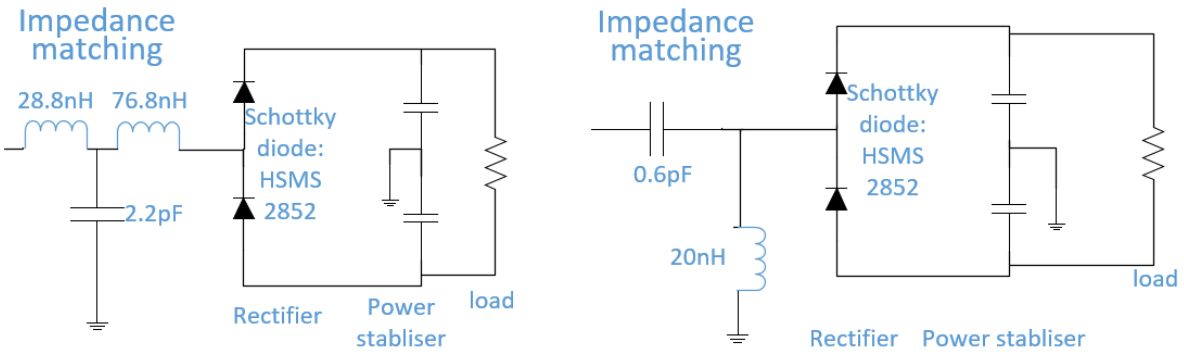

Figure 4.3 Three-component and two-component impedance matching circuit

4.2.2 Combination design

This rectifying circuit is used for rectifying the power received by the embedded antenna (see Figure 3.7). For the patient's comfort, the entire system (antenna + circuit) should occupy the least possible space inside the human body. Furthermore, according to the radiation microstrip circuit of the antenna in chapter 2, the main lobe of the antenna is towards its lateral side. Therefore, one possible solution for the circuit positioning is adding another layer to the antenna (above the superstrate or below the substrate). Two solutions are thus proposed in this chapter corresponding to the antenna's design. The designs are shown in Figure 4.4.

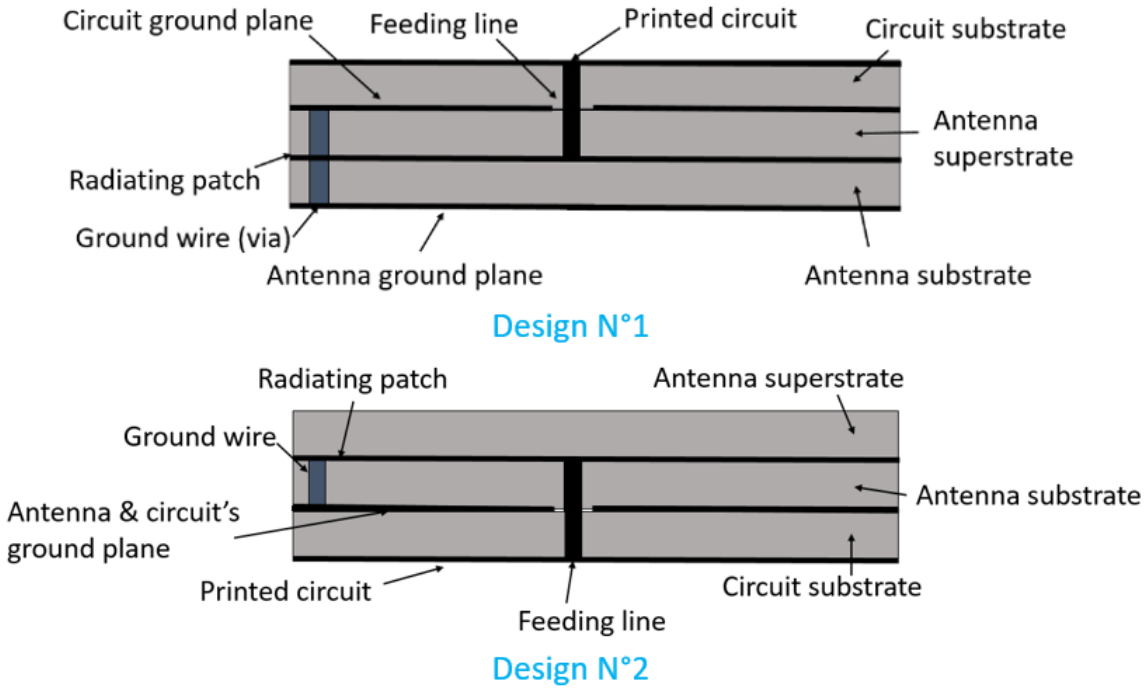

Figure 4.4 Two different antenna-circuit combination designs

In the two designs, the circuit is stuck to the antenna's top or bottom side. In the first design, the feeding line penetrates the antenna's superstrate and the circuit's substrate in order to connect the feeding point of the circuit and that of the antenna. The via which penetrates the superstrate and the substrate connects the antenna's ground point, the circuit's and the antenna's ground plane altogether. In the second design, the printed circuit is placed at the bottom side of the antenna in order to connect the two ground planes without any electrical via. The feeding line also penetrates the circuit substrate. However, for both designs, the feeding line should be isolated from the ground plane (either antenna's or circuit's), otherwise the circuit is shorted immediately.

Both designs are feasible. Nevertheless, the second design has one less via to drill comparing to the first design. Due to this fabrication simplicity, the second design is thus chosen.

4.2.3 Printed microstrip circuit design

As discussed in the previous section, the shape of the printed circuit is determined: It has to fit in the circular substrate of the same size as the antenna. However, due to this tiny size of the circuit printed microstrip circuit and small values of the components, the parasitic capacity of the circuit is no longer negligible. It is thus important to also anticipate the parasitic effect of the circuit in order to match more accurately the impedance with the input port.

Also, for different quantity of components, the printed microstrip circuit could be different and calculations should be performed for each of the cases.

For fabrication simplicity, components of 0603 (1.6 mm x 0.8 mm) package are used and SOT-23 package is used for the diodes. Also, for bio-friendly reasons, the circuit's substrate still uses the Rogers RO3210 (introduced in chapter 2) and the metal cladding is copper.

As non-linear components, the diodes might have impacts on other electronic components during high frequency operations, they are thus positioned in the corner and relatively far away from other inductors.

The two kinds of circuits which are suitable for two-component and three-component impedance matching circuits are presented in Figure 4.5 below:

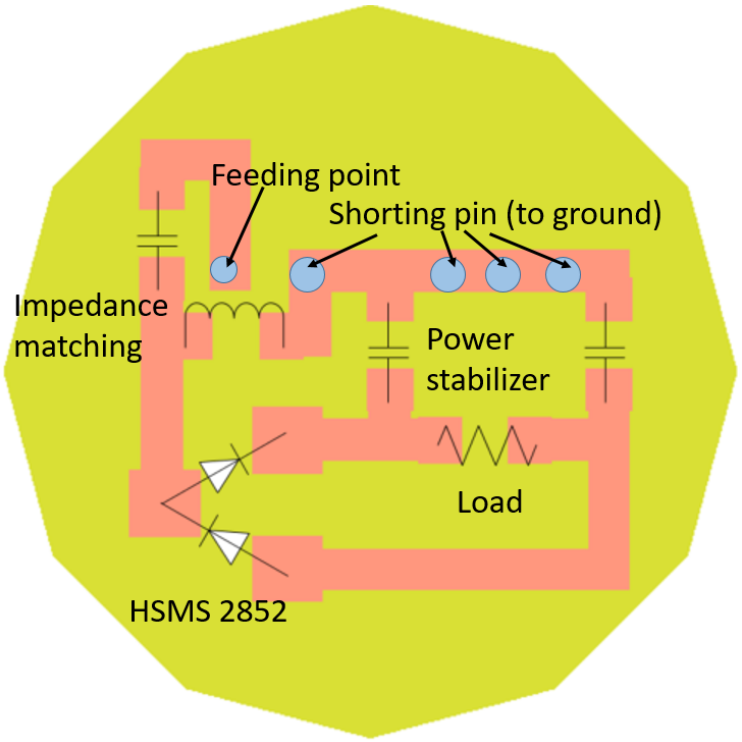

[a]

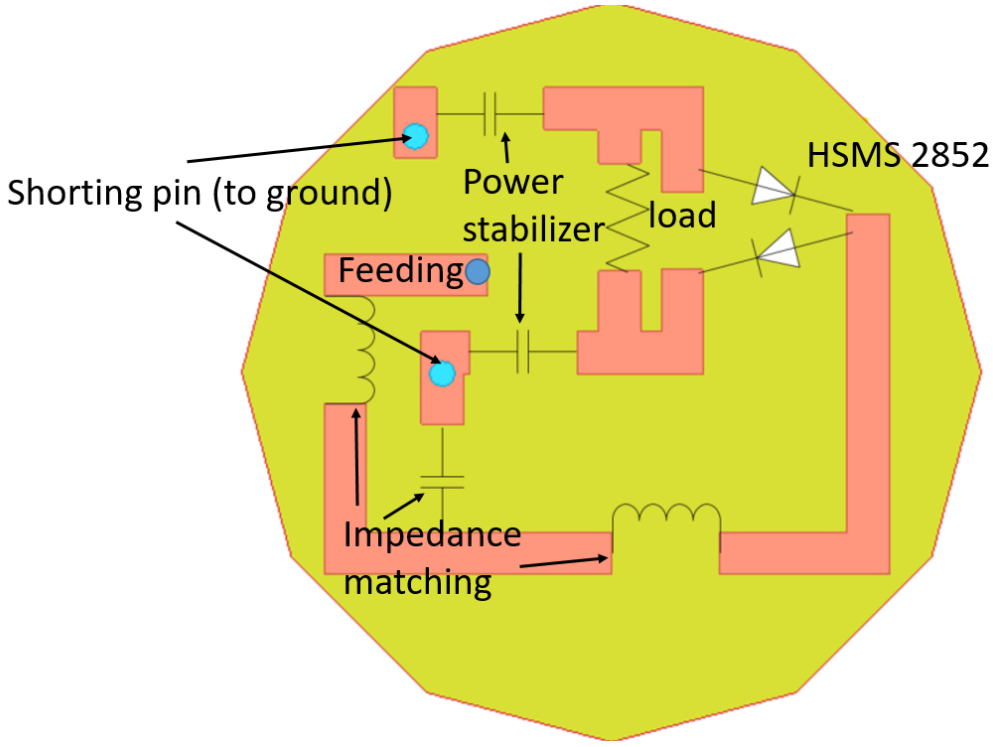

[b]

Figure 4.5 Printed microstrip line circuit (copper track) [a] Two-component (L-matching) [b] Three-component (T-matching)

As seen in the two Figures, the feeding point position is always the same since it must perfectly coincide with the antenna's feeding point's position. Although many corners may add instability to the circuit, the space constraint leaves no choice for it. The current flows in from the feeding point then passes the impedance matching part, then the diodes, and finally charges the power stabilizer capacitors and feeds the load.

4.3 Numerical results

In this section, numerical results that are based on ADS simulations are presented. The rectifying efficiency and output voltage (at load) for different input power levels are usually the given results. The rectifying efficiency is the ratio between the power consumed by the load and the power provided by the power source. Because of reflection, the power provided by the source is slightly higher than the power consumed by the whole circuit.

Due to the existence of the non-linear components, there is a non-superposition between the current and the voltage. Thus, input power (see Figure 4.6) is calculated by:

$$P_{active} = Re[\mathrm{U} \cdot I^{*})] \tag{4-1}$$

where U and I are the voltage and the current in phasor form (the first harmonic approximation is used here). However, since the voltage between the load is DC, the power at the load is calculated by:

$$P_{load} = U_{load} \cdot I_{load} \tag{4-2}$$

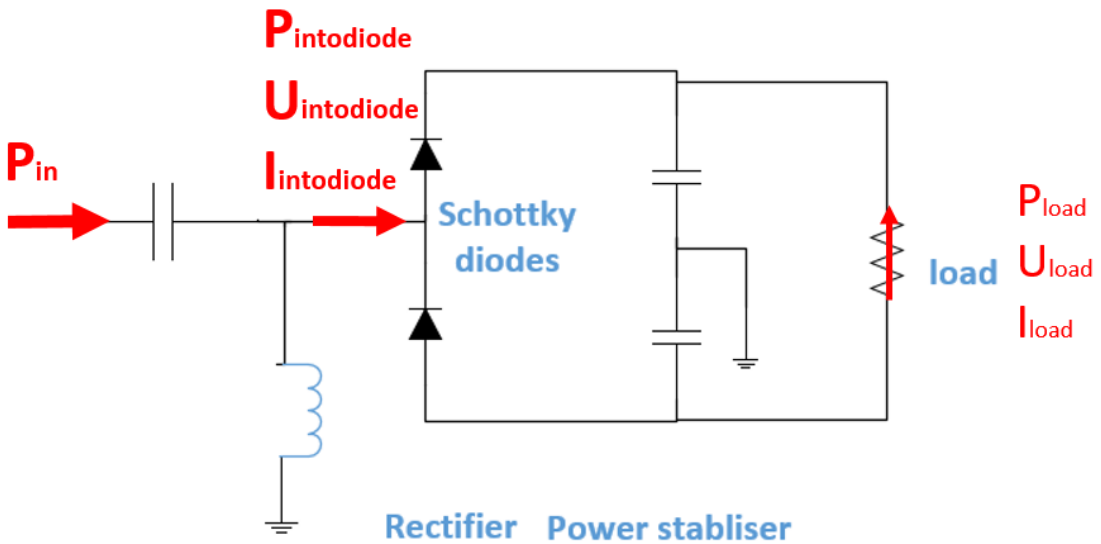

$$P_{Intodiode} = Re[U_{intodiode} \cdot conj(I_{intodiode})]$$

$$P_{load} = U_{intodiode} \cdot I_{intodiode}$$

Figure 4.6 Power calculation with different components

The average input power of the circuit is estimated from -5 dBm to -20 dBm for different transmission conditions (see S_{21} results in chapter 3, S_{21} varies from -35 dB to -50 dB under different conditions). According to the calculations in section 3.2, with an global input power of 30 dBm, the input power for the circuit is estimated as -20 dBm. Therefore, in this section, -20 dBm is taken as an example for the circuit's virtual input power.

4.3.1 Off-the-shelf components

In previous sections, the components are ideal components whose electrical values do not vary or vibrate according to operation frequencies. However, in real uses, the real value might be different from the ideal values, for example, inductors at high frequencies. In fact, the real values of non-linear elements (capacitors, inductors, diodes, etc) are all dependent on the operating frequencies.

Furthermore, for capacitors and inductors, only certain values are available. When the exact value components do not exist, the possible values nearby should be well analyzed and chosen. It is noted in the datasheet that inductor values may be higher than the marked value at high frequency (we take the inductor that we used in measurements as an example, see Figure 4.7 below [83]). We can clearly observe that the inductance value increases slightly at 915 MHz. Thus, the value chosen should usually be smaller than the calculated values in order to compensate for this change.

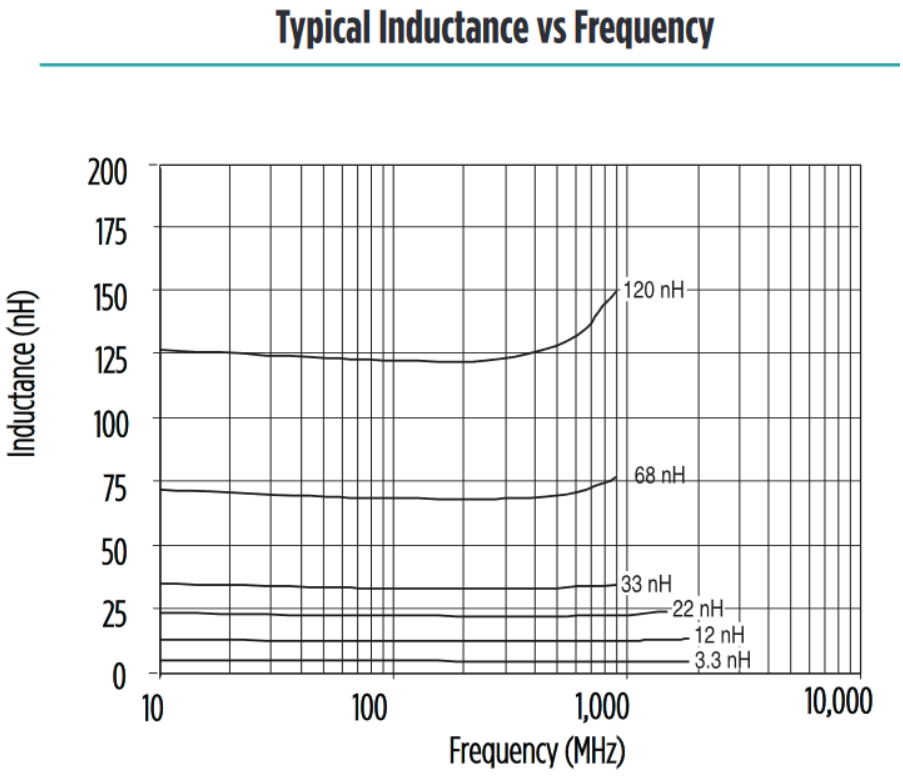

Figure 4.7 Inductance vs frequency [83]

Fortunately, there are some numerical models in the ADS library which consists of a series of ideal components. These models could be equivalent to the off-the-shelf components and thus could be used in simulations. In ADS library, components of package 0603 (1608) from Murata company are already modeled and ready for use in simulations.

While replacing the ideal components with the off-the-shelf ones, the two capacitors which act as the voltage stabilizer are the ones to be started with. These capacitors' values should be chosen properly. High values would increase the charging time of the capacitor and low values would increase the oscillation. The diodes are the next step. Once their values are fixed, the impedance matching part is left to be determined. Let us take a two-component circuit for an example. The comparison results are shown in Figure 4.8 and Figure 4.9.

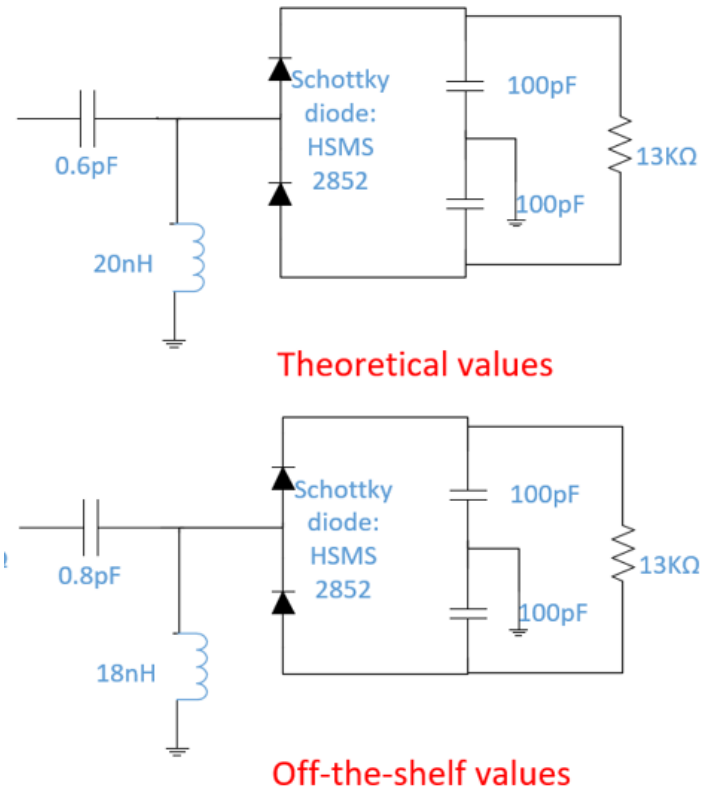

Figure 4.8 Circuit values comparison

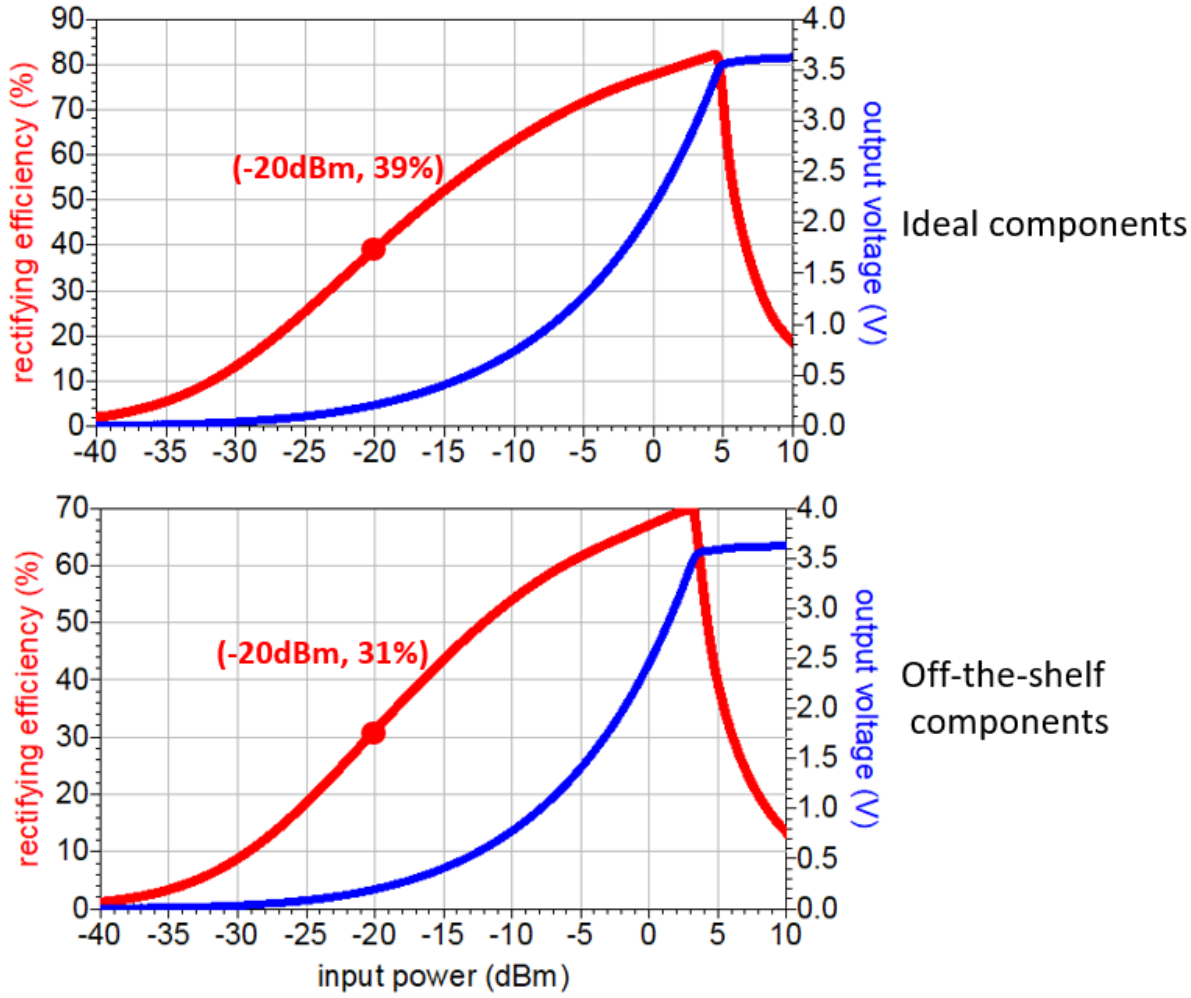

Figure 4.9 Comparison of the circuit with ideal components and off-the-shelf components

As we could see in the two figures 4.8 and 4.9, the optimized values of the components change when the ideal components are replaced by the off-the-shelf ones. This is because, for real uses, the exact value of the components may change under different frequencies. Also, certain components may be affected by other components and the printed lossy transmission line and they can also add some parasitic capacity.

For -20 dBm power input, the rectifying efficiency of the circuit decreases by around 10% with off-the-shelf components. This is a huge difference and thus proves the necessity of the replacement.

4.3.2 Components number comparison

In the last section 4.2, we have compared the two-component impedance matching circuit with the three-component one and discussed their differences. Here another more realistic comparison is done with all off-the-shelf components. The circuit's values are shown in Figure 4.10 and the results are shown in Figure 4.11.

As shown in Figure 4.11, when the impedance matching circuit switches from two components to three-components, the total rectifying efficiency reduces from 31% to 23% and the output voltage decreases from 0.2 V to 0.17 V. As a result, the two-component circuit has better performance than the three-component circuit and thus is chosen.

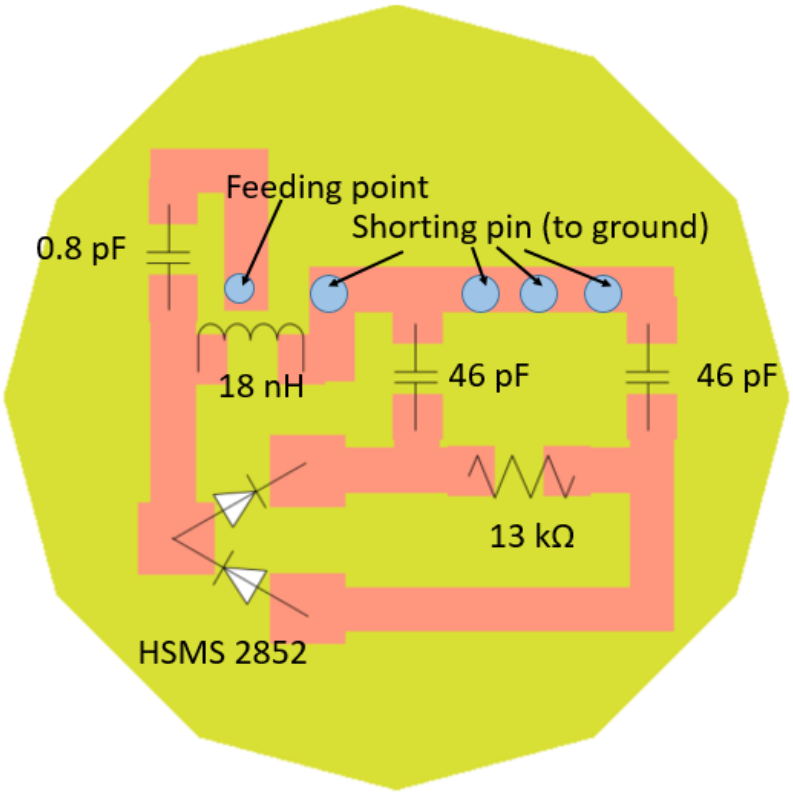

Figure 4.10 Two-component circuit with its optimized values (off-the-shelf components)

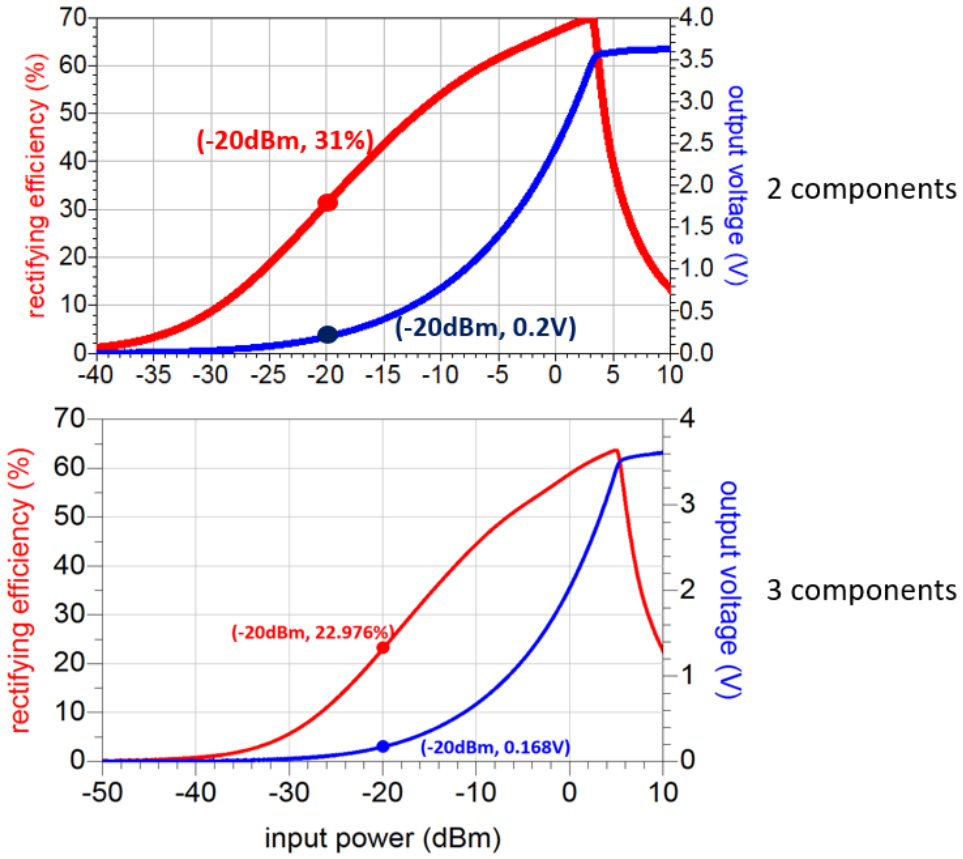

Figure 4.11 Comparison of the circuit with two-component or three-component impedance matching section (with the most optimized load value)

4.3.3 Load optimization

Resistive load, as a replacement for the real power-consuming component, has also impacts on the rectifying circuit. Although we cannot control the resistance value of the load, it is still interesting to quantify the impact of the load on the rectifying efficiency and output voltage. Figure 4.12 shows the efficiency and output voltage as a function of different loads with -20 dBm power input.

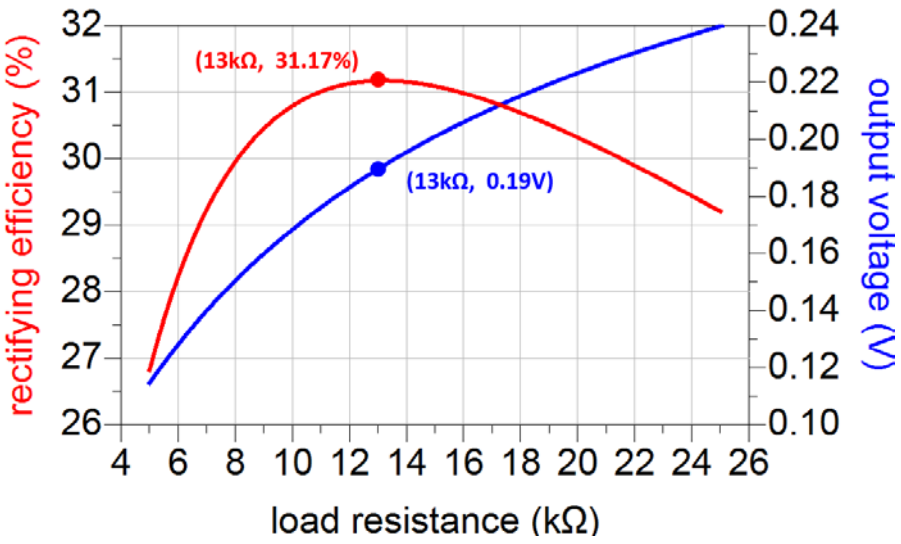

Figure 4.12 Efficiency and output voltage for different load resistance

As shown in Figure 4.12, the rectifying efficiency reaches a local peak value when the load is 13 KΩ. For realistic uses, this might be a criterion for choosing the compatible sensor. As the load increases, the power at the load decreases but the output voltage increases continuously, which might be used as a voltage trigger (obtaining an instantaneous high voltage at 0.3 V for example)

4.3.4 Diode comparison

As the key components of the rectifying circuit, diodes have significant impacts on the circuit. A well-performing diode could decrease the circuit's loss and could also allow the existence of two diodes without worrying too much about loss.

Apart from traditional high frequency (HF) diode HSMS, Skyworks company has also commercialized an HF model Skyworks SMS7630. A comparison between the 2 diodes is thus necessary in order to optimize the circuit.

In order to perform the simulation, the model of the diode must be established first since it is a recent component and does not exist in the ADS library. In Figure 4.13, the SPICE parameters of the diode are shown from which a diode model could be built in the Pspice [84], which is a free software for academic uses.

Table 5. SPICE Model Parameters (Per Junction)

Parameter	Units	SMS1546 Series	SMS7621 Series	SMS7630 Series
I_S	A	3E-7	4E-8	5E-6
R_S	Ω	4	12	20
N	–	1.04	1.05	1.05
TT	sec	1E-11	1E-11	1E-11
C_{JO}	pF	0.38	0.1	0.14
M	–	0.36	0.35	0.40
E_G	eV	0.69	0.69	0.69
XTI	–	2	2	2
F_C	–	0.5	0.5	0.5
B_V	V	3	3	2
I_{BV}	A	1E-5	1E-5	1E-4
V_J	V	0.51	0.51	0.34

Figure 4.13 SPICE model parameters of the diode

After having created the SPICE model of the diode, in order to be more accurate in simulations and closer to reality, the model package should also be considered in order to complete the diode model. After looking into the technical document, skyworks SMS7630 uses SOT-23 package, whose model is shown in Figure 4.14 as below:

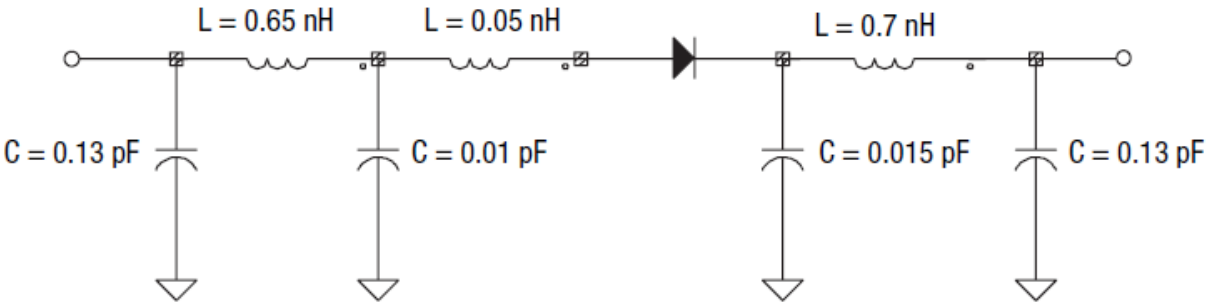

Figure 4.14 SOT-23 package model

Since this SOT-23 package model is applied for one single diode, the package model should be added for each diode used in the circuit.

Now with the complete model of both diodes, the performance of these two diodes should be examined and compared in the same circuit. The values of the impedance matching section are set to the most optimized value and the input power is fixed at -20 dBm. The efficiency and output voltage are always the main criteria for this comparison.

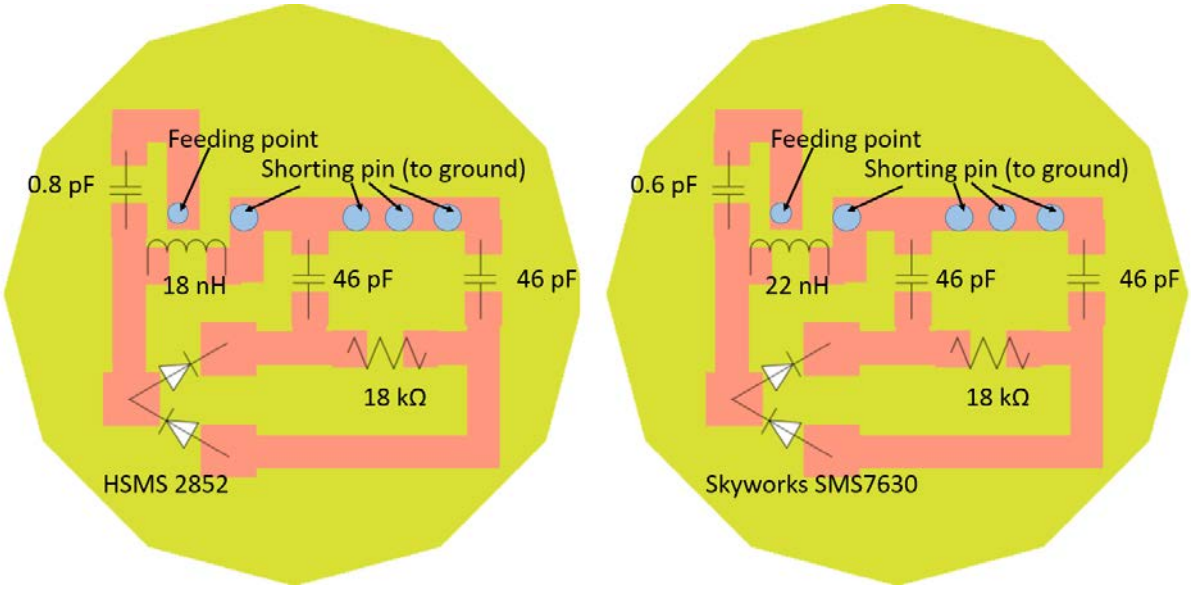

Figure 4.15 Rectifying circuit with HSMS 2852 and skyworks SMS7630 diodes

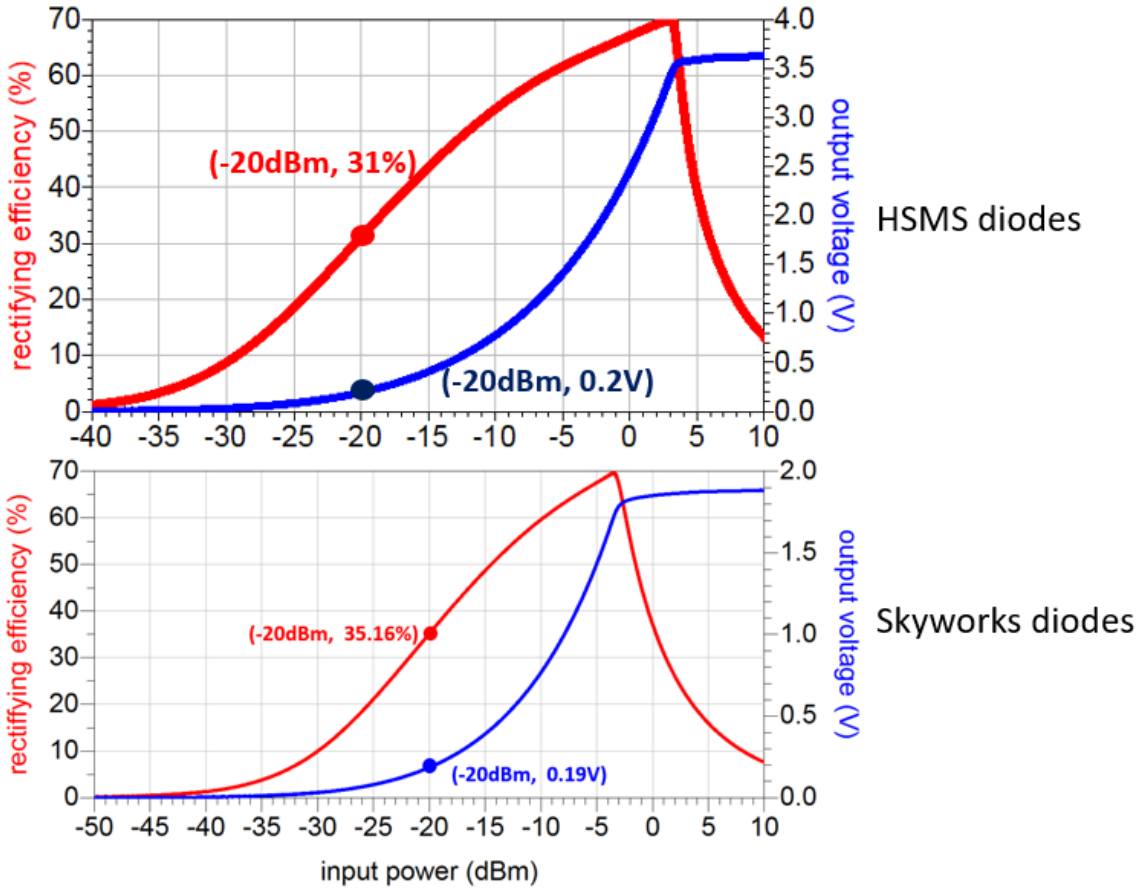

Figure 4.16 Results comparison between HSMS and Skyworks diodes

As shown in the comparison Figure 4.16, the rectifying efficiency of the circuit increases by 4% when the HSMS diodes are replaced by Skyworks diodes. The output voltage does not have significant change but still, HSMS diodes have higher output voltages. Therefore, it is suggested that for uses that do not require high voltages,

Skyworks diodes should be more capable; if there is any requirement for output voltage that Skyworks diodes cannot fulfill, HSMS diodes could be an alternative choice.

4.3.5 Antenna-circuit combination analysis

Last but not least, we should integrate the antenna model into the circuit model in order to simulate a more realistic case. The circuit simulation is based on the electromagnetic modeling of the circuit and components available in ADS library. Since the co-simulation between ADS and CST is not feasible, it is possible to integrate the antenna as an S-parameter block which could also represent all characteristics of the antenna for this kind of use. As mentioned in chapter 3, the maximum allowable fed power to an antenna at 915 MHz band is 30 dBm.

Simulation results for the global rectenna system are shown in Figures 4.17 and 4.18, in which the relationship between the rectifying efficiency, output voltage, and input power into the external antenna is presented for various transmission distances. In this simulation, mismatch losses between antenna and circuit are also taken into account. As mentioned in chapter 2, the impedance of the antenna at 915 MHz is around 80 Ω. Since the antenna is directly connected with the circuit (no more coaxial cable), the circuit should be matched directly with the antenna.

It is worth mentioning that in this section, the X-axis --input power is the input power for the rectenna (antenna + circuit). In the previous sections, all input power values were considered only for the feeding of the circuit.

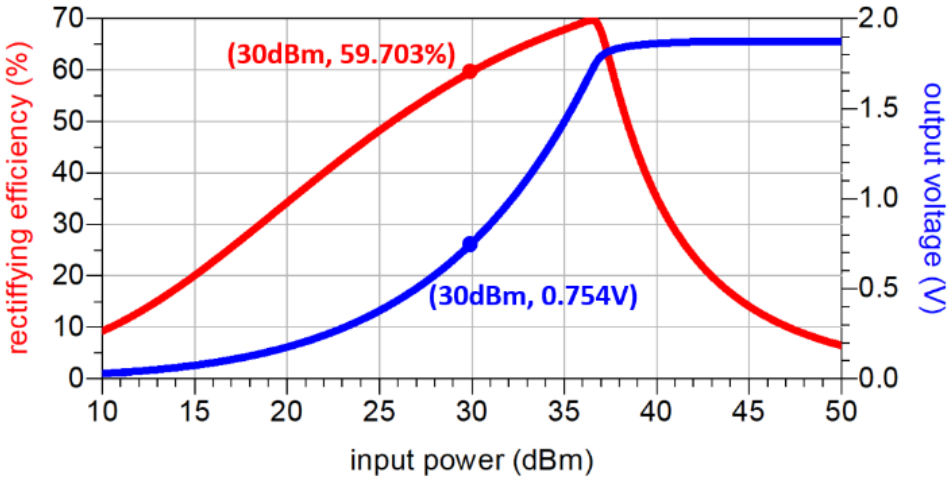

Figure 4.17. Global system efficiency and output voltage when the external patch is at 400 mm distance (rectifying efficiency = 59.7%, output voltage = 0.75 V with 30 dBm input power at the patch and for 10 kΩ load)

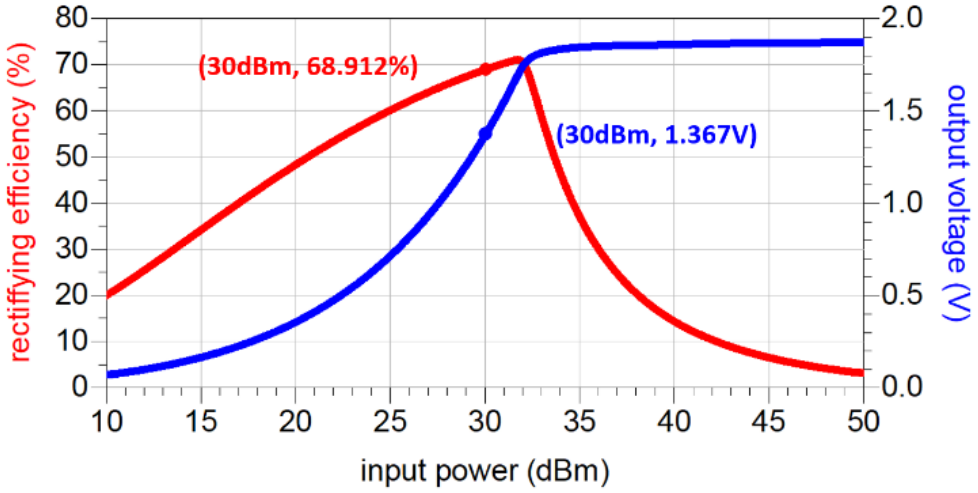

Figure 4.18. Global system efficiency and output voltage when the external patch is at 200 mm distance (rectifying efficiency = 68.9%, output voltage = 1.37 V with 30 dBm input power at the patch and for 8 kΩ load)

As we can see in Figures 4.17 and 4.18, the rectenna system has better performance when the transmission antenna is close to the receiver antenna. This is because when the two antennas are nearby, the transmission efficiency is increased. The receiver antenna gets more power, which increases again the rectifying efficiency. Therefore, any condition that could increase the power transmission efficiency of the antenna may lead to a large improvement in the rectenna's rectifying efficiency and output power. Both two load values are the most optimized values in each situation.

When the external patch antenna is fed by 30 dBm power and radiates from 400mm away (transmission distance), the efficiency of the circuit is 59.7%. The value of the load 10 kΩ is chosen in order to maximize the power transmission efficiency. The DC voltage at the load is 0.75 V and the power consumed by the load is 56.9 μW at this distance.

When the patch antenna is only 200 mm away (transmission distance) from the patch, the rectifying efficiency of the circuit is increased to 68.9% due to the increase of the power received by the implanted antenna. The output voltage at load is 1.37 V and the final rectified DC power is 233.6 μW.

4.4 Advanced Design System™ settings

Advanced Design System (ADS) is an electronic design automation software system produced by Keysight EEsof EDA, a division of Keysight Technologies. It provides an integrated design environment to designers of RF electronic products and thus is used during this design procedure of the rectifying circuit.

4.4.1 Circuit layout setup

It has been discussed in the previous sections that the electromagnetic characteristics of the entire circuit (together with circuit model) should be considered as well since all the components are of tiny values and they are more sensitive to parasitic capacities or any other perturbations.

For the circuit design, first of all, the circuit must be printed on a bio-friendly material in order to be embedded inside the human body together with the antenna. As we mentioned before, the Rogers RO3210 has close dielectric properties to Alumina which is bio-friendly. Here we choose the same substrate as that of the antenna for simplicity.

The materials of the substrate and the transmission lines tracks should be set up in the ***EM – Susbtrate***. The thickness, material, and global structure are all defined in this window.

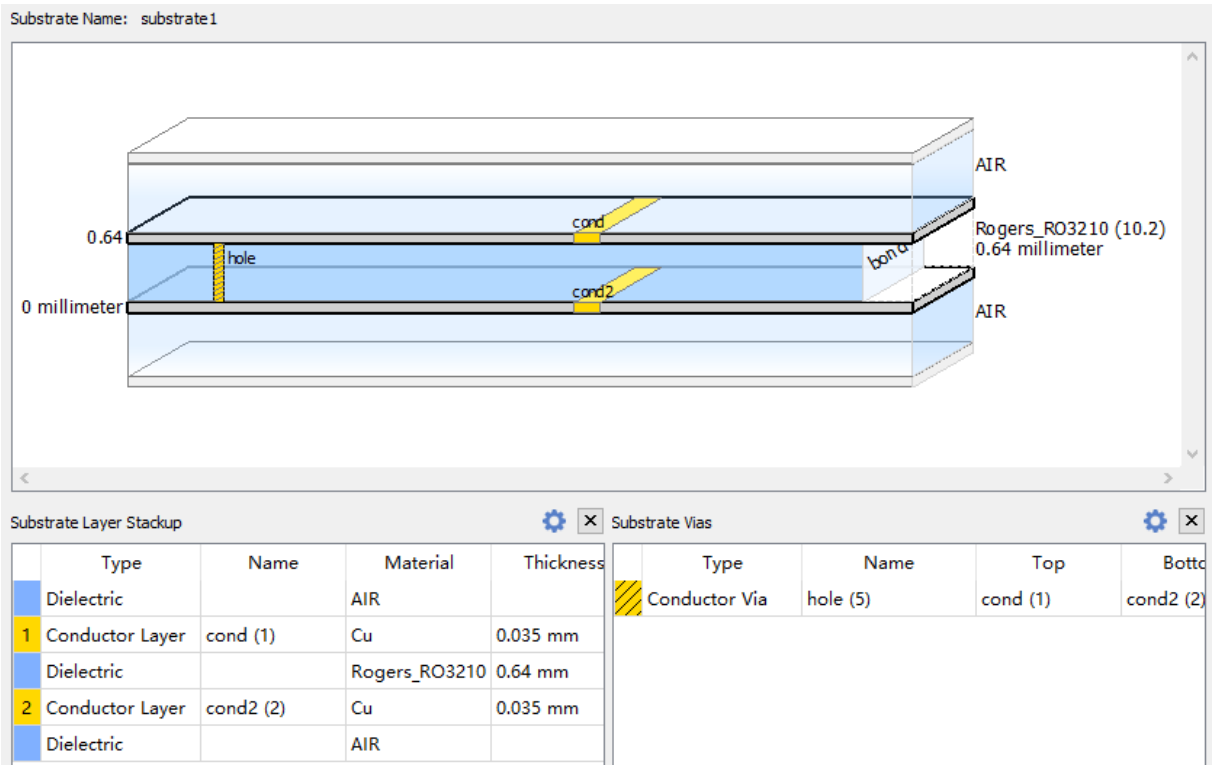

	Type	Name	Material	Thickness
	Dielectric		AIR	
1	Conductor Layer	cond (1)	Cu	0.035 mm
	Dielectric		Rogers_RO3210	0.64 mm
2	Conductor Layer	cond2 (2)	Cu	0.035 mm
	Dielectric		AIR	

Type	Name	Top	Bottc
Conductor Via	hole (5)	cond (1)	cond2 (2)

Figure 4.19 Circuit structure setup

The two "cond" represent the circuit transmission line and a hole with an electrical via represent the rest metal conductor. Three "Dielectric" represent the material with which the metal conductors have contact.

After the substrate setup, we need to draw the circuit transmission line. As calculated in chapter 2 the impedance of the antenna at 915 MHz is close to 50 Ω. According to a microstrip calculator [85], the width of the microstrip should be 0.6mm in order to minimize the mismatch loss. Also, the size of all the packages (especially of their feet)

(0603 and SOT-23) that are used in this design should be noted. The design to pring is drawn in Figure 4.20.

There are in total 4 layers in this design: The two metallic conductors (layer: *cond* and *cond2*), the dielectric (layer: *bond*), and the holes with via (layer: *holes*).

In the "cond" layer, which has all the main microstrip circuit, a port should be placed at each location where there is a connection in order to connect the electronic components later in the simulations. In the port Editor, the relationship of all the ports should be correctly defined.

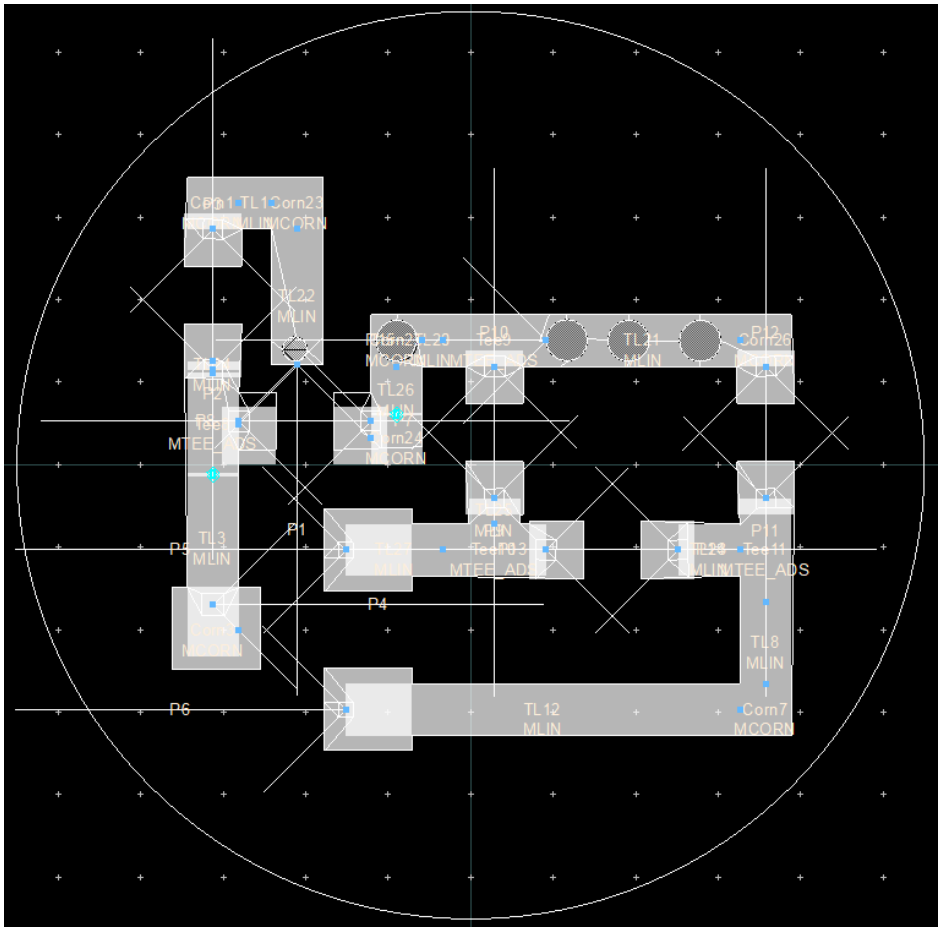

Figure 4.20 Circuit layout draft

After the design procedures, the model should be created by performing the "***EM-simulate***". Then in the "*EM-3D EM Preview- With EM Setup Preprocessing*" should be carefully checked before in use. The correct example is shown in Figure 4.21.

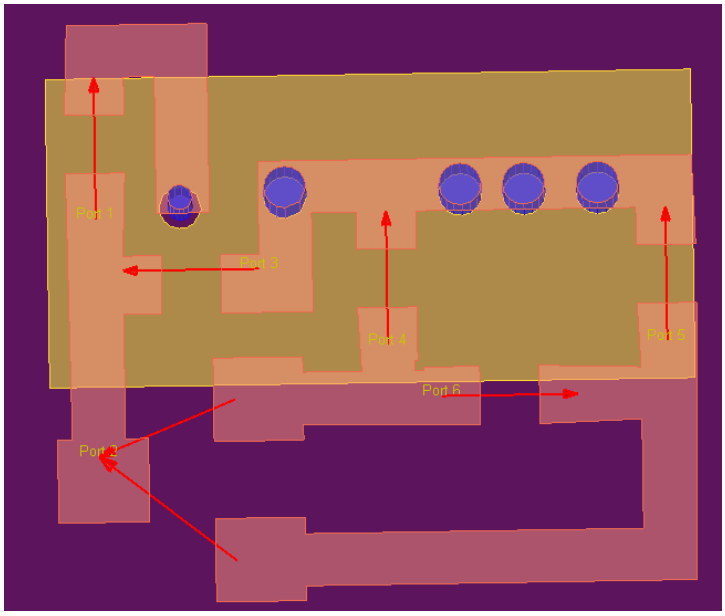

Figure 4.21 Correct example of the circuit layout model

In this example, it is clear that each port has a corresponding component which is to be connected afterward.

Finally, when it is to be used, it just needs to drag the "*symbol*" directly into the new "*schematic*" page and use it as a common component.

4.5 Sensor analysis

Various micro-sensor grids for biomedical uses are studied and developed in recent years. These sensors need low power and have small sizes in order to be suitable for implanting uses. In Table 4.1, several sensors together with their feeding power, supply voltage, area of circuit and Effective Number of Bits (ENOB) are presented.

Table 4.1 Low cost sensors and specific parameters

Ref	Average power consumption (μW)	Supply Voltage (V)	Area (mm^2)	ENOB (bit)
[24]	5.5	0.5	375	8.02
[86]	0.27	0.3	0.07	6.1
[87]	6.9	3	9.28	8
[88]	10.5	1.8	0.25	13
[89]	1.5	1	2.25	12

The sensors in the table require low energy and voltage to operate. They also occupy little space which is suitable for implanted uses together with the power transmission

system in this paper. These sensors require continuous power during data measuring. They operate only while the implant is being charged, therefore no store device is needed. In order to match the two parts together, it is necessary to calculate the actual power received by the load.

From the previous calculation, the power that a single power transmission system in this paper could receive for different transmission distances is shown in Table 4.2. An implantation depth of 16 mm is taken as an example here.

Table 4.2 Received power at different distances

Transmission distance (mm)	S_{21}@ 915 MHz	Circuit efficiency (%)	Power @ load (μW)	Power for information exchange (μW)	Max external patch distance for information exchange (mm)
200	-36.1	68.9	233.4	23.3	1300
400	-40.4	59.7	56.9	5.7	850
500	-42.4	54.5	28.9	2.9	600

As shown in Table 4.2, the power transmission system is capable of feeding several sensors in terms of power. The results are calculated by simulations. They are based on the power received by the implanted antenna with the corresponding distance value and the rectifying efficiency & output voltage results with the corresponding power received. In both simulations, the port impedances are standardized to 110 Ω and it is assumed that only 10% of the rectified power is used for powering the information exchange and that all ports are perfectly matched.

As calculated, there is always a corresponding maximum distance between the reception dipole and the skin surface in order to ensure the connection (energy received by the reception dipole ≥ -90dBm [90] which is the minimum power that can be received by mobile phones without information loss) for every different implantation depth.

For the values in Table 4.2, the input power of the rectifying circuit is not -20 dBm. This power varies with transmission distances. However, due to maximum allowable power emission standards, the power emitted by the external antenna must not be higher than 30 dBm. Therefore, in all the results presented in Table 4.2, the power emitted by the external antenna is fixed at the maximum value 30 dBm. The value of power received in Table 4.2 shows that this could support any one of the sensors mentioned in Table 4.1. However, a voltage booster might still be needed to achieve the supply voltage of the sensors and will be tested in the future.

4.6 Conclusion

This chapter introduces mainly the design procedures and results of the rectifying circuit. It firstly presents the reason why choosing the voltage doubler. Then the antenna-circuit combining methods for fabrication are discussed and compared. After that, we use several comparisons to find the most optimized design step by step. A two-component impedance matching circuit using 0603 package components is chosen Some possible difficulties in simulation setup are discussed and presented afterward. Finally, some existing sensors are introduced and it is proved by simulations that this system could support the feeding of several kinds of sensors in terms of received power. Through antenna-circuit combination analysis, with the most optimized configuration, the entire system is able to receive 56.9 μW for 400 mm power transmission distance and 233.4 μW for 200 mm power transmission distance.

The scenario of the wireless power transmission system is here completed and the usability of the system is proved. Measurements follow.

Chapter 5

Measurements and experimental procedures

5.1 Introduction

Experimental measurements are always the best way to prove the feasibility and the proof-worthy of the theoretical researches. In this chapter, all the experimental procedures of the previous simulations are introduced, including the receiving antenna and the rectifying circuit. For the receiving antenna, it was embedded into a "human-like" environment and several useful results were obtained.

In this chapter, we will first introduce all the equipment that is used during the measurements and then the different results obtained by different experiments.

5.2 Antenna measurements

5.2.1 Preparations

In order to accomplish the measurements, there are several fundamental devices that are necessary for the experiment.

5.2.1.1 Vector network analyzer

Vector network analyzer, known as VNA, is the most essential equipment during the measurement procedure. Different from a scalar network analyzer, it measures not only the amplitude properties but also the phase properties of the signal. With VNA, we could easily measure the S-parameters of the antenna with simple buttons.

Figure 5.1 shows the VNA that is used during the measurement in GeePs. Although different VNAs have different structures, the main functions and utilization procedures remain the same. In the anechoic chamber in GeePs, Agilent E8363b (see Figure 5.1) from Keysight company is employed. This VNA could operate from 10 MHz to 40 GHz with minimum of 10 Hz accuracy.

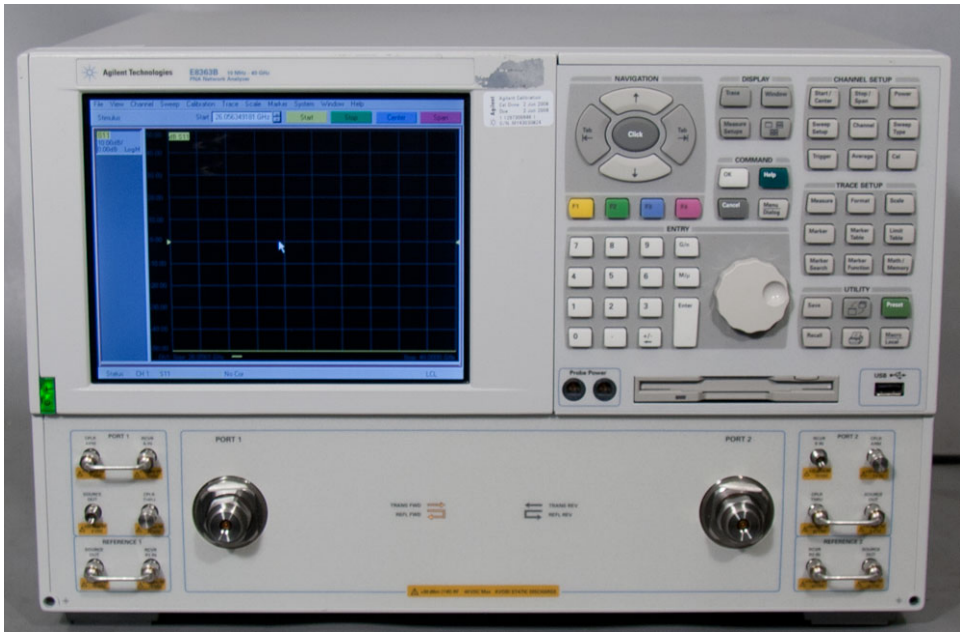

Figure 5.1 Agilent E8363b Network Analyzer

With each VNA, in order to ensure the result's accuracy, has to be calibrated at the feeding point of the antenna. Figure 5.2 shows the standard calibration kit for this kind of VNA.

Figure 5.2 Calibration kit of the VNA

For the calibration, three different connection modes are to be standardized: Open circuit, short circuit, and a preset value (usually 50 Ω, depends on the port impedance). For each connection, a male and a female connection are provided in the case of different cables. The calibration kits should be well connected to the end of the cable and should be placed on a stable surface to avoid perturbation.

According to the formula in chapter 2 (see Figure 2.11), the reflection coefficient S_{11} is defined as:

$$S_{11} = \frac{Z_{in} - Z_0}{Z_{in} + Z_0} \tag{5-1}$$

Z_{in} is the input impedance and Z_0 is the port impedance.

Let's take a 50Ω port as an example. When the circuit is connected to "open", S_{11} = 1; when the circuit is connected to "short", S_{11} = -1; and when the circuit is connected to "50 Ω", S_{11} = 0. These are the two limit and the middle values of the S_{11}.

For the uses where both two ports are needed, a transmission calibration kit is also necessary. A male-male, male-female and female-female connectors are available for this calibration.

5.2.1.2 RF coaxial cable

In order to connect the antenna with the VNA, we need a series of connection cables. As we mentioned in the previous section, the calibration should be done at the feeding point of the antenna in order to eliminate the impact of the cable on the measurements. However, a simple antenna without any connector could not be connected directly to the cable. Therefore, a connector is needed in this case (see Figure 5.3).

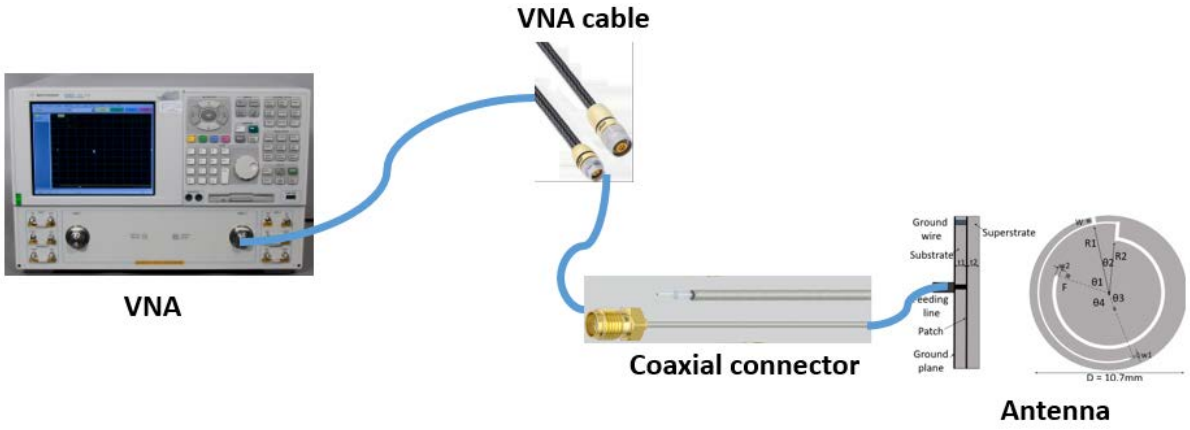

Figure 5.3 Connection structure for the measurements

The RF coaxial connector is a specially made connector that is designed to be used in miniaturized cases. It is thin and thus has fewer perturbations comparing to thick connectors. The connector is chosen as the PE3CA1103-3 from Pasternack company. Regardless of its tiny size, due to the high sensitivity of the measurements, it should still be included in the calibration in order to ensure accuracy.

The RF coaxial connector has three layers: Outer metal, dielectric and inner metal. The dielectric ensures the wave propagation between the two metallic wires with the minimization of loss. The structure is shown in Figure 5.4.

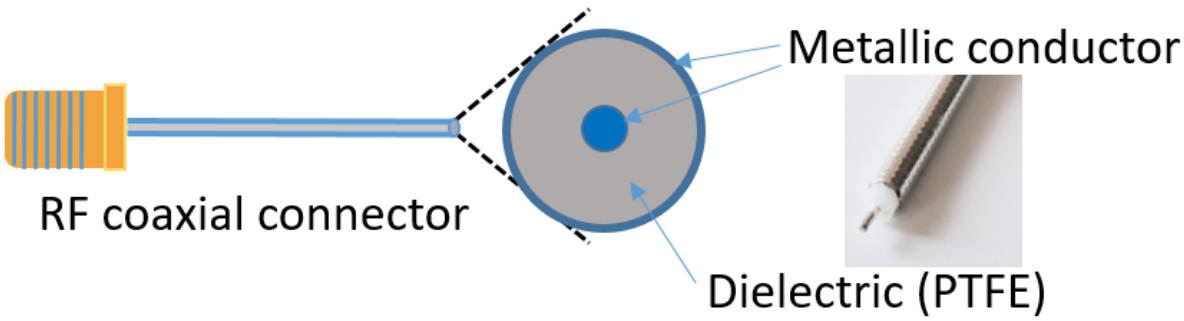

Figure 5.4 RF coaxial connector structure

For the PE3CA1103-3 cable, the inner solid metal is made of silver and the outer metal is copper. The dielectric is PTFE (Teflon, ε_r=2.1, tanδ=0.0002). The operation frequency is 0 to 6 GHz. The diameter of the inner metal is 0.3 mm.

5.2.2 Antenna fabrication

For the fabrication of the antenna, two fabrication methods are usually in use: The laser method and the mechanical method.

The laser etching is a modern method for the fabrication of printed antennas: We use a laser to remove the preset amount of material on the surface of the object in order to form and shape it. Also, we could realize the cutting and drilling by using a more powerful laser beam. However, the precondition of using a laser is for the material is to be heatproof, otherwise, it is likely that the material is burnt during the fabrication process. In our case, the Rogers RO3210 material has woven glass reinforcement [91] and thus it could resist the temporary heat. Also, the copper layer covering RO3210 is 17 μm thick and is suitable for the laser machine in our laboratory (the thicker the layer, the more difficult it is for the laser to cut it).

For the laser machine, the key factor is the number of passes it performs, the power of the laser, and processing speed. For a soft material, the procedure should be carried out with low power laser but with more passes in order not to burn the materials and to control the surface temperature. The number of passes should be obtained by exercising on the material and the most optimized parameters should be found out and noted. Also, the material should be well fixed in the machine in order to be shaped precisely.

The mechanical etching is an alternative option for printed antenna fabrication. As the parameter size of the antenna is too small (0.15 mm width of the slot) and the laser machine could only offer 0.1 mm minimum precision, mechanical etching is thus chosen for this fabrication. The fabricated antenna comparing with one-euro cent is presented in Figure 5.5. The scale of the ruler is in centimeters.

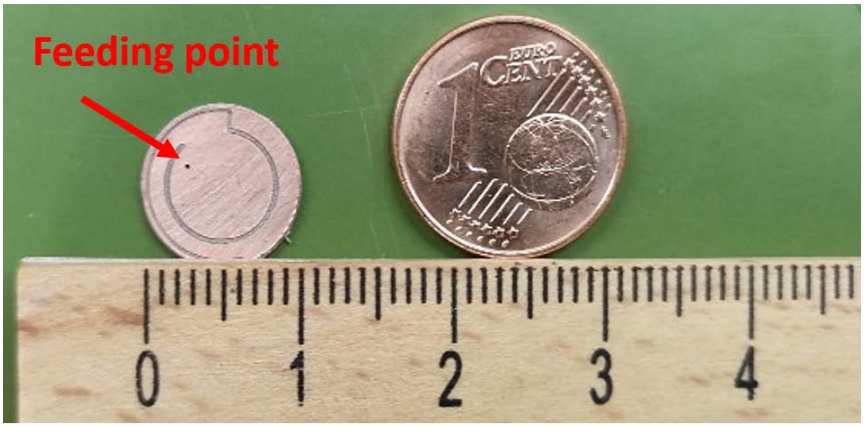

Figure 5.5 Mechanically fabricated antenna comparing with one-euro cent

As seen in Figure 5.5, the antenna is tiny ($\lambda_{403\ MHz}$ =74.4 cm; $\lambda_{915\ MHz}$ =32.8 cm). The feeding point which sits next to the second slot measures only 0.3 mm in diameter, where the inner metal of the coaxial connector should go through and be soldered together with the antenna's front side. The metal on the backside of the antenna has a larger hole which is soldered with the outer metal of the coaxial connector. The top and the bottom side of the antenna are electrically connected only through the via near the edge. Top and bottom views of the antenna are shown in Figure 5.6.

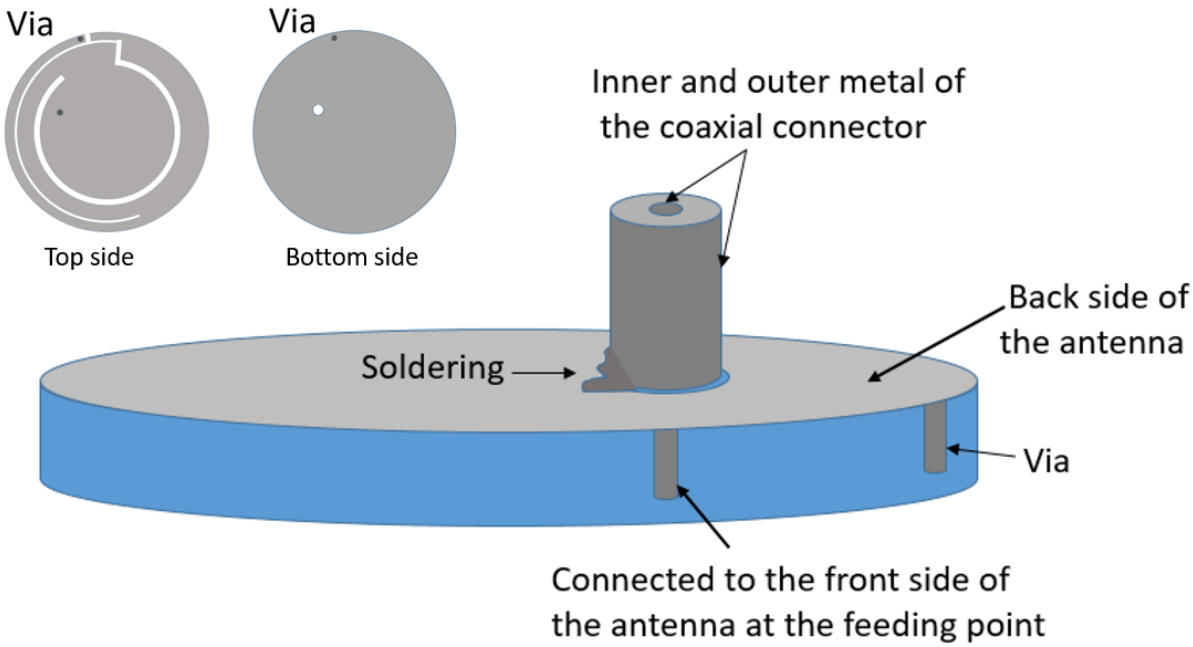

Figure 5.6 Antenna structure after soldering

To prevent direct contact between the antenna and the environment, the antenna should be covered by a superstrate that is the same size as the substrate but without metal. The two parts are glued with each other as mentioned in section 2.2.4. By setting the dielectric constant of the glue as 3.5, the thickness of the glue as 0.3 mm, the new

simulation results remain almost the same. The new antenna model with glue is shown in Figure 5.7.

The glue is added between the radiating patch and the superstrate.

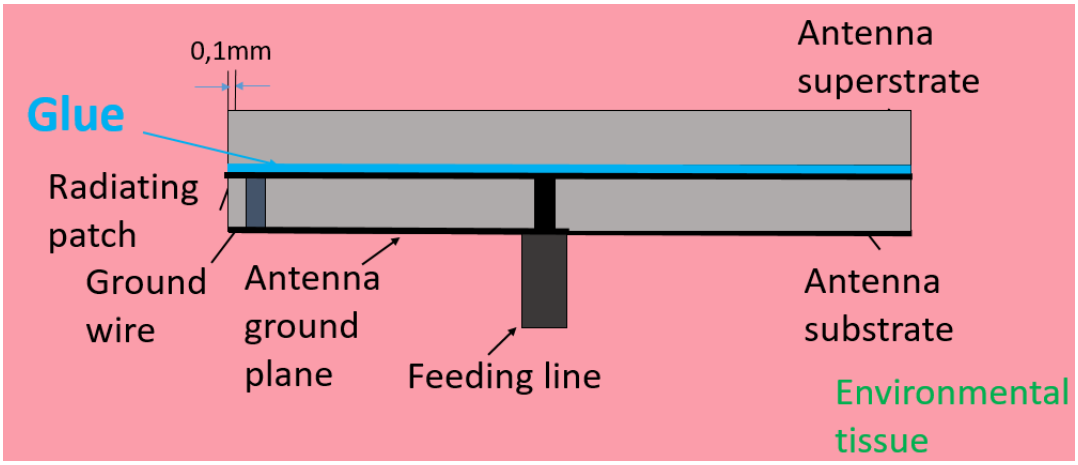

Figure 5.7 Realistic antenna model with glue

5.2.3 Environmental setup and measurements

5.2.3.1 Biological environment

In order to simulate the "arm" environment, a cylindrical phantom should be used. The phantom should not have a thick external layer which could generate some reflections. Thus, a plastic cup whose thickness is negligible is used for maintaining the 'arm' shape. The measurement scenario is first simulated by CST and results are compared with those of the antenna implanted in the arm. As found in this comparison, the implantation depth should be 10 mm deeper (comparing to the location in simulation) to obtain the same transmission efficiency. The scenario is shown in Figure 5.8.

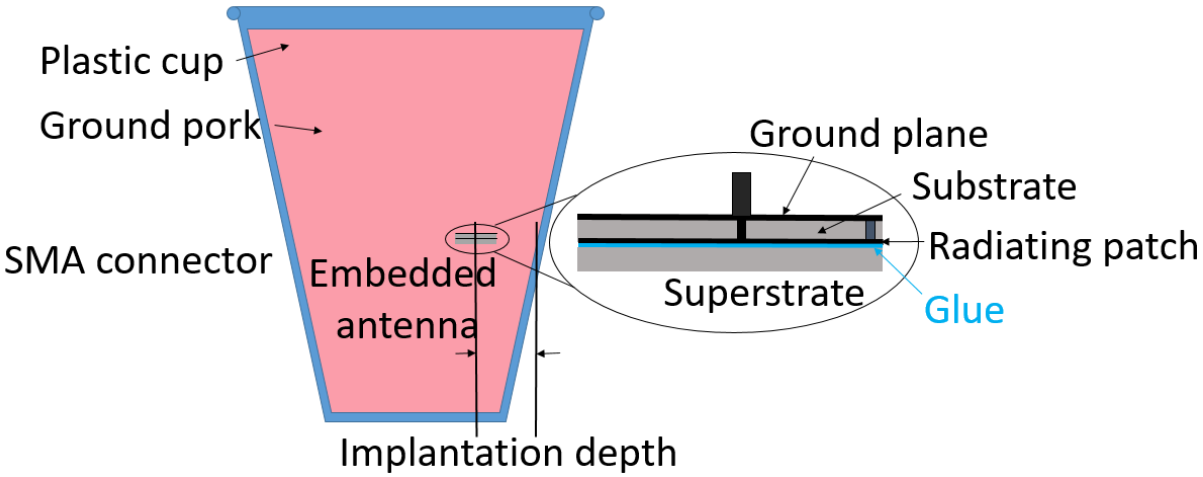

Figure 5.8 Measurement scenario with the plastic cup

The implantation depth is the distance between the edge of the antenna and the cup surface at the same height. The coaxial connector is not drawn in Figure 5.8.

According to the literature and experience [92], animal tissues are usually used as a replacement for 'human tissue' since it is more realistic than using dielectric emulating liquids. The dielectric emulating liquid could only be used for mimicking the human tissue at a certain frequency. Therefore, it is more suitable for applications that the operating frequency is strictly fixed. Yet for the real meat, even when there is frequency shifting, it is still a realistic biological environment. Here in the next sections, two different kinds of animal tissues are used and evaluated: Porcine tissue and bovine tissue. Results are discussed.

5.2.3.2 First measurement (Univ. Patras)

The first measurement is done in the laboratory of the Electrical Engineering School in the University of Patras in Greece. The antenna is fabricated by mechanical etching and measured. The soldered antenna is shown in Figure 5.9.

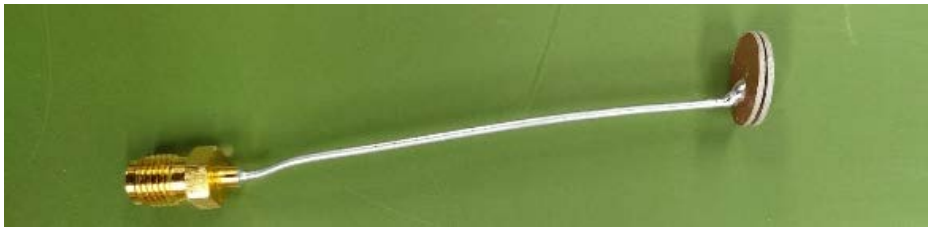

Figure 5.9 Antenna soldered with the coaxial connector

Since the antenna is very small and the results can be sensitive to the antenna's accurate placement, it is important that the antenna is well-positioned. Also, the cable should be vertical to the antenna surface in order not to affect the antenna's operation.

It is worth pointing out that the coaxial connector will not be present when the system is finally embedded into the human body. The antenna receives power from the external antenna and transfers the power directly to the rectifying circuit. The design will be shown in section 5.5.

During this measurement, the ground pork meat is used as the simulation environment as shown in Figure 5.10.

Figure 5.10 Antenna embedded together with the coaxial connector

The antenna is vertically inserted into the minced pork tissue since its main lobe is parallel to the antenna surface. It was mentioned in chapter 2 since this was the first trial, the results were not satisfactory. The reflection coefficient (S_{11}) of the antenna could be easily perturbed and an obvious frequency shifting was observed during this measurement. This is because of the direct contact between the metallic radiating patch and the minced pork meat. As a consequence, the resistance (the real part of the impedance) of the antenna at its first resonant frequency (403 MHz) is smaller and the reactance (the imaginary part of the impedance) of the second resonant frequency (915 MHz) is larger than expected.

As a result, two simulations were performed for comparison: With the radiating metallic patch isolated from the biological tissue by the glue or in contact with the tissue (details see Figure 5.11 [a], [b]).

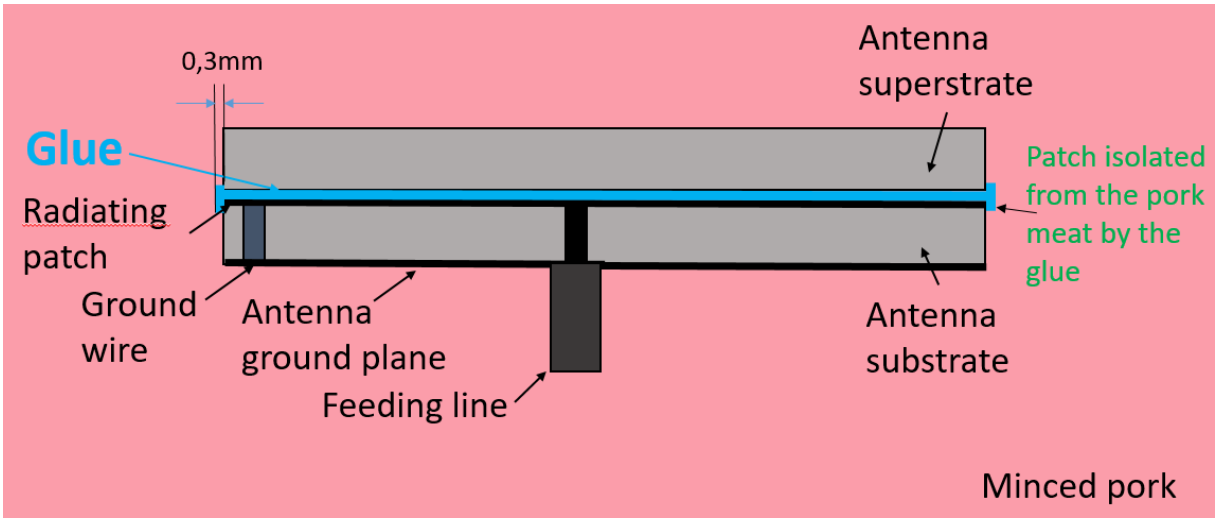

[a]

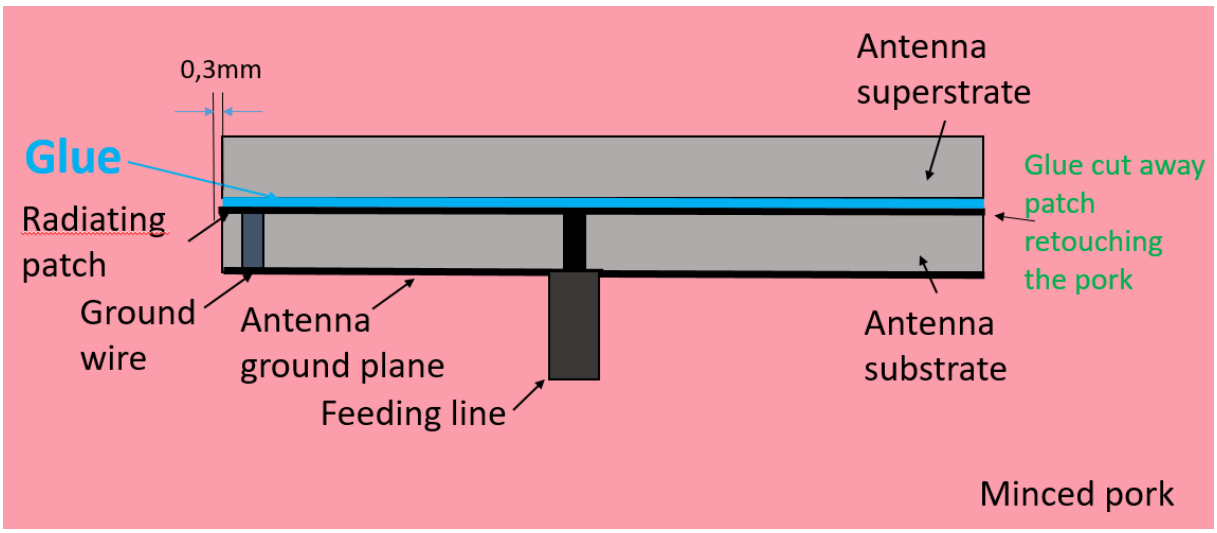

[b]

Figure 5.11 Detailed model with the antenna [a] isolated from [b] in contact with the pork tissue

In the first simulation, which corresponds to the experimental case, the patch is isolated by 0.3 mm thickness of glue while in the second case, the glue is cut away from the patch and, the patch contacts the tissue again. For each simulation case, a corresponding measurement is also done for the purpose of validation.

In order to better explain the case, 400 MHz is taken as an example and the antenna's impedance (resistance and reactance) is shown in Figure 5.12.

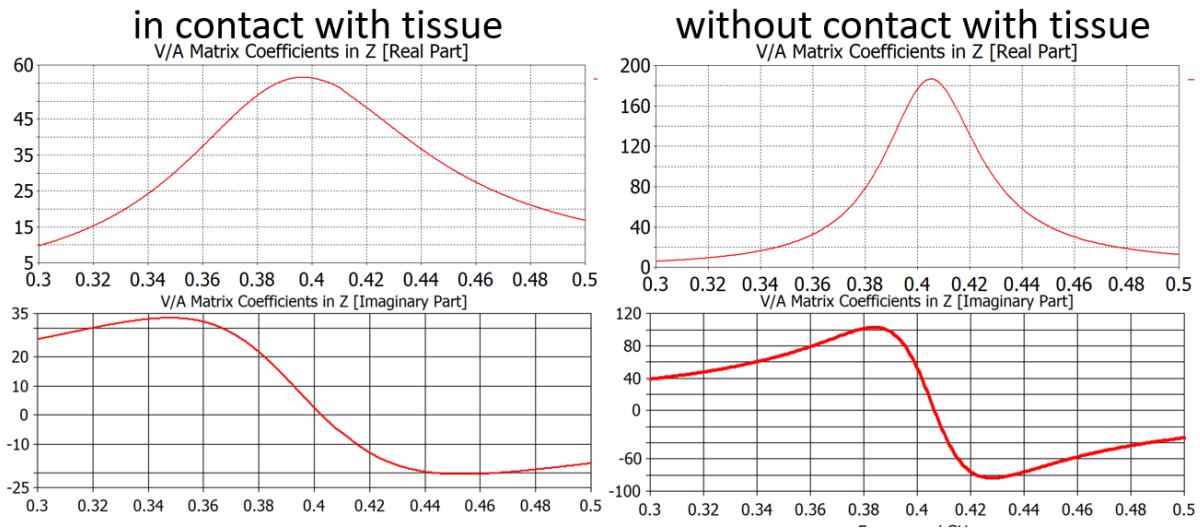

Figure 5.12 The impedance of the antenna with/without contact with the biological tissue (402 MHz) vs. frequency

In Figure 5.13, the S_{11} value in dB is presented vs operating frequency. We can observe a clear difference in the antenna's resistance (real part) at this resonant frequency. According to the simulation results, the resistance of the antenna increases from 56 Ω to 187 Ω when it loses contact with the tissue. The resonant frequency has also shifted for about 5 MHz.

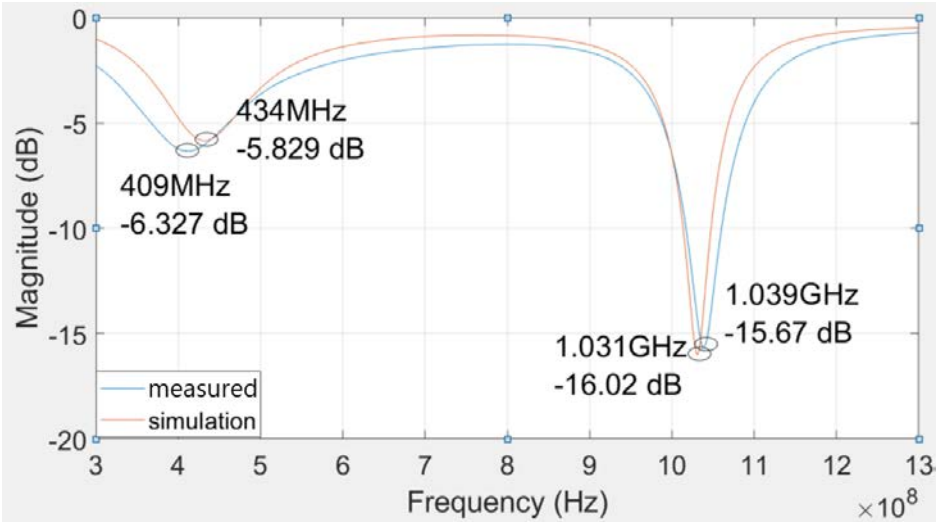

[a]

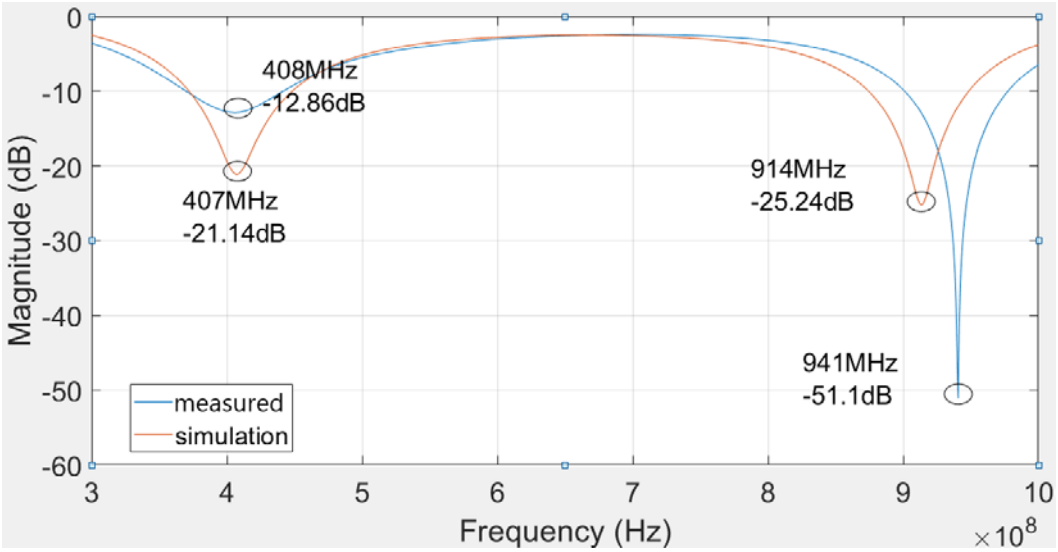

[b]

Figure 5.13 Simulation results comparing with measurement results [a] isolated from tissue [b] in contact with tissue

As we can observe in Figure 5.13, the measured results match globally the simulation results. In the first Figure 5.13 [a], the frequency shifting is synchronized for each resonant frequency. There is still some slight difference which is probably caused by air bubbles in the minced pork, as the experimental results ameliorate when some pressure is put on the tissue.

5.2.3.3 Second measurement (GeePs)

Different from the first measurement, the second measurement was done in an anechoic chamber in GeePs laboratory in order to verify the expected improvements.

The antenna is refabricated and resoldered as shown in Figure 5.14. The coaxial connector is bent 90° for the purpose of avoiding radiation perturbations from the coaxial connector since its size is not negligible to the antenna. The bending position is shown in Figure 3.9 (chapter 3).

Figure 5.14 Soldered and bent antenna

Since several differences were observed during the last experiment probably due to the biological tissue environment, Table 5.1 shows the dielectric properties of the

porcine tissue and human tissue [93] [94] at 915 MHz. The human tissue property values are cited from the CST database.

Table 5.1 Dielectric properties comparison

	Ground pork	**Human muscle**
ε_r	39.8	54.9
σ (S/m)	0.65	0.93

As we have observed during the last measurement and in this table, there is still some slight difference between the two kinds of tissue. The reason is suspected to be that the ground pork contains more fat than human muscle. Fat has a relative permittivity much lower than the muscle (see Table 1.3 in chapter 1). Therefore, bovine tissue with less fat is in use for comparison. The measurement scenario and results are shown in Figure 5.15.

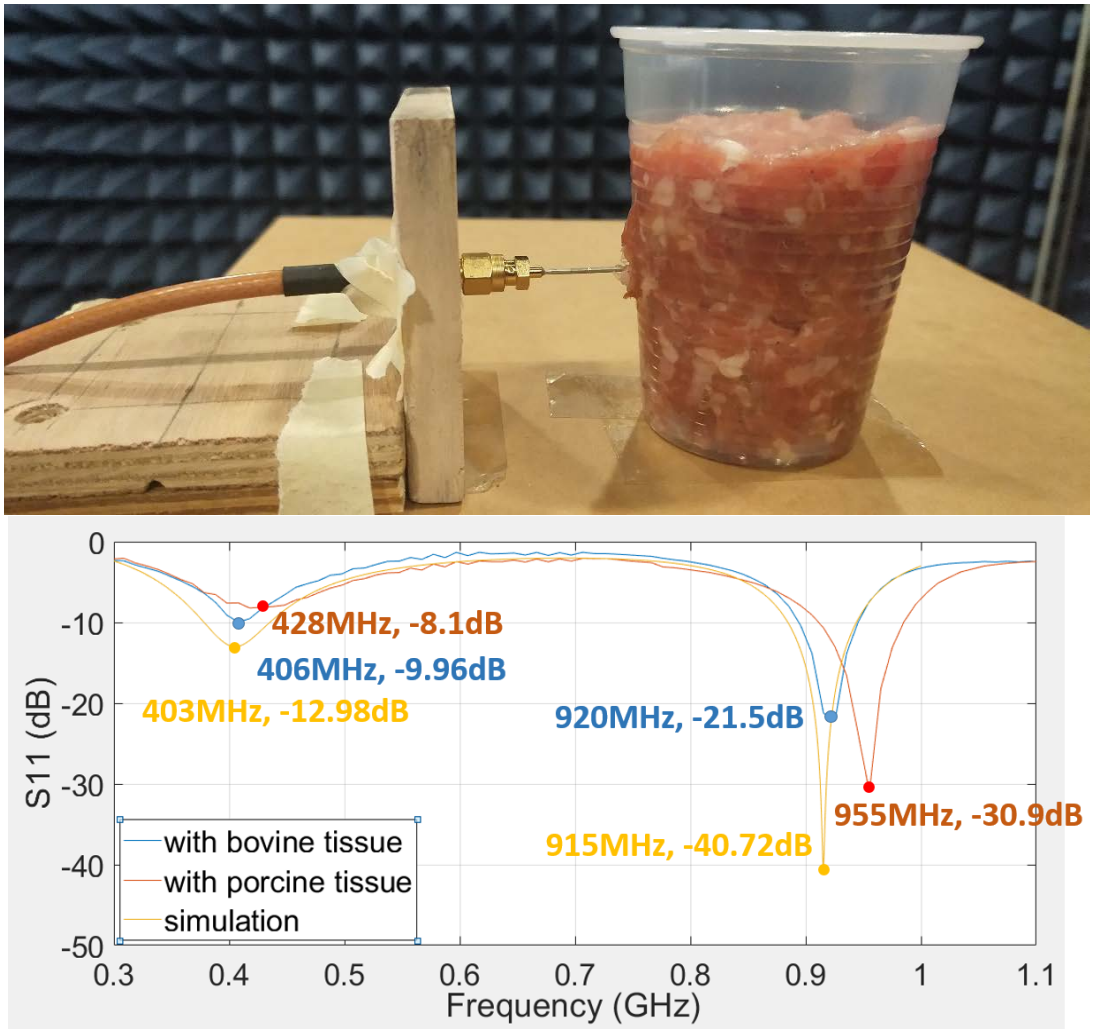

Figure 5.15 Antenna's reflection coefficient while embedded into different types of animal tissue as compared to simulation results

As seen, the antenna's resonant frequencies when implanted into bovine tissues (5% fat) slightly shift to higher values but are still within the authorized band. The shifting may be caused by two possible reasons: The 5% fat in the tissue and random air bubbles that exist among the tissue. Both factors will decrease the permittivity of the environment and change the resonant frequency of the antenna.

The ground pork meat has 20% to 30% of fat inside; the ground beef meat used has only less than 5% of fat inside and fat has a lower permittivity than lean meat. In simulations, a homogenous human muscle is used as an embedding environment. Therefore, when the bovine tissue (with less fat) is used, results are closer to those from the simulation. Nevertheless, in real life, people with only 5% fat are not that common, so the results using ground pork are closer to reality.

5.3 Transmission measurements

During both transmission measurements, a wide-band antenna is used as the external antenna instead of a patch antenna. This is because the embedded antenna resonant frequencies usually have slight shifting according to different surrounding environment. It could be difficult for a patch antenna to always resonate exactly at the corresponding frequencies. Therefore, a logarithm antenna is used thanks to its large resonant frequency band.

5.3.1 First transmission measurement (Univ. Patras)

As mentioned before, the first measurement was also performed at the University of Patras. The transmission scenario establishment is shown in Figure 5.16.

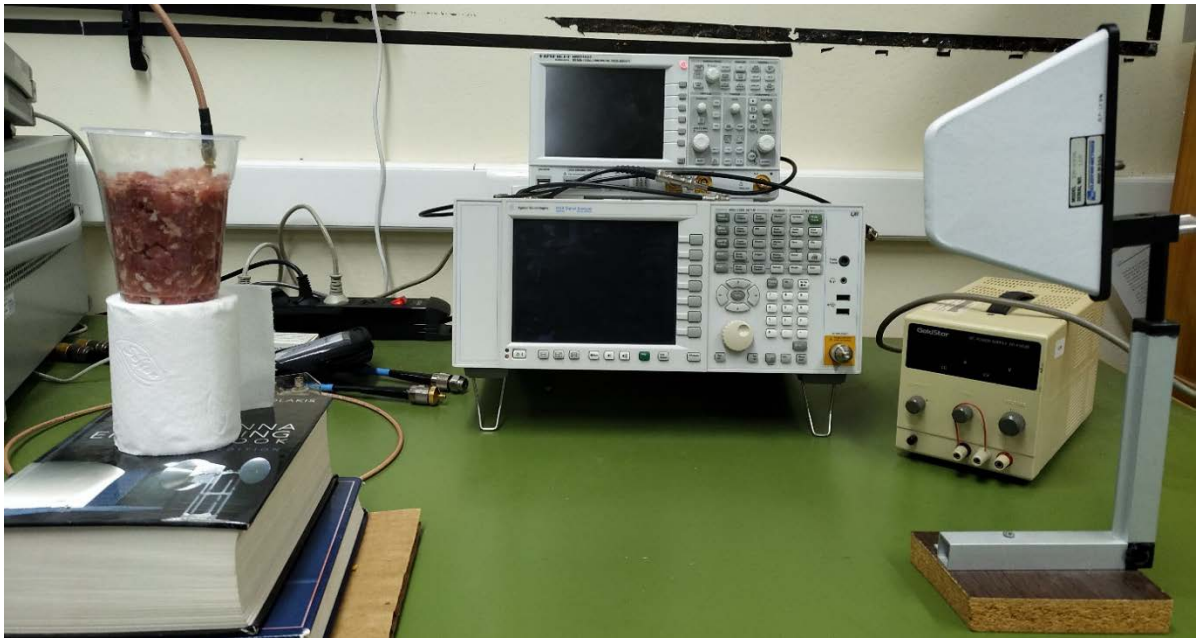

Figure 5.16 Transmission scenario during the first measurement

The plastic cup which is filled with minced pork is set to the same height as the transmission antenna. The transmission antenna is the logarithmic periodic antenna EM6936 from the Electro-Metrics company. The antenna operates from 700 MHz to 1300 MHz (gain: 3-6 dBi), which covers the second operating frequency of the antenna (902.8 MHz – 928 MHz). The transmission antenna and the embedded antenna are connected to the two ports of the VNA and the transmission distance is around 400 mm. The transmission results are shown in Figure 5.17.

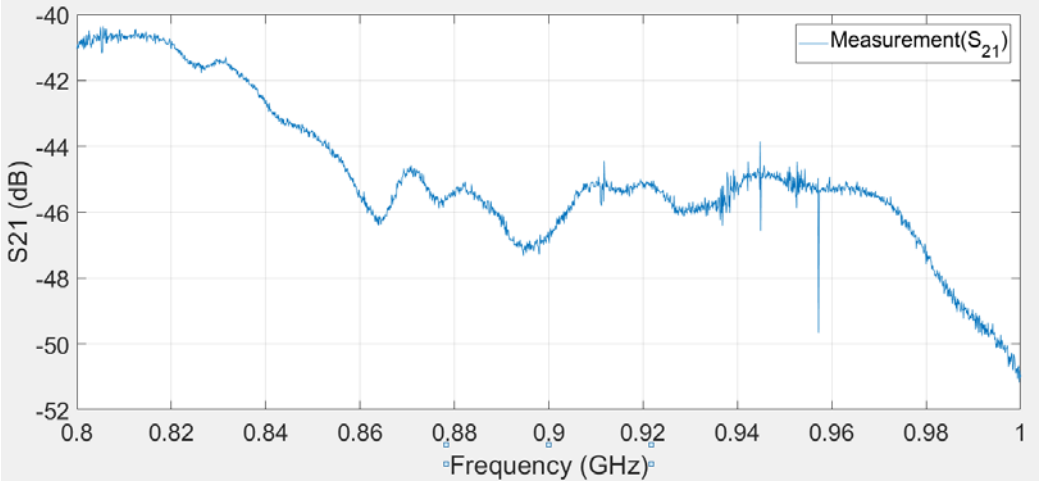

Figure 5.17 S_{21} results for the first measurement

The results show that the transmission efficiency has a local peak value at around 915 MHz at -45 dB. The result values are higher than those in the simulations with the external patch antenna. This is not only because the log antenna has a higher gain than the patch but also because the metallic instruments around and other metallic parts could reflect the waves and thus forms a 'reflector' as the one mentioned in chapter 3. The results here are thus not reliable enough for validation.

5.3.2 Second transmission measurement (GeePs)

Due to lack of time and less reliability of the first measurement results, a second measurement was planned and conducted in GeePs.

In GeePs, the available transmission antenna is the log-periodic antenna ESLP 9145 from Schwarzbeck company. Due to the embedded antenna's tiny size, the far-field range of it is much smaller than the external antenna. The length of the external antenna is 50 cm. It has a gain of around 6 dBi and is linearly polarized. The transmission scenario is shown in Figure 5.18.

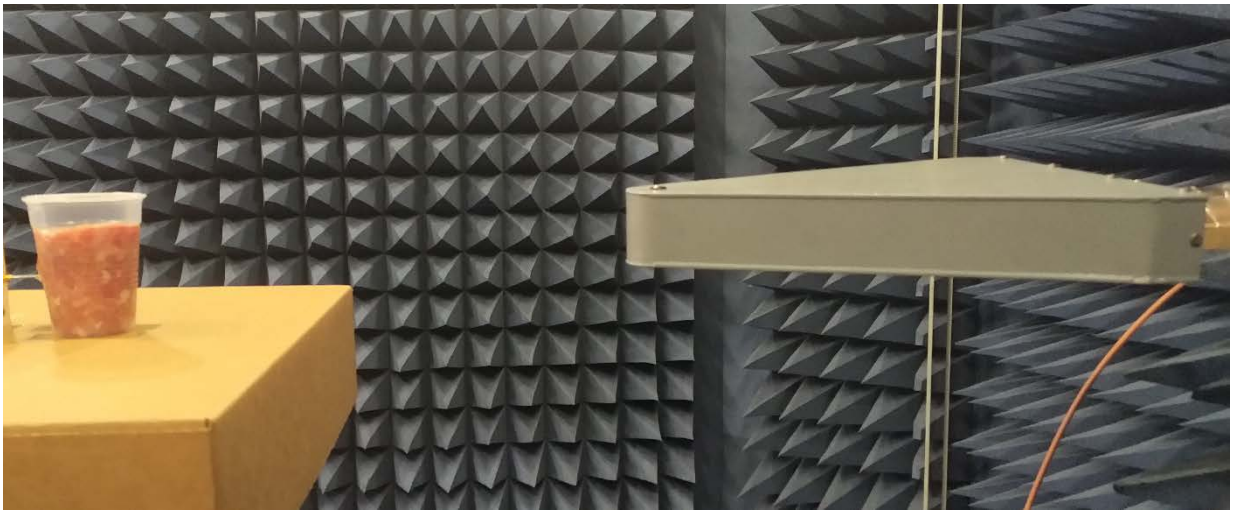

[a]

[b]

Figure 5.18 Experiment transmission model (porcine meat)
([a] without reflector [b] with reflector) (not real transmission distance)

This Figure 5.18 shows two different transmission scenarios, with or without the presence of the metallic reflector. It should be mentioned that the transmission distance which is shown in Figure 5.18 is not the real distance, as for real distance, the structures could not be presented clearly. During this measurement, the enhancement of the reflector is examined and validated. The results comparison of the two situations – with or without the metallic reflector, for 1 m transmission distance (in its far field range) are shown in Figure 5.19.

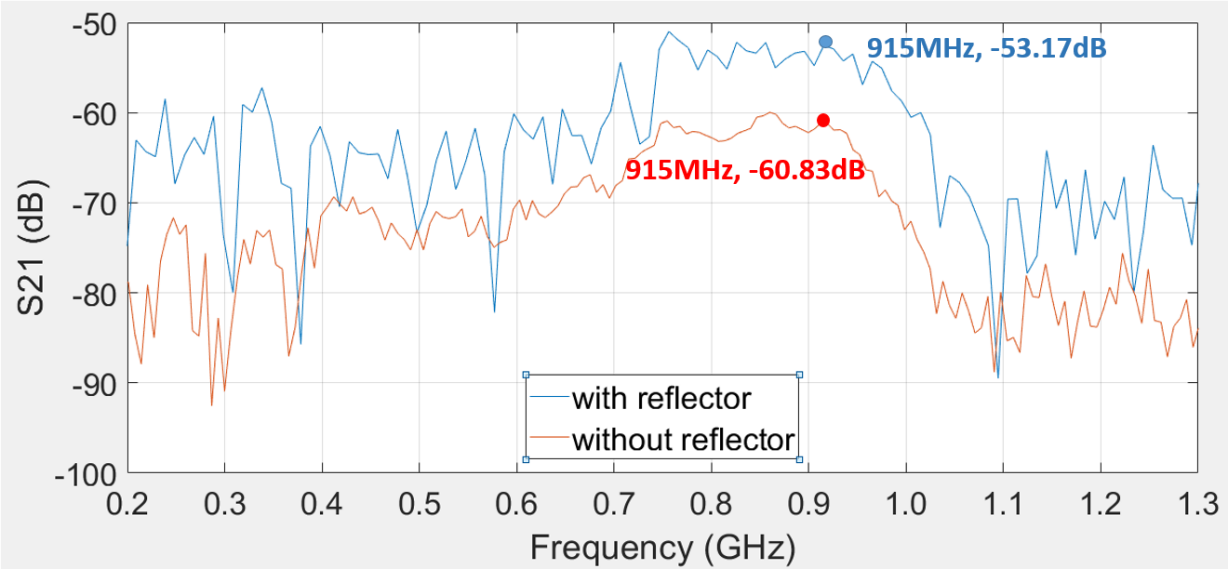

Figure 5.19 Transmission results comparison

As seen, the S_{21} is enhanced by around 7 dB with the presence of the reflector at 915 MHz, which validates the simulation results in chapter 3.

5.4 Circuit measurements

5.4.1 Circuit fabrication

As an essential part of the power transmission system, the circuit is tested separately in order to measure its performance. For the fabrication of the circuit, laser and mechanical etching method is used.

For the laser method, the first thing to pay attention is the heat resistivity of the material. Only heatproof material can be manufactured by this method without being melt or deformed during the process.

As we mentioned in chapter 4, the circuit material is Rogers RO3210. RO3210 could maintain its shape thanks to the integrated glass fiber. However, since the copper cladding thickness is 0.017 mm, the laser should be set to low power with more passes in order to minimize the burning.

The mechanical etching is an option and a more reliable method. Although most part of the copper is removed from the surface and a drill could create grooves on the material surface and reduce the flatness due to its sharp head, the via could only be fabricated through this method in our situation.

All the necessary components are of 0603 (16 mm x 0.8 mm) package for space-saving reasons. The following Figure shows the unsoldered and soldered circuit and the corresponding simulation model.

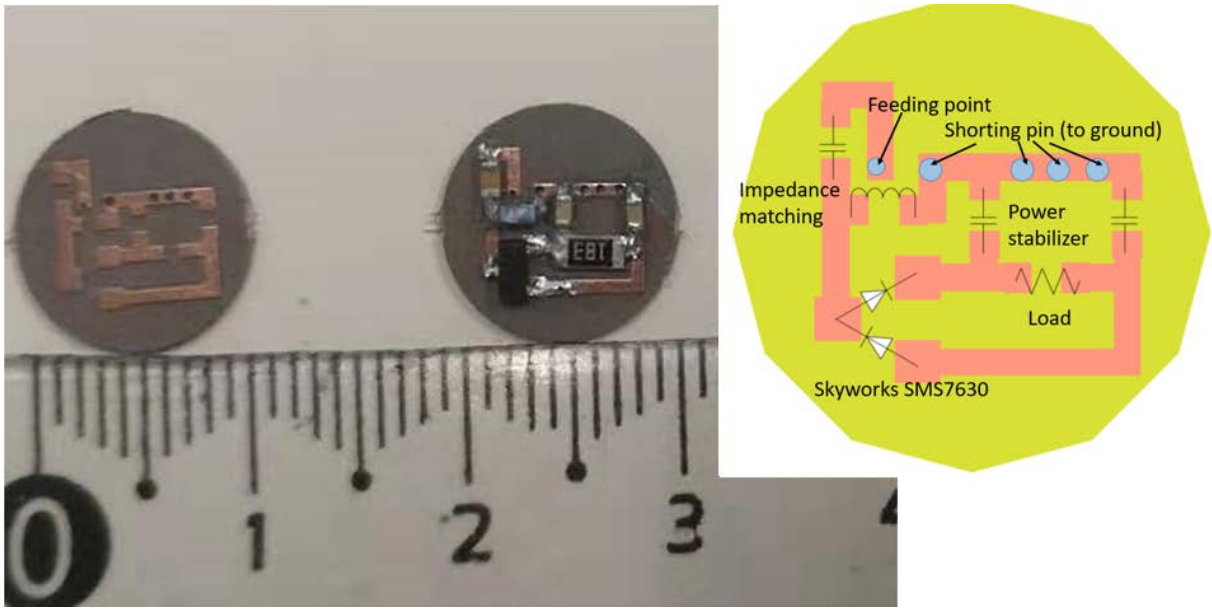

Figure 5.20 Unsoldered and soldered circuit with the simulation model

5.4.2 Measurements

The measurement is performed by the RHODES & SCHWARZ ZNB Vector Network Analyzer (VNA). The VNA provides -20 dBm of power from its output port for the circuit. The impedance of the total circuit and the voltage between the load are measured during the experiment. The load is an 18 kΩ resistance instead of a 13 kΩ but the results difference is negligible.

In order to proceed with the measurement, calibration is an important step. Differently from the previous antenna measurement, the circuit is more sensitive and difficult to calibrate. In Figure 5.21 we show the special calibration kit for this measurement:

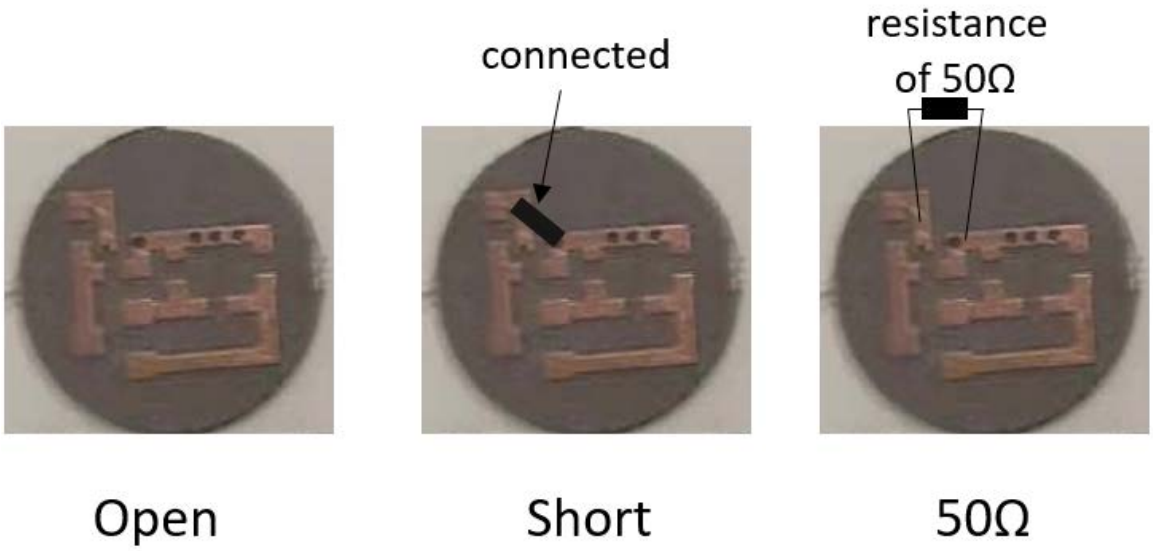

Figure 5.21 The specially made "calibration kit"

The special “calibration kit” has three components in total: An empty circuit which serves as an “open circuit”, a circuit with feeding and ground connected which serves as an “short circuit” and a 50 Ω connected between the feeding and ground which serves as the standard load. All these three components have the same length of the coaxial connector as the testing circuit in order to minimize any difference from elsewhere.

The total impedance of the circuit is around 32-31j Ω, which is nearly matched with the standard 50 Ω impedance at 915 MHz. The reflection coefficient is -7.8 dB. The voltage at the load is measured as 0.07 V by a multimeter placed at the two ends of the 18 kΩ load. The value presents some difference with the simulation results, which is likely due to the tiny size of the circuit. The measurement impedance could even be affected by the different sizes of the soldering dot.

5.5 Conclusion

In this chapter, the experimental procedures are introduced and described in detail. For the antenna measurement, the equipment utilized and their functions are firstly introduced. Two measurements are presented (one in Univ. Patras the other in GeePs). Several results from the first measurement are not as expected. The problem was diagnosed as the direct antenna-tissue contact and the assumption was validated by the second measurement. Furthermore, during the second measurement, some further issues were also addressed, such as: The surrounding tissue, the reflector presence, etc. These issues are studied in details in order to eliminate their negative effects. Finally, a measurement of the circuit is also done.

Conclusion and Perspectives

Conclusion

In this thesis, a complete wireless power transmission system is designed, simulated, and tested. The system operates at 915 MHz (ISM band: 902.8 – 928 MHz) in order to have better performance. The system could be globally divided into 4 parts: The embedded antenna, the external antenna, the rectifying circuit, and a power-consuming sensor.

The embedded antenna is a dual-band, miniaturized, circular dipole antenna. The total antenna has a radius of 11 mm and a thickness of 1.28 mm. It has 2 resonant frequencies: 403 MHz (MedRadio band) and 915 MHz (ISM band) which are created by the 2 circular slots on the patch surface. For both frequencies, the -10 dB bandwidths are around 60 MHz which cover the entire operating band. For each resonant frequency of the antenna, the gain of the antenna (in-body) is **-33.65 dB for the 403 MHz band and -29.45 dB for the 915 MHz band.** The simulation environment is a three-layer cylinder (bone 25 mm, muscle 25 mm - 47.5 mm, and skin 47.5 mm - 50 mm) that simulates the human arm.

According to the e-CFR regulation and the FCC requirements, the maximum authorized power for the 915 MHz band is around 40 times higher than for the MedRadio band. Therefore, the 915 MHz ISM band is chosen for power transmission use. The external antenna is chosen as a patch antenna because of its easy modeling and its suitable directivity value for the FCC requirements. In order to maximize the power transmission efficiency and patient comfort, the embedded antenna should be placed in parallel with the muscle fiber at a special angle (see Figure 3.9). The impact of the transmission distance, the implantation depth on the transmission efficiency is studied. Also, a metallic reflector is proposed to enhance transmission efficiency. The reflector should have its focal point at the embedded antenna's position and has an open angle of 210° for optimization. The total enhancement could achieve 6-8 dB for different implantation depths and transmission distances. **The enhanced S21 could achieve around -35 dB for 400 mm transmission distance and 14 mm implantation depth.** The safety issues are considered as well: The SAR values are 10 times lower than the limit for the nearest transmission distance in the far-field range and 12 mm deep implanted.

Due to the low power level for the antenna, the rectifying circuit should be small, low power-consuming, and efficient.

- In order to be small, the circuit uses components of 0603 package (size: 1.6 mm x 0.8 mm), and the circuit has the same size as the antenna's substrate to avoid increasing the system's size.

- To consume less power, the circuit is using only 2 components for impedance matching for reducing the loss.
- To be efficient, the electromagnetic properties of the circuit copper track are also taken into account and the circuit uses a voltage doubler to rectify as much power as possible.

In the simulations, off-the-shelf components are used in order to obtain results that are closer to reality. Through antenna-circuit combination analysis, with the most optimized configuration, **the entire system is able to receive 56.9 µW for 400 mm power transmission distance and 233.6 µW for 200 mm power transmission distance.**

In the previous literature, many sensors could operate normally with the mentioned power value for our system (see section 4.2).

Also, in chapter 3, a mathematical method is proposed for the purpose of diagnosing the variables' impact and results prediction. The method turns out to be efficient since it could predict results basing on a few samples without losing much accuracy. Furthermore, in chapter 2 and 4, some important matters needing attention while using the simulation tools (CST and ADS) of the thesis are detailed.

Finally, some measurements were performed in order to validate the simulation results. By analyzing the problems encountered during the first measurement, the antenna design was to be improved and the experimental environment was questioned. By designing a new antenna and altering the porcine tissue (more fat) to bovine tissue (less fat), **the measurement results have been significantly improved and the antenna works as in simulations. The system performance is proved.**

Perspectives

Future research is suggested in the following aspects:

1. The antenna-circuit combination measurement should be done for more precise validation of the system. This was not done during the thesis because of the Covid-19 situation in France.
2. The sensitivity analysis method that is presented at the end of chapter 3 could be widely developed. This method is very powerful since it could predict any logical results from only a few existing results. This could largely reduce the computation time, especially for heavy simulations which last for about one hour in this thesis. And the impact diagnosing method is also useful for realistic uses.

3. For realistic uses, fat is always an issue for implantation. It has a permittivity a lot lower than other human tissues and thus could be a problem. Fat might be used as a special “wearable” material for wave refraction and thus could help to enhance power transmission.
4. For the circuit, a low power DC booster could be applied in order to increase the output voltage in order to fulfill various more cases.
5. Finally, some in vivo experiments could be done. This could increase largely the precision of the measurement and get a more concrete evaluation of the system.

References

1) F. Huang, C. Lee, C. Chang, L. Chen, T. Yo and C. Luo, "Rectenna Application of Miniaturized Implantable Antenna Design for Triple-Band Biotelemetry Communication," in *IEEE Transactions on Antennas and Propagation*, vol. 59, no. 7, pp. 2646-2653, July 2011, doi: 10.1109/TAP.2011.2152317.

2) Y. Hao, A. Alomainy, P. S. Hall, Y. I. Nechayev, C. G. Parini and C. C. Constantinou, "Antennas and propagation for body centric wireless communications," *IEEE/ACES International Conference on Wireless Communications and Applied Computational Electromagnetics, 2005.*, Honolulu, HI, 2005, pp. 586-589, doi: 10.1109/WCACEM.2005.1469656

3) H. Hamouda, P. Le Thuc, R. Staraj and G. Kossiavas, "Small antenna embedded in a wrist-watch for application in telemedicine," The 8th European Conference on Antennas and Propagation (EuCAP 2014), The Hague, 2014, pp. 876-879, doi: 10.1109/EuCAP.2014.6901902.

4) P. Perrissol, A. Diallo, P. Le Thuc, R. Staraj and G. F. Carle, "Performance of a cross dipole antenna dedicated to biological telemetry," The 8th European Conference on Antennas and Propagation (EuCAP 2014), The Hague, 2014, pp. 2174-2177, doi: 10.1109/EuCAP.2014.6902240.

5) C. Liu, Y. Zhang and X. Liu, "Circularly Polarized Implantable Antenna for 915 MHz ISM-Band Far-Field Wireless Power Transmission," in *IEEE Antennas and Wireless Propagation Letters*, vol. 17, no. 3, pp. 373-376, March 2018, doi: 10.1109/LAWP.2018.2790418.

6) R. Joshi, S. Podilchak, D. Anagnostou et al., "Analysis and Design of Dual-Band Folded-Shorted Patch Antennas for Robust Wearable Applications," in IEEE Open Journal of Antennas and Propagation, vol. 1, pp. 239-252, 2020, doi: 10.1109/OJAP.2020.2991343.

7) Image from http://cargocollective.com/futurehealth/pillcam

8) M. A. Hannan, S.Mutashar, S. A. Samad, and A. Hussain,. Energy harvesting for the implantable biomedical devices: Issues and challenges. *BioMedical Engineering Online*, *13*(1), 1–23, 2014. https://doi.org/10.1186/1475-925X-13-79

9) M. Schormans, V. Valente and A. Demosthenous, "Practical Inductive Link Design for Biomedical Wireless Power Transfer: A Tutorial," in *IEEE Transactions on Biomedical Circuits and Systems*, vol. 12, no. 5, pp. 1112-1130, Oct. 2018, doi: 10.1109/TBCAS.2018.2846020

10) O. Knecht, R. Bosshard and J. W. Kolar, "High-Efficiency Transcutaneous Energy Transfer for Implantable Mechanical Heart Support Systems," in *IEEE Transactions on Power Electronics*, vol. 30, no. 11, pp. 6221-6236, Nov. 2015, doi: 10.1109/TPEL.2015.2396194.

11) D. Jiang, D. Cirmirakis, M. Schormans, T. A. Perkins, N. Donaldson and A. Demosthenous, "An Integrated Passive Phase-Shift Keying Modulator for Biomedical Implants With Power Telemetry Over a Single Inductive Link," in *IEEE Transactions*

on Biomedical Circuits and Systems, vol. 11, no. 1, pp. 64-77, Feb. 2017, doi: 10.1109/TBCAS.2016.2580513.

12) Y. Wang, D. Ye, L. Lyu, Y. Xiang, H. Min and C. -. R. Shi, "A 13.56MHz Wireless Power and Data Transfer Receiver Achieving 75.4% Effective-Power-Conversion Efficiency with 0.1% ASK Modulation Depth and 9.2mW Output Power," *2018 IEEE International Solid - State Circuits Conference - (ISSCC)*, San Francisco, CA, 2018, pp. 142-144, doi: 10.1109/ISSCC.2018.8310224.

13) W. H. Ko, J. Hyneck and J. Homa, "Single Frequency RF Powered ECG Telemetry System," in *IEEE Transactions on Biomedical Engineering*, vol. BME-26, no. 2, pp. 105-109, Feb. 1979, doi: 10.1109/TBME.1979.326518.

14) A. Kurs, A. Karalis, R. Moffatt, J. D. Joannopoulos, P. Fisher, and M. Soljacic, "Wireless Energy Transfer via Strongly Coupled Magnetic Resonances," Science, vol. 317, pp. 83-85, 2007.

15) H. Hu and S. V. Georgakopoulos, "Wireless powering of biomedical implants by Comformal Strongly Coupled Magnetic Resonators," *2015 IEEE International Symposium on Antennas and Propagation & USNC/URSI National Radio Science Meeting*, Vancouver, BC, 2015, pp. 1207-1208, doi: 10.1109/APS.2015.7304992.

16) O. Jonah, S. V. Geogakopoulos, and M.M. Tentzeris, "Strongly Coupled wireless power transfer with conformal structures," *IEEE Antennas Propagat.* Society Internat. Symp., Lake Buena Vista, FL, Jul. 2013

17) J. Barreto, A. Kaddour and S. V. Georgakopoulos, "Conformal Strongly Coupled Magnetic Resonance Systems With Extended Range," in *IEEE Open Journal of Antennas and Propagation*, vol. 1, pp. 264-271, 2020, doi: 10.1109/OJAP.2020.2999447.

18) WILLIAM C. BROWN. (1984) The History of Power Transmission Radio Waves, *IEEE Transactionson Microwavetheoryand Techniques,Vol. Mtt-32, No. 9, September, 1984*

19) H. Kim, H. Hirayama, S. Kim, K. J. Han, R. Zhang and J. Choi, "Review of Near-Field Wireless Power and Communication for Biomedical Applications," in *IEEE Access*, vol. 5, pp. 21264-21285, 2017, doi: 10.1109/ACCESS.2017.2757267.

20) S. Rao and J. -. Chiao, "Body Electric: Wireless Power Transfer for Implant Applications," in *IEEE Microwave Magazine*, vol. 16, no. 2, pp. 54-64, March 2015, doi: 10.1109/MMM.2014.2377586.

21) B. Zhang, X. H. Hao. Modeling and analysis of wireless power transmission system via strongly coupled magnetic resonances, 2014 International Conference on Mechatronics and Control (ICMC) July 3 - 5, 2014, 70–75.

22) Rahmani, H., & Babakhani, A.. A fully integrated electromagnetic energy harvesting circuit with an on-chip antenna for biomedical implants in 180 nm SOI CMOS. *Proceedings of IEEE Sensors*, 7–9. https://doi.org/10.1109/ICSENS.2016.7808979

23) S. Bakogianni, and S. Koulouridis, "A Dual-Band Implantable Rectenna for Wireless Data and Power Support at Sub-GHz Region," IEEE Transactions on Antennas and Propagation 67.11 (2019): 6800-6810.

24) Trung, N. T., Häfliger, P., & Member, S. (2015). A Submicrowatt Implantable Capacitive Sensor System for Biomedical Applications. IEEE Transactions on Circuits and Systems II: Express Briefs, 62(2), 209–213.

25) Chirwa, L. C., Hammond, P. A., Roy, S., & Cumming, D. R. S. (2003). Electromagnetic radiation from ingested sources in the human intestine between 150 MHz and 1.2 GHz. IEEE Transactions on Biomedical Engineering, 50(4), 484–492.

26) Schmidt, C., Casado, F., Arriola, A., Ortego, I., Bradley, P. D., & Valderas, D. (2014). 8.Broadband UHF implanted 3-D conformal antenna design and characterization for in-off body wireless links. IEEE Transactions on Antennas and Propagation, 62(3), 1433–1444.

27) Merli, F., Bolomey, L., Zürcher, J. F., Corradini, G., Meurville, E., & Skrivervik, A. K. (2011). Design, realization and measurements of a miniature antenna for implantable wireless communication systems. *IEEE Transactions on Antennas and Propagation*, *59*(10), 3544–3555. https://doi.org/10.1109/TAP.2011.2163763

28) Poon, A. S. Y., O'driscoll, S., & Meng, T. H. (2010). Optimal frequency for wireless power transmission into dispersive tissue. IEEE Transactions on Antennas and Propagation, 58(5), 1739–1750.

29) Kim, J., & Rahmat-Samii, Y. (2004). Implanted antennas inside a human body: Simulations, designs, and characterizations. IEEE Transactions on Microwave Theory and Techniques, 52(8 II), 1934–1943.

30) Soontornpipit, P., Furse, C. M., & Chung, Y. C. (2004). Design of implantable microstrip antenna for communication with medical implants. IEEE Transactions on Microwave Theory and Techniques, 52(8 II), 1944–1951.

31) Soontornpipit, P. (2005). Miniaturized biocompatible microstrip antenna using genetic algorithm. IEEE Transactions on Antennas and Propagation, 64(240), 69\\-1945.

32) Karacolak, T., Hood, A. Z., & Topsakal, E. (2008). Design of a dual-band implantable antenna and development of skin mimicking gels for continuous glucose monitoring. IEEE Transactions on Microwave Theory and Techniques, 56(4), 1001–1008.

33) Karacolak, T., Cooper, R., & Topsakal, E. (2009). 2.Electrical properties of rat skin and design of implantable antennas for medical wireless telemetry. IEEE Transactions on Antennas and Propagation, 57(9), 2806–2812.

34) Soora, S., Gosalia, K., Humayun, M. S., & Lazzi, G. (2008). A comparison of two and three dimensional dipole antennas for an implantable retinal prosthesis. *IEEE Transactions on Antennas and Propagation*, *56*(3), 622–629.

35) Gosalia, K., Humayun, M. S., & Lazzi, G. (2005). Impedance matching and implementation of planar space-filling dipoles as intraocular implanted antennas in a retinal prosthesis. *IEEE Transactions on Antennas and Propagation*, *53*(8 I), 2365–2373.

36) Liu, C., Wang, J., Yang, X., & Liu, X. (2017). Frequency Optimization of an Implantable Antenna for Far-field Wireless Power Transmission, (1), 154–155.

37) Liu, C., Guo, Y. X., & Xiao, S. (2012). A hybrid patch/slot implantable antenna for biotelemetry devices. *IEEE Antennas and Wireless Propagation Letters*, *11*, 1646–1649.

38) Xu, L. J., Guo, Y. X., & Wu, W. (2012). Dual-band implantable antenna with open-end slots on ground. *IEEE Antennas and Wireless Propagation Letters*, *11*, 1568–1571.

39) Liu, C., Guo, Y., & Xiao, S. (2014). Capacitively Loaded Circularly Polarized Implantable Patch Antenna for ISM-Band Biomedical Applications. *IEEE Transactions on Antennas and Propagation*, *PP*(99), 1–1.

40) Liu, C., Guo, Y. X., & Xiao, S. (2012). Compact dual-band antenna for implantable devices. *IEEE Antennas and Wireless Propagation Letters*, *11*, 1508–1511.

41) A. K. Skrivervik and F. Merli, "Design strategies for implantable antennas," LAPC 2011 - 2011 Loughborough Antennas and Propagation Conference, pp. 1–5, 2011.

42) A. K. Skrivervik, "Implantable antennas: The challenge of efficiency," 2013 7th European Conference on Antennas and Propagation, EuCAP 2013, no. Eucap, pp. 3627–3631, 2013.

43) Kiourti, A., & Nikita, K. S. (2012). Miniature scalp-implantable antennas for telemetry in the MICS and ISM bands: Design, safety considerations and link budget analysis. *IEEE Transactions on Antennas and Propagation*, *60*(8), 3568–3575.

44) Sánchez-Fernández, C. J., Quevedo-Teruel, O., Requena-Carrión, J., Inclán-Sánchez, L., & Rajo-Iglesias, E. (2010). Dual-band microstrip patch antenna based on short-circuited ring and spiral resonators for implantable medical devices. *IET Microwaves, Antennas & Propagation*, *4*(8), 1048.

45) Xia, W., Saito, K., Takahashi, M., & Ito, K. (2009). Performances of an implanted cavity slot antenna embedded in the human arm. *IEEE Transactions on Antennas and Propagation*, *57*(4 PART. 1), 894–899

46) Bakogianni, S., & Koulouridis, S. (2016). An Implantable Planar Dipole Antenna for Wireless MedRadio-Band Biotelemetry Devices. *IEEE Antennas and Wireless Propagation Letters*, *15*, 234–237.

47) Mohamed, A. E., & Sharawi, M. S. (2017). Miniaturized dual-wideband circular patch antenna for biomedical telemetry. *2017 11th European Conference on Antennas and Propagation (EUCAP)*, 1027–1030.

48) Das, R., & Yoo, H. (2017). A Multiband Antenna Associating Wireless Monitoring and Nonleaky Wireless Power Transfer System for Biomedical Implants. *IEEE Transactions on Microwave Theory and Techniques*, *65*(7), 2485–2495.

49) M. Haerinia and S. Noghanian, "Study of Bending Effects on a Dual-Band Implantable Antenna," *2019 IEEE International Symposium on Antennas and Propagation and USNC-URSI Radio Science Meeting*, Atlanta, GA, USA, 2019, pp. 753-754, doi: 10.1109/APUSNCURSINRSM.2019.8888320.

50) P. Anacleto, H. Dinis, J. Fernandes and P. M. Mendes, "Design and Characterization of 3-D Self-Folded Microantennas for Implantable Microdevices," in *IEEE Transactions on Antennas and Propagation*, vol. 68, no. 3, pp. 2031-2039, March 2020, doi: 10.1109/TAP.2019.2948741.

51) Q. Luu, S. Koulouridis, A. Diet, Y. Le Bihan and L. Pichon, "Investigation of inductive and radiating energy harvesting for an implanted biotelemetry antenna," *2017 11th European Conference on Antennas and Propagation (EUCAP)*, Paris, 2017, pp. 160-163, doi: 10.23919/EuCAP.2017.7928620

52) A. Basir and H. Yoo, "Efficient Wireless Power Transfer System with a Miniaturized Quad-Band Implantable Antenna for Deep-Body Multitasking Implants," in *IEEE*

Transactions on Microwave Theory and Techniques, vol. 68, no. 5, pp. 1943-1953, May 2020, doi: 10.1109/TMTT.2020.2965938.

53) N. Ganeshwaran, J. K. Jeyaprakash, M. G. N. Alsath and V. Sathyanarayanan, "Design of a Dual-Band Circular Implantable Antenna for Biomedical Applications," in *IEEE Antennas and Wireless Propagation Letters*, vol. 19, no. 1, pp. 119-123, Jan. 2020, doi: 10.1109/LAWP.2019.2955140.

54) Asif, S. M., Iftikhar, A., Hansen, J. W., Khan, M. S., Ewert, D. L., Braaten, B. D., & Member, S. (2019). A Novel RF-Powered Wireless Pacing via a Rectenna-Based Pacemaker and a Wearable Transmit-Antenna Array. *IEEE Access*, *7*, 1139–1148. https://doi.org/10.1109/ACCESS.2018.2885620

55) P. Soontornpipit and P. Satitvipawee, "Design and Development of a Dual-Band PIFA Antenna for Wireless Biotelemetry Applications," *2018 International Electrical Engineering Congress (iEECON)*, Krabi, Thailand, 2018, pp. 1-4, doi: 10.1109/IEECON.2018.8712165.

56) Computer Simulation Technology (CST) STUDIO SUITE. Ver 2017, Dassault Systèmes Simulia Corp, the U.S. http:// www.cst.com

57) D.Andreuccetti, R.Fossi and C.Petrucci: An Internet resource for the calculation of the dielectric properties of body tissues in the frequency range 10 Hz - 100 GHz. IFAC-CNR, Florence (Italy), 1997. Based on data published by C.Gabriel et al. in 1996. [Online]. Available: *http://niremf.ifac.cnr.it/tissprop/*

58) S. Bakogianni and S. Koulouridis, "On the Design of Miniature MedRadio Implantable Antennas," in *IEEE Transactions on Antennas and Propagation*, vol. 65, no. 7, pp. 3447-3455, July 2017, doi: 10.1109/TAP.2017.2702718.

59) Z. Erlangung, Detailed Modeling of the Human Body in Motion to Investigate the Electromagnetic Influence of Fields in a Realistic Environment. Ph.D dissertation. 2018

60) Said, Mohd & Seman, Norhudah & Jaafar, Haliza. (2015). Characterization of Human Head Phantom based on its Dielectric Properties for Wideband Microwave Imaging Application. Jurnal Teknologi. 73. 10.11113/jt.v73.4405.

61) OET bulletin 65 edition 97-01. FCC Std. Supplement C. Jun.2001

62) Costanzo, A., Dionigi, M., Masotti, D., Mongiardo, M., Monti, G., Tarricone, L., & Sorrentino, R. (2014). Electromagnetic energy harvesting and wireless power transmission: A unified approach. *Proceedings of the IEEE*, *102*(11), 1692–1711. https://doi.org/10.1109/JPROC.2014.2355261

63) H. Cheng, T. Yu and C. Luo, "Direct current driving impedance matching method for rectenna using medical implant communication service band for wireless battery charging," in *IET Microwaves, Antennas & Propagation*, vol. 7, no. 4, pp. 277-282, 19 March 2013.

64) B. J. DeLong, A. Kiourti and J. L. Volakis, "A Radiating Near-Field Patch Rectenna for Wireless Power Transfer to Medical Implants at 2.4 GHz," in *IEEE Journal of Electromagnetics, RF and Microwaves in Medicine and Biology*, vol. 2, no. 1, pp. 64-69, March 2018.

65) C. Liu, Y. Guo, H. Sun and S. Xiao, “Design and Safety Considerations of an Implantable Rectenna for Far-Field Wireless Power Transfer,” in *IEEE Transactions on Antennas and Propagation*, vol. 62, no. 11, pp. 5798-5806, Nov. 2014.

66) A. Okba, A. Takacs and H. Aubert, "Compact Rectennas for Ultra-Low-Power Wireless Transmission Applications," in *IEEE Transactions on Microwave Theory and Techniques*, vol. 67, no. 5, pp. 1697-1707, May 2019.

67) D. Vasisht, G. Zhang, O. Abari, D. Katabi, H. -M. Lu, and J. Flanz, "In-body Backscatter Communication and Localization," ACM SIGCOMM, 2018.

68) X. Fang *et al*., "Experimental In-Body to On-Body and In-Body to In-Body Path Loss Models of Planar Elliptical Ring Implanted Antenna in the Ultra-Wide Band," *2019 13th International Symposium on Medical Information and Communication Technology (ISMICT)*, Oslo, Norway, 2019, pp. 1-5.

69) International Telecommunications Union. (1998). Recommendation ITU-R RS.1346.

70) FCC 15. 209, Standard Specification for Radiated emission limits, general requirements

71) Konstatina S. Nikita. Handbook of Biomedical Telemetry [M]. John Wiley & Sons, Inc., Hoboken, New Jersey, 2014.

72) IEEE standard for safety levels with respect to human exposure to radiofrequency electromagnetic fields, 3 kHz to 300 GHz, IEEE Standard C95.1, 1999.

73) IEEE standard for safety levels with respect to human exposure to radiofrequency electromagnetic fields, 3 kHz to 300 GHz, IEEE Standard C95.1, 2005

74) Constantine A. Balanis. 2005. Antenna Theory: Analysis and Design. Wiley-Interscience, New York, NY, USA.

75) http://blog.gyminutesapp.com/2016/11/20/lifting-smart-series-muscle-fiber-role-in-muscle-building

76) Sudret, B., “Global sensitivity analysis using polynomial chaos expansions,” Reliability Engineering & System Safety, Vol. 93, No. 7, 964–979, 2008.

77) G. Blatman and B. Sudret, “Adaptive sparse polynomial chaos expansion based on least angle regression,” J. Comput. Phys., vol. 230, no. 6, pp. 2345–2367, 2011

78) I. M., Sobol “Sensitivity estimates for nonlinear mathematical models,” Mathematical Modelling and Computational Experiments, Vol. 1, No. 4, 407–414, 1993

79) S. Marelli, and B. Sudret, UQLab: A framework for uncertainty quantification in Matlab, Proc. 2nd Int. Conf. on Vulnerability, Risk Analysis and Management (ICVRAM2014), Liverpool, United Kingdom, 2014, 2554–2563.

80) Advanced Design System (ADS) 2019, Keysight Technology.

81) A. Mouapi, N. Hakem and N. Kandil, "A Performance Analysis of Schottky Diode to support RF Energy Harvesting," *2019 IEEE International Symposium on Antennas and Propagation and USNC-URSI Radio Science Meeting*, Atlanta, GA, USA, 2019, pp. 1169-1170, doi: 10.1109/APUSNCURSINRSM.2019.8888832.

82) M. ur Rehman, W. Ahmad and W. T. Khan, "Highly efficient dual band 2.45/5.85 GHz rectifier for RF energy harvesting applications in ISM band," *2017 IEEE Asia Pacific Microwave Conference (APMC)*, Kuala Lumpar, 2017, pp. 150-153, doi: 10.1109/APMC.2017.8251400.

83) Technical Sheet of Wirewound RF Chip Inductors0603cd Series from Pulse Electronics

84) PSpice, EMA Design Automation, Inc. 225 Tech Park Drive, Rochester, NY 14623, USA

85) https://www.pasternack.com/t-calculator-microstrip.aspx

86) H. Danneels, K. Coddens and G. Gielen, "A fully-digital, 0.3V, 270 nW capacitive sensor interface without external references," 2011 Proceedings of the ESSCIRC (ESSCIRC), Helsinki, 2011, pp. 287-290.

87) Bracke, W., Merken, P., Puers, R., Member, S., & Hoof, C. Van. (2007). Ultra-Low-Power Interface Chip for Autonomous Capacitive Sensor Systems, 54(1), 130–140.

88) Z. Tan et al., "A 1.8V 11μW CMOS smart humidity sensor for RFID sensing applications," IEEE Asian Solid-State Circuits Conference 2011, Jeju, 2011, pp. 105-108.

89) M. Kamarainen et al., "A 1.5μW 1V 2nd-Order ΔΣ Sensor Front-End with Signal Boosting and Offset Compensation for a Capacitive 3-Axis Micro-Accelerometer," 2008 IEEE International Solid-State Circuits Conference - Digest of Technical Papers, San Francisco, CA, 2008, pp. 578-637.

90) Sauter, M. (2010). From GSM to LTE. An Introduction to Mobile Networks and Mobile Broadband, *Wiley*, 2014, pp. 251.

91) Rogers corporation, RO3210 Circuit Materials Data Sheet.

92) M. Vallejo, J. Recas, P.G. del Valle, J.L. Ayala Accurate Human Tissue Characterization for Energy-Efficient Wireless On-Body Communications. Sensors. 2013; 13: 7546–7569

93) Gabriel S., Lau R., and Gabriel C., “The dielectric properties of biological tissues: II. Measurements on the frequency range 10 Hz to 20 GHz,” Phys.Med. Biol., vol. 41, pp. 2251–2269, 1996.

94) Deneris Z. A., Pe'a D. E. and Furse C. M., "A Layered Pork Model for Subdermal Antenna Tests at 433 MHz," in IEEE Journal of Electromagnetics, RF and Microwaves in Medicine and Biology, vol. 3, no. 3, pp. 171-176, Sept. 2019.

Publications

Journals:

S. Ding, S. Koulouridis, and L. Pichon, Miniaturized implantable power transmission system for biomedical wireless applications, Wireless Power Transfer, vol. 7, no. 1, pp. 1–9, 2020.

S. Ding; L. Pichon, Sensitivity Analysis of an Implanted Antenna within Surrounding Biological Environment. Energies 2020, 13, 996.

S. Ding, S. Koulouridis, and L. Pichon, Design and characterization of a dual-band miniaturized circular antenna for deep in body biomedical wireless applications, International Journal of Microwave and Wireless Technologies, pp. 1–8, 2020

S. Ding, S. Koulouridis and L. Pichon, "Implantable Wireless Transmission Rectenna System for Biomedical Wireless Applications," in IEEE Access, vol. 8, pp. 195551-195558, 2020, doi: 10.1109/ACCESS.2020.3032848.

International Conferences:

2019 13th European Conference on Antennas and Propagation (EuCAP)

S. Ding, S. Koulouridis and L. Pichon, "A Dual-Band Miniaturized Circular Antenna for Deep in Body Biomedical Wireless Applications," *2019 13th European Conference on Antennas and Propagation (EuCAP)*, Krakow, Poland, 2019, pp. 1-4.

2019 IEEE Wireless Power Transfer Conference (WPTC)

S. Ding, S. Koulouridis and L. Pichon, "Implantable rectenna system for biomedical wireless applications," *2019 IEEE Wireless Power Transfer Conference (WPTC)*, London, United Kingdom, 2019, pp. 454-457, doi: 10.1109/WPTC45513.2019.9055687.

2020 14th European Conference on Antennas and Propagation (EuCAP)

S. Ding, Y. Pei, L. Pichon and S. Koulouridis, "Impact of Parameters Variability on the Performances of an Implanted Antenna for Biomedical Applications," *2020 14th European Conference on Antennas and Propagation (EuCAP)*, Copenhagen, Denmark, 2020, pp. 1-4, doi: 10.23919/EuCAP48036.2020.9135804.

National Conferences:

Huitième conférence plénière biennale du GDR ONDES - CentraleSupélec

S. Ding, S. Koulouridis and L. Pichon, Système miniaturisé de transmission d'énergie sans fils pour des applications biomédicales, Huitième conférence plénière biennale du GDR ONDES - CentraleSupélec